Type Ia Supernovae Are Excellent Standard Candles in the Near-infrared

Arturo Avelino[1] , Andrew S. Friedman[2] , Kaisey S. Mandel[3,4] , David O. Jones[5] , Peter J. Challis[1], and
Robert P. Kirshner[1,6]

[1] Harvard-Smithsonian Center for Astrophysics, 60 Garden Street, Cambridge, MA 02138, USA; arturo.avelino.h@gmail.com
[2] University of California, San Diego, La Jolla, California 92093, USA; asf@ucsd.edu
[3] Institute of Astronomy and Kavli Institute for Cosmology, Madingley Road, Cambridge, CB3 0HA, UK
[4] Statistical Laboratory, DPMMS, University of Cambridge, Wilberforce Road, Cambridge, CB3 0WB, UK
[5] University of California, Santa Cruz, Santa Cruz, CA 95064, USA
[6] Gordon and Betty Moore Foundation, 1661 Page Mill Road, Palo Alto, CA 94304, USA

Abstract

We analyze a set of 89 type Ia supernovae (SNe Ia) that have both optical and near-infrared (NIR) photometry to derive distances and construct low-redshift ($z \leqslant 0.04$) Hubble diagrams. We construct mean light curve (LC) templates using a hierarchical Bayesian model. We explore both Gaussian process (GP) and template methods for fitting the LCs and estimating distances, while including peculiar-velocity and photometric uncertainties. For the 56 SNe Ia with both optical and NIR observations near maximum light, the GP method yields a NIR-only Hubble-diagram with a root mean square (rms) of 0.117 ± 0.014 mag when referenced to the NIR maxima. For each NIR band, a comparable GP method rms is obtained when referencing to NIR-max or B-max. Using NIR LC templates referenced to B-max yields a larger rms value of 0.138 ± 0.014 mag. Fitting the corresponding optical data using standard LC fitters that use LC shape and color corrections yields larger rms values of 0.179 ± 0.018 mag with SALT2 and 0.174 ± 0.021 mag with SNooPy. Applying our GP method to subsets of SNe Ia NIR LCs at NIR maximum light, even without corrections for LC shape, color, or host-galaxy dust reddening, provides smaller rms in the inferred distances, at the ~ 2.3–4.1σ level, than standard optical methods that correct for those effects. Our ongoing RAISIN program on the *Hubble Space Telescope* will exploit this promising infrared approach to limit systematic errors when measuring the expansion history of the universe in order to constrain dark energy.

Unified Astronomy Thesaurus concepts: Cosmology (343); Distance measure (395); Type Ia supernovae (1728); Infrared photometry (792); Optical observation (1169); Photometry (1234)

1. Introduction

The increasing sample of high-quality low-redshift (low-z), near-infrared (NIR) light curves (LCs) of type Ia supernovae (SNe Ia) provides an opportunity to further investigate their utility as cosmological standard candles. Optical samples of SNe Ia are large enough now that systematic uncertainties are a major limitation to accurate cosmological constraints. Infrared observations of SNe Ia can help in that essential way because SNe are better standard candles in the NIR than in the optical bands and the effects of dust are diminished. This paper explores ways to use NIR observations of SNe Ia to measure distances. This investigation is for a low-z sample, but we are working to extend this technique to cosmologically interesting distances with the *Hubble Space Telescope* (*HST*).

Before NIR photometry became practical for large samples of SNe Ia, photometry and spectroscopy of SNe Ia at optical wavelengths enabled the unexpected 1998 discovery of cosmic acceleration (Riess et al. 1998; Schmidt et al. 1998; Perlmutter et al. 1999). Since then, a suite of independent cosmological methods has confirmed the SNe Ia results (see Frieman et al. 2008; Weinberg et al. 2013 for reviews). The prevailing view is that the mechanism behind cosmic acceleration is some form of dark energy. The constraints on cosmological parameters from the SNe Ia Pantheon sample (Scolnic et al. 2018) combined with

the Planck 2015/2018 Cosmic Microwave Background data (Planck Collaboration et al. 2016b, 2018), as well as Baryon Acoustic Oscillations (Alam et al. 2017) and local Hubble constant measurements (Riess et al. 2016, 2018a, 2018b, 2018c) are consistent with this view. Among the major cosmological techniques, SNe Ia provide precise measurements of extragalactic distances and the most direct evidence for cosmic acceleration (see Goobar & Leibundgut 2011; Kirshner 2013; Goobar 2015; Davis & Parkinson 2016; Riess et al. 2018c for reviews).

Optical SNe Ia LCs are known to be excellent *standardizable* candles that exploit correlations between intrinsic luminosity and LC shape and color (Phillips 1993; Hamuy et al. 1996; Riess et al. 1996, 1998; Perlmutter et al. 1997; Phillips et al. 1999; Goldhaber et al. 2001; Tonry et al. 2003; Wang et al. 2003; Guy et al. 2005, 2007, 2010; Astier et al. 2006; Jha et al. 2006, 2007; Prieto et al. 2006; Conley et al. 2008; Takanashi et al. 2008; Mandel et al. 2009, 2011, 2017). Recent work has demonstrated that SNe Ia in the NIR are approximately *standard* candles, even before correction for LC shape or host galaxy dust reddening (e.g., Krisciunas et al. 2004a, 2009; Wood-Vasey et al. 2008; Mandel et al. 2009; Friedman 2012; Kattner et al. 2012). Near-infrared LCs are about 5–11 times less sensitive to dust extinction than optical B-band data (Cardelli et al. 1989). When constructing SNe Ia Hubble diagrams using NIR data, the distance errors produced by extinction are small: ignoring dust would be fatal for optical studies but presents less of a problem for NIR studies like Wood-Vasey et al. (2008) or the present work. An improved approach would use optical and infrared data simultaneously to determine the extinction (Mandel et al. 2011).

Optical-only samples yield typical Hubble diagram intrinsic scatter of $\sigma_{int} \sim 0.12$ mag and a root mean square (rms) of 0.141 mag after applying LC shape, host-galaxy dust, and host-galaxy mass corrections, assuming a peculiar-velocity uncertainty of 250 km s^{-1} (e.g., Scolnic et al. 2018). For simplicity, we adopt a conservative peculiar-velocity uncertainty for the host galaxies in our sample of 150 km s^{-1}. If the typical redshifts in the sample were large enough, this would be of no consequence, but for our nearby sample, the inferred intrinsic scatter of the SN luminosities depends on the value we choose. As a result, though we have confidence when comparing the rms and intrinsic scatter for various subsamples containing the same SN with both optical and infrared data, the real value of the scatter should be determined from observations that are securely in the Hubble flow beyond 10,000 km s^{-1}.

When including a peculiar-velocity uncertainty of 150 km s^{-1}, our best method yields an intrinsic scatter as small as $\sim$0.03–0.11 mag, depending on the NIR filter subset, and an rms of $\sim$0.087 $\pm$ 0.013 mag for the best NIR YJH-band subset, confirming and strengthening previous results for NIR methods (Meikle 2000; Krisciunas et al. 2004a, 2005, 2007; Wood-Vasey et al. 2008; Folatelli et al. 2010; Burns et al. 2011; Mandel et al. 2009, 2011; Kattner et al. 2012; Dhawan et al. 2015). Assuming a larger peculiar-velocity uncertainty, such as 250 km s^{-1}, makes our estimated intrinsic scatter even *smaller*. In addition, our best NIR method using any of the $YJHK_s$ bands yields an rms of only 0.117 $\pm$ 0.014 mag, compared to 0.179 $\pm$ 0.018 mag and 0.174 $\pm$ 0.021 mag for SALT2 and SNooPy fits to optical BVR data for the same 56 SNe Ia, respectively. While using LC shape, color, and host galaxy dust corrections would likely lead to improvements, the simpler approaches in this paper are still remarkably effective.

Overall, a substantial body of evidence indicates that rest-frame LCs of SNe Ia in the NIR are better standard candles than at optical wavelengths and are less sensitive to the confounding effects of dust. When NIR data are combined with *UBVRI* photometry, this yields accurate and precise distance estimates (Krisciunas et al. 2004b, 2007; Wood-Vasey et al. 2008; Mandel et al. 2009, 2011, 2014, 2017; Folatelli et al. 2010; Burns et al. 2011; Friedman 2012; Kattner et al. 2012; Phillips 2012; Burns et al. 2014).

This is significant for supernova cosmology because, along with photometric-calibration uncertainties (Scolnic et al. 2015; Foley et al. 2018), uncertain dust extinction estimates and the intrinsic variability of SNe Ia colors present challenging and important systematic problems for dark energy measurements (Wang et al. 2006; Conley et al. 2007, 2011; Guy et al. 2007, 2010; Jha et al. 2007; Wood-Vasey et al. 2007; Hicken et al. 2009a; Kessler et al. 2009a, 2019b; Chotard et al. 2011; Komatsu et al. 2011; Campbell et al. 2013; Narayan 2013; Rest et al. 2014; Scolnic et al. 2014a, 2014b, 2015, 2017, 2018; Betoule et al. 2014; Mosher et al. 2014; Narayan et al. 2016; Mandel et al. 2017; Dark Energy Survey Collaboration et al. 2018; Foley et al. 2018). Combining optical and NIR LCs promises to reduce these systematic distance uncertainties (Folatelli et al. 2010; Burns et al. 2011; Kattner et al. 2012; Mandel et al. 2011, 2014).

This work is organized as follows. In Section 2, we review previous results with SNe Ia in the NIR, detail our analysis selection criteria, and discuss host galaxy redshifts. In Section 3, we outline our Gaussian process (GP) procedure to fit LCs and our hierarchical Bayesian model to construct mean $YJHK_s$ LC templates. In Section 4, we use these templates and GP fits to individual LCs to construct Hubble diagrams in each NIR band, as well as a combined $YJHK_s$ NIR Hubble diagram. We compare this to optical BVR Hubble diagrams for the very same set of 56 SNe using the SALT2 and SNooPy LC fitters. We end with Section 5 by documenting how, even without correcting for LC shape or dust, SNe Ia in the NIR using our GP fits at NIR maximum are better standard candles than optical SNe Ia observations corrected for these effects. Mathematical details of the GP method, the hierarchical Bayesian model, and the method for determining the intrinsic scatter are presented in the Appendices.

2. Type Ia Supernovae in the NIR as Standard Candles

Pioneering studies by Meikle (2000) and Krisciunas et al. (2004a) demonstrated that SNe Ia display less luminosity variation in the NIR JHK_s bands than in the optical BV bands at the time of B-band maximum light ($t_{B\,max}$). Krisciunas et al. (2004a) found that optical LC shape and intrinsic NIR luminosity were uncorrelated in a sample of 16 SNe Ia, while measuring a NIR absolute magnitude scatter of $\sigma_J = 0.14$, $\sigma_H = 0.18$, and $\sigma_{K_s} = 0.12$ mag. Following this, Wood-Vasey et al. (2008) used a homogeneously observed sample of 18 spectroscopically normal SNe Ia in the JHK_s bands, with intrinsic rms absolute magnitudes of 0.15 mag in the H-band, *without* applying any reddening or LC shape corrections. By combining these 18 objects with 23 SNe Ia from the literature, the sample in Wood-Vasey et al. (2008) yielded an H-band rms of 0.16 mag, strengthening the evidence that normal SNe Ia are excellent NIR standard candles. In the present work, we show that SNe Ia in the NIR yield a narrow distribution of $YJHK_s$ peak magnitudes with rms Hubble diagram scatter as small as 0.087 $\pm$ 0.013 mag for the combined YJH bands and as large as 0.179 $\pm$ 0.029 mag for the K_s band, consistent with previous results.

Following Wood-Vasey et al. (2008), Mandel et al. (2009) developed a new hierarchical Bayesian model (BAYESN) and a template model to account for J-band LC shape variation to the existing SNe Ia in NIR sample, finding a marginal scatter in the peak absolute magnitudes of 0.17, 0.11, and 0.19 mag, in JHK_s, respectively, while finding that J-band LC shape does correlate with NIR intrinsic luminosity. Subsequent work by Folatelli et al. (2010) applied a different LC shape-correction method, but found scatters of 0.12–0.16 mag in $YJHK_s$, consistent with the results of Mandel et al. (2009).

Additional work by Kattner et al. (2012) found an absolute magnitude scatter of 0.12, 0.12, and 0.09 mag in YJH, respectively, by analyzing a subset of 13 well-sampled normal NIR SNe Ia LCs with relatively little host galaxy dust extinction. Kattner et al. (2012) also showed evidence for a correlation between the JH-band absolute magnitudes at t_{Bmax} and, $\Delta m_{15}(B)$, the light-curve decline rate parameter in B-band after 15 days of t_{Bmax} (Phillips 1993), with no evidence for strong correlation in the Y-band. This is also consistent with the results of Mandel et al. (2009), who found that J-band LC shape and luminosity are correlated.

Using a small data set of 12 SNe Ia JH-band LCs, each with only three to five data points, Barone-Nugent et al. (2012, 2013) find a scatter of 0.116 mag and 0.085 mag in the J- and H-bands, respectively. In the first data release of the SweetSpot survey, Weyant et al. (2014) presented a similarly small sample of 13 low-z SNe Ia, each with between one and

three LC points, finding an H-band scatter of 0.164 mag. This was followed by a second SweetSpot data release, which included a total of 33 SNe Ia with 168 JHK_s observations in the redshift range $0.02 < z < 0.09$, well into the smooth Hubble flow, but did not present NIR Hubble diagrams (Weyant et al. 2018).

By analyzing 45 NIR LCs with data near NIR-maximum, Stanishev et al. (2018) find an intrinsic Hubble diagram scatter of ∼0.10 mag, after accounting for potential new correlations between light curve shape, color excess, and $J - H$ color at NIR-max. Stanishev et al. (2018) also present single-epoch JH photometry for 16 new SNe Ia with $z > 0.037$. The Carnegie Supernova Project (CSP) final data release (CSP-I; Krisciunas et al. 2017) was recently analyzed by Burns et al. (2018), who found peculiar-velocity corrected Hubble diagram dispersions of ∼0.08–0.15 mag, depending on the subset of the 120 SNe Ia they considered. Additional CSP-II photometric data, to be published in 2019, was recently described in Phillips et al. (2019). Hsiao et al. (2019) present an overview of the NIR SNe Ia spectroscopy obtained by the CSP and the Center for Astrophysics (CfA) Supernova Group.

While the current sample of optical SNe Ia LCs exceeds 1000 (Scolnic et al. 2018), and will be increased by orders of magnitude by ongoing and future surveys including the Dark Energy Survey (DES; Dark Energy Survey Collaboration et al. 2016, 2018, 2019a, 2019b, 2019c, 2019d, 2019e), the Zwicky Transient Facility (ZTF; Smith et al. 2014), and the Large Synoptic Survey Telescope (LSST; Ivezic et al. 2019; Zhan & Tyson 2018), the number of normal SNe Ia with published NIR LCs is still less than 250. Nevertheless, the NIR sample has the potential to improve systematic errors compared to optical-only SNe Ia cosmology samples, which are already limited by their systematic errors (Scolnic et al. 2018).

Overall, the growing sample of photometric data suggests that NIR observations of SNe Ia present a promising path to standardize SNe Ia for distance estimates (Dhawan et al. 2015; Shariff et al. 2016; Burns et al. 2018; Stanishev et al. 2018), Hubble constant estimates (Cartier et al. 2014; Efstathiou 2014; Riess et al. 2016; Cardona et al. 2017; Burns et al. 2018; Dhawan et al. 2018), and eventually cosmological parameter estimates when the nearby and high-z samples are combined as in the *HST* RAISIN program (RAISIN: *Tracers of cosmic expansion with* SN IA *in the* IR, PI: R. Kirshner, *HST* GO-13046, GO-14216).

2.1. Nearby SNe Ia in NIR Sample and Data Cuts

This work analyzes a suitable subset including 89 objects from the current sample of low-redshift photometric data for SNe Ia NIR $YJHK_s$-band LCs including data releases 1 and 2 from the CSP (Schweizer et al. 2008; Contreras et al. 2010; Stritzinger et al. 2010, 2011; Taddia et al. 2012), now superseded by CSP data release 3 (Krisciunas et al. 2017), the CfA (Wood-Vasey et al. 2008; Friedman 2012; Friedman et al. 2015), and other groups (e.g., Krisciunas et al. 2000, 2004b, 2004c, 2005, 2007). We limit our analysis to spectroscopically normal SNe Ia from Table 3 of Friedman et al. (2015), plus the definitive version of the CSP-I DR3 sample of low-z SNe Ia (Krisciunas et al. 2017), and other groups. Additional CSP-II photometric data, to be published in 2019, was recently described in Phillips et al. (2019) and will be analyzed in future work.

Table 1
Data Cuts

Cuts	# SNe Ia After Cuts
Initial Sample	177
$0.8 < \Delta m_{15} < 1.6$	138
$-0.15 < E(B - V)_{host} < 0.4$	122
$E(B - V)_{MW} < 1$	122
$z_{CMB} < 0.04$	111
Remove Duplicates	100
Normal Spectrum	95
$\geqslant 3$ LC Points	89

Note. Reduction of the initial sample based on data cuts

We determine $\Delta m_{15}(B)$ and $E(B - V)_{host}$ with the SNooPy LC fitting package (Burns et al. 2011). In the process of applying K-corrections to transform the data to the rest-frame, we use SNooPy to transform all observer-frame JHK-band data to the natural system of the PAIRITEL/2MASS telescope used by the CfA (Friedman et al. 2015), with the observed Y-band data remaining in the natural system of the CSP Swope telescope, since only the CSP data included Y-band observations (Krisciunas et al. 2017).

We apply the following data cuts to analyze a subset of 89 SNe Ia with NIR data. Table 1 shows how the initial sample of 177 SNe Ia decreases after applying the different cuts, and Table 2 lists the general properties of the remaining 89 SNe Ia.

1. Optical light curve shape parameter $0.8 < \Delta m_{15}(B) < 1.6$, to consider *normal* SNe Ia only (Hicken et al. 2009b). Objects must have accompanying B-band optical data to measure $\Delta m_{15}(B)$.
2. Host galaxy reddening: $-0.15 < E(B - V)_{host} < 0.4$. This cut is inspired by the standard SALT2 cut in color, $-0.3 < c < 0.3$, in optical-only analysis (Betoule et al. 2014; Scolnic et al. 2018) but with a less stringent cut considering that SNe Ia in the NIR are less sensitive to dust.
3. One advantage of the relative NIR insensitivity to dust reddening is that it also allows us to set a large threshold for Milky Way color excess: $E(B - V)_{MW} < 1$ mag, to exclude highly reddened SNe Ia. All 177 SNe Ia in the sample passed this cut. SN2006lf with $E(B - V)_{MW} = 0.8135$ mag has the largest color excess in the initial sample.
4. Redshift range: $z < 0.04$. The maximum redshift cut limits the effects of Malmquist bias. Section 2.2 describes corrections to deal with SNe Ia at $z < 0.01$ that suffer from peculiar-velocity bias.
5. Duplicates: For a given SN observed by multiple surveys, we use the CSP data (Krisciunas et al. 2017), which typically have smaller photometric uncertainties than the CfA PAIRITEL data (Friedman et al. 2015).
6. We include only spectroscopically normal SNe Ia as identified by the Supernova Identification Code (SNID) Blondin & Tonry (2007).
7. At least three photometric points in a given band for each SNe Ia LC. A large fraction of the NIR data from Barone-Nugent et al. (2012), Stanishev et al. (2018), and the SweetSPOT survey with WIYN (Weyant et al. 2014, 2018) did not meet this criterion, so we chose not to analyze these data in this work.

Table 2
SNe Ia Light-Curve Parameters

SN Name	$z_{(helio)}$[a]	z_{CMB}[b]	$\sigma_{\mu pec}$[c] (mag)	LC Data Source[d]	$t_{B\,max}$[e] (MJD days)	$\Delta m_{15}(B)$[f] (mag)	$E(B-V)_{host}$[g] (mag)	$E(B-V)_{MW}$[h] (mag)
SN1998bu	0.0030 ± 0.000003	0.0025 ± 0.00023	0.000	CfA	50953.11 ± 0.08	1.076 ± 0.012	0.351 ± 0.006	0.022 ± 0.0002
SN1999ee	0.0114 ± 0.000010	0.0112 ± 0.00050	0.137	K04b	51469.61 ± 0.04	0.802 ± 0.007	0.384 ± 0.004	0.017 ± 0.0001
SN1999ek	0.0176 ± 0.000007	0.0178 ± 0.00050	0.086	K04c	51482.60 ± 0.19	1.113 ± 0.031	0.277 ± 0.014	0.479 ± 0.0187
SN2000bh	0.0229 ± 0.000027	0.0240 ± 0.00050	0.064	K04b	51636.16 ± 0.25	1.055 ± 0.019	0.065 ± 0.012	0.047 ± 0.0064
SN2000ca	0.0236 ± 0.000200	0.0239 ± 0.00050	0.064	K04b	51666.25 ± 0.18	0.917 ± 0.019	-0.033 ± 0.010	0.057 ± 0.0025
SN2000E	0.0047 ± 0.000003	0.0056 ± 0.00050	0.273	V03	51577.20 ± 0.13	1.041 ± 0.027	0.217 ± 0.011	0.319 ± 0.0086
SN2001ba	0.0296 ± 0.000033	0.0302 ± 0.00050	0.051	K04b	52034.47 ± 0.17	0.997 ± 0.020	-0.072 ± 0.009	0.054 ± 0.0017
SN2001bt	0.0146 ± 0.000033	0.0142 ± 0.00050	0.108	K04c	52064.69 ± 0.07	1.199 ± 0.009	0.216 ± 0.008	0.056 ± 0.0007
SN2001cn	0.0152 ± 0.000127	0.0154 ± 0.00050	0.100	K04c	52071.93 ± 0.19	1.044 ± 0.012	0.176 ± 0.008	0.051 ± 0.0008
SN2001cz	0.0155 ± 0.000027	0.0171 ± 0.00050	0.090	K04c	52104.10 ± 0.10	0.956 ± 0.014	0.136 ± 0.008	0.079 ± 0.0005
SN2001el	0.0039 ± 0.000007	0.0045 ± 0.00014	0.000	K03	52182.38 ± 0.10	1.080 ± 0.019	0.277 ± 0.010	0.012 ± 0.0003
SN2002dj	0.0094 ± 0.000003	0.0083 ± 0.00152	0.000	P08	52451.04 ± 0.14	1.111 ± 0.019	0.093 ± 0.013	0.082 ± 0.0009
SN2003du	0.0064 ± 0.000013	0.0094 ± 0.00035	0.000	St07	52766.01 ± 0.09	1.010 ± 0.015	-0.033 ± 0.010	0.008 ± 0.0008
SN2003hv	0.0056 ± 0.000037	0.0049 ± 0.00034	0.000	L09	52891.49 ± 0.11	1.501 ± 0.006	-0.092 ± 0.007	0.013 ± 0.0008
SN2004ef	0.0310 ± 0.000017	0.0301 ± 0.00050	0.051	CSP	53264.90 ± 0.05	1.422 ± 0.011	0.116 ± 0.006	0.046 ± 0.0013
SN2004eo	0.0156 ± 0.000003	0.0152 ± 0.00050	0.101	CSP	53278.90 ± 0.04	1.318 ± 0.006	0.077 ± 0.005	0.093 ± 0.0010
SN2004ey	0.0158 ± 0.000003	0.0154 ± 0.00050	0.100	CSP	53304.81 ± 0.04	1.025 ± 0.011	0.006 ± 0.004	0.120 ± 0.0139
SN2004gs	0.0274 ± 0.000007	0.0287 ± 0.00050	0.054	CSP	53356.75 ± 0.05	1.546 ± 0.006	0.189 ± 0.006	0.026 ± 0.0006
SN2004S	0.0093 ± 0.000003	0.0107 ± 0.00050	0.143	K07	53040.00 ± 0.29	1.052 ± 0.021	0.112 ± 0.014	0.086 ± 0.0014
SN2005bo	0.0139 ± 0.000027	0.0144 ± 0.00050	0.107	CfA	53479.63 ± 0.15	1.310 ± 0.020	0.272 ± 0.007	0.044 ± 0.0006
SN2005cf	0.0064 ± 0.000017	0.0069 ± 0.00036	0.000	CfA	53534.31 ± 0.06	1.072 ± 0.023	0.088 ± 0.010	0.084 ± 0.0013
SN2005el	0.0149 ± 0.000017	0.0153 ± 0.00050	0.101	CSP	53647.42 ± 0.04	1.370 ± 0.006	-0.102 ± 0.005	0.098 ± 0.0004
SN2005iq	0.0340 ± 0.000123	0.0336 ± 0.00050	0.046	CSP	53688.14 ± 0.06	1.280 ± 0.012	-0.049 ± 0.006	0.018 ± 0.0007
SN2005kc	0.0151 ± 0.000003	0.0145 ± 0.00050	0.106	CSP	53698.31 ± 0.08	1.112 ± 0.023	0.350 ± 0.012	0.114 ± 0.0023
SN2005ki	0.0195 ± 0.000010	0.0203 ± 0.00050	0.076	CSP	53706.01 ± 0.04	1.365 ± 0.004	-0.065 ± 0.004	0.027 ± 0.0009
SN2005lu	0.0320 ± 0.000037	0.0317 ± 0.00050	0.048	CSP	53712.08 ± 0.23	0.834 ± 0.008	0.324 ± 0.011	0.022 ± 0.0009
SN2005na	0.0263 ± 0.000083	0.0272 ± 0.00050	0.056	CfA	53739.37 ± 0.30	1.027 ± 0.014	-0.050 ± 0.012	0.068 ± 0.0025
SN2006ac	0.0231 ± 0.000010	0.0237 ± 0.00050	0.065	CfA	53781.55 ± 0.10	1.189 ± 0.008	0.066 ± 0.010	0.014 ± 0.0006
SN2006ax	0.0167 ± 0.000020	0.0180 ± 0.00050	0.085	CSP	53827.78 ± 0.04	1.058 ± 0.012	-0.009 ± 0.005	0.041 ± 0.0019
SN2006bh	0.0108 ± 0.000013	0.0107 ± 0.00050	0.143	CSP	53834.14 ± 0.06	1.408 ± 0.007	-0.043 ± 0.004	0.023 ± 0.0004
SN2006bt	0.0321 ± 0.000007	0.0307 ± 0.00050	0.050	CSP	53859.29 ± 0.26	1.093 ± 0.042	0.313 ± 0.023	0.042 ± 0.0013
SN2006cp	0.0223 ± 0.000003	0.0223 ± 0.00050	0.069	CfA	53897.45 ± 0.15	1.023 ± 0.046	0.134 ± 0.022	0.022 ± 0.0011
SN2006D	0.0085 ± 0.000017	0.0090 ± 0.00050	0.171	CfA	53757.84 ± 0.08	1.460 ± 0.013	0.062 ± 0.009	0.039 ± 0.0004
SN2006ej	0.0204 ± 0.000007	0.0205 ± 0.00050	0.075	CSP	53977.24 ± 0.25	1.394 ± 0.013	0.016 ± 0.011	0.030 ± 0.0008
SN2006kf	0.0200 ± 0.000010	0.0194 ± 0.00050	0.079	CSP	54041.86 ± 0.05	1.517 ± 0.008	0.007 ± 0.006	0.210 ± 0.0020
SN2006lf	0.0132 ± 0.000017	0.0121 ± 0.00050	0.127	CfA	54045.56 ± 0.06	1.406 ± 0.010	-0.054 ± 0.010	0.814 ± 0.0503
SN2006N	0.0143 ± 0.000083	0.0145 ± 0.00050	0.106	CfA	53761.48 ± 0.15	1.457 ± 0.013	-0.030 ± 0.007	0.083 ± 0.0010
SN2007A	0.0176 ± 0.000087	0.0172 ± 0.00050	0.089	CSP	54113.67 ± 0.13	1.037 ± 0.034	0.225 ± 0.014	0.063 ± 0.0016
SN2007af	0.0055 ± 0.000013	0.0056 ± 0.00018	0.000	CSP	54174.97 ± 0.04	1.116 ± 0.010	0.183 ± 0.005	0.034 ± 0.0008
SN2007ai	0.0317 ± 0.000137	0.0327 ± 0.00050	0.047	CSP	54174.03 ± 0.26	0.844 ± 0.021	0.339 ± 0.013	0.286 ± 0.0035
SN2007as	0.0176 ± 0.000460	0.0184 ± 0.00050	0.084	CSP	54181.15 ± 0.23	1.120 ± 0.023	0.138 ± 0.010	0.123 ± 0.0007
SN2007bc	0.0208 ± 0.000007	0.0211 ± 0.00050	0.073	CSP	54200.82 ± 0.09	1.282 ± 0.012	0.039 ± 0.006	0.019 ± 0.0006
SN2007bd	0.0304 ± 0.000100	0.0311 ± 0.00050	0.049	CSP	54207.43 ± 0.06	1.270 ± 0.012	-0.018 ± 0.010	0.029 ± 0.0009
SN2007ca	0.0141 ± 0.000010	0.0145 ± 0.00050	0.106	CSP	54228.20 ± 0.14	1.037 ± 0.024	0.376 ± 0.012	0.057 ± 0.0016
SN2007co	0.0270 ± 0.000110	0.0274 ± 0.00050	0.056	CfA	54264.91 ± 0.23	1.040 ± 0.040	0.208 ± 0.017	0.096 ± 0.0037
SN2007cq	0.0260 ± 0.000080	0.0252 ± 0.00050	0.061	CfA	54280.90 ± 0.10	1.062 ± 0.021	0.051 ± 0.011	0.092 ± 0.0020
SN2007jg	0.0371 ± 0.000013	0.0380 ± 0.00050	0.040	CSP	54366.64 ± 0.25	1.088 ± 0.034	0.150 ± 0.017	0.090 ± 0.0020
SN2007le	0.0067 ± 0.000003	0.0065 ± 0.00050	0.237	CSP	54399.85 ± 0.07	1.027 ± 0.016	0.379 ± 0.008	0.029 ± 0.0003
SN2007qe	0.0240 ± 0.000050	0.0236 ± 0.00050	0.065	CfA	54429.59 ± 0.10	0.988 ± 0.023	0.069 ± 0.014	0.033 ± 0.0008
SN2007sr	0.0055 ± 0.000030	0.0044 ± 0.00025	0.000	CSP	54449.73 ± 0.19	1.084 ± 0.015	0.173 ± 0.009	0.040 ± 0.0010
SN2007st	0.0212 ± 0.000030	0.0211 ± 0.00050	0.073	CSP	54455.09 ± 0.32	1.486 ± 0.019	0.101 ± 0.018	0.014 ± 0.0004
SN2008af	0.0334 ± 0.000007	0.0340 ± 0.00050	0.045	CfA	54499.69 ± 0.43	1.178 ± 0.010	-0.028 ± 0.023	0.029 ± 0.0012
SN2008ar	0.0262 ± 0.000010	0.0290 ± 0.00050	0.053	CSP	54535.22 ± 0.07	1.032 ± 0.014	0.081 ± 0.008	0.031 ± 0.0011

Table 2
(Continued)

SN Name	$z_{(helio)}$[a]	z_{CMB}[b]	$\sigma_{\mu pec}$[c] (mag)	LC Data Source[d]	$t_{B\,max}$[e] (MJD days)	$\Delta m_{15}(B)$[f] (mag)	$E(B-V)_{host}$[g] (mag)	$E(B-V)_{MW}$[h] (mag)
SN2008bc	0.0151 ± 0.000120	0.0156 ± 0.00050	0.098	CSP	54550.41 ± 0.08	1.015 ± 0.019	0.003 ± 0.008	0.225 ± 0.0042
SN2008bf	0.0235 ± 0.000167	0.0254 ± 0.00050	0.061	CSP	54555.31 ± 0.06	0.967 ± 0.012	−0.013 ± 0.006	0.030 ± 0.0027
SN2008C	0.0166 ± 0.000013	0.0175 ± 0.00050	0.088	CSP	54466.60 ± 0.23	1.075 ± 0.019	0.239 ± 0.010	0.072 ± 0.0023
SN2008fl	0.0199 ± 0.000103	0.0199 ± 0.00050	0.077	CSP	54721.85 ± 0.13	1.328 ± 0.006	0.080 ± 0.005	0.157 ± 0.0058
SN2008fr	0.0390 ± 0.002001	0.0384 ± 0.00050	0.040	CSP	54733.93 ± 0.26	0.920 ± 0.014	−0.002 ± 0.011	0.040 ± 0.0012
SN2008fw	0.0085 ± 0.000017	0.0086 ± 0.00050	0.178	CSP	54732.29 ± 0.15	0.844 ± 0.009	0.112 ± 0.008	0.112 ± 0.0030
SN2008gb	0.0370 ± 0.000167	0.0381 ± 0.00050	0.040	CfA	54748.22 ± 0.34	1.183 ± 0.014	0.080 ± 0.018	0.171 ± 0.0035
SN2008gg	0.0320 ± 0.000023	0.0311 ± 0.00050	0.049	CSP	54750.93 ± 0.34	1.036 ± 0.028	0.155 ± 0.013	0.019 ± 0.0010
SN2008gl	0.0340 ± 0.000117	0.0332 ± 0.00050	0.046	CSP	54768.70 ± 0.09	1.319 ± 0.010	0.030 ± 0.006	0.024 ± 0.0008
SN2008gp	0.0330 ± 0.000070	0.0335 ± 0.00050	0.046	CSP	54779.62 ± 0.04	1.017 ± 0.008	−0.018 ± 0.004	0.104 ± 0.0051
SN2008hj	0.0379 ± 0.000130	0.0372 ± 0.00050	0.041	CSP	54802.26 ± 0.12	1.055 ± 0.027	0.038 ± 0.012	0.030 ± 0.0008
SN2008hm	0.0197 ± 0.000077	0.0210 ± 0.00050	0.073	CfA	54804.74 ± 0.21	0.993 ± 0.025	0.182 ± 0.014	0.380 ± 0.0085
SN2008hs	0.0174 ± 0.000070	0.0189 ± 0.00004	0.058	CfA	54812.94 ± 0.14	1.531 ± 0.015	0.122 ± 0.024	0.050 ± 0.0003
SN2008hv	0.0126 ± 0.000007	0.0140 ± 0.00050	0.110	CSP	54817.65 ± 0.04	1.328 ± 0.006	−0.065 ± 0.006	0.028 ± 0.0008
SN2008ia	0.0219 ± 0.000097	0.0225 ± 0.00050	0.068	CSP	54813.67 ± 0.09	1.340 ± 0.009	0.003 ± 0.007	0.195 ± 0.0050
SN2009aa	0.0273 ± 0.000047	0.0287 ± 0.00050	0.054	CSP	54878.81 ± 0.04	1.172 ± 0.008	0.020 ± 0.005	0.029 ± 0.0009
SN2009ab	0.0112 ± 0.000020	0.0103 ± 0.00050	0.149	CSP	54883.89 ± 0.08	1.288 ± 0.016	0.050 ± 0.010	0.184 ± 0.0028
SN2009ad	0.0284 ± 0.000003	0.0287 ± 0.00050	0.054	CSP	54886.91 ± 0.07	0.949 ± 0.013	0.020 ± 0.007	0.095 ± 0.0011
SN2009ag	0.0086 ± 0.000007	0.0102 ± 0.00050	0.151	CSP	54890.23 ± 0.16	1.088 ± 0.019	0.343 ± 0.009	0.218 ± 0.0012
SN2009al	0.0221 ± 0.000080	0.0234 ± 0.00050	0.066	CfA	54897.20 ± 0.18	1.079 ± 0.033	0.236 ± 0.020	0.021 ± 0.0004
SN2009an	0.0092 ± 0.000007	0.0107 ± 0.00050	0.144	CfA	54898.56 ± 0.09	1.327 ± 0.010	0.063 ± 0.010	0.016 ± 0.0003
SN2009bv	0.0366 ± 0.000017	0.0385 ± 0.00050	0.040	CfA	54927.07 ± 0.20	0.948 ± 0.033	−0.026 ± 0.019	0.008 ± 0.0008
SN2009cz	0.0212 ± 0.000010	0.0218 ± 0.00050	0.070	CSP	54943.50 ± 0.09	0.899 ± 0.014	0.102 ± 0.007	0.022 ± 0.0003
SN2009D	0.0250 ± 0.000033	0.0243 ± 0.00050	0.063	CSP	54841.65 ± 0.11	1.025 ± 0.024	0.054 ± 0.009	0.044 ± 0.0012
SN2009kk	0.0129 ± 0.000150	0.0122 ± 0.00050	0.126	CfA	55126.37 ± 0.20	1.189 ± 0.006	−0.055 ± 0.011	0.116 ± 0.0025
SN2009kq	0.0117 ± 0.000020	0.0126 ± 0.00050	0.122	CfA	55154.81 ± 0.17	0.992 ± 0.025	0.089 ± 0.010	0.035 ± 0.0005
SN2009Y	0.0093 ± 0.000027	0.0094 ± 0.00050	0.163	CSP	54877.10 ± 0.10	1.063 ± 0.023	0.169 ± 0.010	0.087 ± 0.0005
SN2010ai	0.0184 ± 0.000123	0.0239 ± 0.00018	0.048	CfA	55277.50 ± 0.08	1.421 ± 0.016	−0.075 ± 0.016	0.008 ± 0.0010
SN2010dw	0.0381 ± 0.000150	0.0392 ± 0.00050	0.039	CfA	55358.25 ± 0.35	0.844 ± 0.058	0.177 ± 0.028	0.080 ± 0.0009
SN2010iw	0.0215 ± 0.000007	0.0228 ± 0.00050	0.067	CfA	55497.14 ± 0.26	0.876 ± 0.019	0.084 ± 0.012	0.047 ± 0.0006
SN2010kg	0.0166 ± 0.000007	0.0171 ± 0.00050	0.090	CfA	55543.96 ± 0.10	1.194 ± 0.011	0.183 ± 0.014	0.131 ± 0.0022
SN2011ao	0.0107 ± 0.000003	0.0120 ± 0.00050	0.128	CfA	55639.61 ± 0.11	1.012 ± 0.018	0.035 ± 0.019	0.017 ± 0.0001
SN2011B	0.0047 ± 0.000003	0.0056 ± 0.00050	0.276	CfA	55583.38 ± 0.06	1.174 ± 0.005	0.112 ± 0.008	0.026 ± 0.0011
SN2011by	0.0028 ± 0.000003	0.0051 ± 0.00020	0.000	CfA	55690.95 ± 0.05	1.053 ± 0.008	0.067 ± 0.005	0.012 ± 0.0002
SN2011df	0.0145 ± 0.000020	0.0150 ± 0.00050	0.102	CfA	55716.40 ± 0.11	0.923 ± 0.015	0.072 ± 0.010	0.112 ± 0.0034
SNf20080514-002	0.0219 ± 0.000010	0.0216 ± 0.00050	0.071	CfA	54612.80 ± 0.00	1.360 ± 0.000	−0.143 ± 0.000	0.027 ± 0.0014

Notes.

[a] Heliocentric redshift from the NASA/IPAC Extragalactic Database (NED) or the literature using v_{helio} from Table 3.

[b] Redshift corrected to the CMB frame and using the C15 local flow model or redshift-independent distance information from Table 4.

[c] Uncertainty in the theoretical distance modulus because of the peculiar velocity, defined in Equation (8). The nine objects with redshift-independent distance information in Table 4 (SN1998bu, SN2001el, SN2002dj, SN2003du, SN2003hv, SN2005cf, SN2007af, SN2007sr, and SN2011by) have a peculiar velocity uncertainty of 0.000.

[d] LC-data source. CfA: Wood-Vasey et al. (2008), Friedman et al. (2015), CSP: Krisciunas et al. (2017), Others: K04b: Krisciunas et al. (2004b); K04c: Krisciunas et al. (2004c); V03: Valentini et al. (2003); K03: Krisciunas et al. (2003); P08: Pignata et al. (2008); St07: Stanishev et al. (2007); L09: Leloudas et al. (2009); K07: Krisciunas et al. (2007). Also see Table 3 of Friedman et al. (2015) for references.

[e] Determined by fitting the optical and NIR LCs data with SNooPy.

[f] LC shape parameter: apparent-magnitude decline between B-band peak luminosity and 15 days after peak.

[g] Host galaxy color excess, as measured by SNooPy fits to the optical and NIR LCs.

[h] Milky Way color excess, from the Schlafly & Finkbeiner (2011) Milky Way dust maps.

2.2. Host Galaxy Redshifts

Heliocentric galaxy recession velocities and CMB frame redshifts are shown in Tables 2 and 3. We obtained heliocentric host galaxy recession velocities using the NASA/IPAC Extragalactic Database (NED), using measurements with the smallest reported uncertainty.[7] If the host galaxy was anonymous or had no reported NED redshift, we used redshifts reported in the literature. When no uncertainties are available, we assume a recession velocity uncertainty of $50 \, \mathrm{km \, s^{-1}}$.

To further correct the CMB frame redshifts for local velocity flows and to estimate uncertainties, we used the model of Carrick et al. (2015).[8] Such corrections are most important for SNe Ia with $z < 0.01$ ($v < 3000 \, \mathrm{km \, s^{-1}}$), but we also use them for SNe Ia further into the Hubble flow.

In special cases, we did not use the Carrick et al. (2015) flow model and instead used independent information for individual objects. For several SNe Ia that have $v_{\mathrm{helio}} > 3000 \, \mathrm{km \, s^{-1}}$, but are members of known galaxy clusters, to avoid large peculiar velocities from the cluster velocity dispersion, following Dhawan et al. (2018), we used the mean recession velocity of the cluster based on the cluster redshift from NED to estimate the CMB frame recession velocity for the SNe Ia host galaxy. For SN 2008hs in Abell 347, we used $v_{\mathrm{CMB}} = 5655 \pm 13 \, \mathrm{km \, s^{-1}}$. For SN 2010ai in the Coma cluster, we used $v_{\mathrm{CMB}} = 7166 \pm 54 \, \mathrm{km \, s^{-1}}$ (Pimbblet et al. 2014).

To further avoid peculiar-velocity systematic errors for SNe Ia with $v_{\mathrm{helio}} < 3000 \, \mathrm{km \, s^{-1}}$, where available, we also used redshift-independent distance information from Cepheid variable stars, surface brightness fluctuations (SBF), or the Tully–Fisher method (TF) to estimate an effective CMB frame redshift (see Tables 3–4 for references).

Of the 19 SNe Ia with Cepheid distances μ_{Ceph} and uncertainties $\sigma_{\mu_{\mathrm{Ceph}}}$ in the *HST* SHOES program (Table 5 of Riess et al. 2016), seven with NIR data are included in our Table 3 (SN 2001el, SN 2003du, SN 2005cf, SN 2007af, SN 2007 sr, and SN 2011by). One other SNe Ia (SN 1998bu) also has Cepheid distance from the *HST* Key Project (Table 4 of Freedman et al. 2001).[9] Lastly, two more SNe Ia with NIR data (SN 2002dj and SN 2003hv) had redshift-independent host galaxy distance information from TF and/or SBF (Courtois & Tully 2012; Tully et al. 2013, 2016).

For all of these methods, we convert the reported distance modulus μ' on a given Hubble scale H_0' to the Hubble scale of $H_0 = 73.24 \, \mathrm{km \, s^{-1} \, Mpc^{-1}}$ as measured by Riess et al. (2016) and use this value of H_0 throughout the rest of the paper. More specifically, for Hubble constants in units of $\mathrm{km \, s^{-1} \, Mpc^{-1}}$, the distance modulus μ_{eff} on our fiducial Hubble scale H_0 is given by

$$\mu_{\mathrm{eff}} = 5\log_{10}\left(\frac{H_0'}{H_0}\right) + \mu'. \quad (1)$$

See Table 4.

For these objects, we convert the redshift-independent distance modulus μ_{eff} to an effective CMB frame recession velocity with Hubble's law in the linear regime:

$$v_{\mathrm{eff}} = c\, z_{\mathrm{eff}} = H_0\, d_L(\mu_{\mathrm{eff}}) = H_0 \times 1 \, \mathrm{Mpc} \times 10^{\frac{\mu_{\mathrm{eff}} - 25}{5}}, \quad (2)$$

with an uncertainty given by[10]

$$\sigma_{v_{\mathrm{eff}}} = c\, \sigma_{z_{\mathrm{eff}}} = c\, z_{\mathrm{eff}}\left(\frac{\ln 10}{5}\sigma_{\mu_{\mathrm{eff}}}\right). \quad (3)$$

For SNe Ia with redshift-independent information in Table 4, we assume that the only contribution to the recession velocity uncertainty comes from Equation (3) and therefore adopt a peculiar-velocity uncertainty of $0 \, \mathrm{km \, s^{-1}}$ for these objects.

For objects without Cepheid or other redshift-independent distances, we assume a peculiar-velocity uncertainty of $\sigma_{\mathrm{pec}} = 150 \, \mathrm{km \, s^{-1}}$ following Radburn-Smith et al. (2004).[11] As shown in Section 5, the value of $\sigma_{\mathrm{pec}} = 150 \, \mathrm{km \, s^{-1}}$ yields a more conservative determination of the Hubble diagram intrinsic scatter compared with larger values of σ_{pec} that tend to produce a misleadingly small value. However, statistics like the rms, which we also use to compare various methods, are relatively insensitive to the assumed value of σ_{pec}.

3. Near-infrared LC Templates

We determine the normalized mean $YJHK_s$ LC templates, as shown in Figure 1 and Table 5 using the SNe Ia listed in Table 2 and shown in Figure 2 as follows. In each band, we convert the photometry from the observer-frame apparent magnitude to the rest-frame absolute magnitude. We further apply K-corrections to the rest frame and correct for Milky Way dust extinction. These steps are detailed in Section 3.1. We then use a GP method, as described in Section 3.2, to fit the LC in each NIR band. Finally, in Section 3.3, using a hierarchical Bayesian model, we average all the LCs in a given NIR band to determine the normalized mean LC template, its uncertainty, and the population standard deviation.

3.1. Rest-frame Absolute Magnitudes

For a given supernova s observed through filter O, we convert the apparent magnitude m_s datum observed at the modified Julian day (MJD) t_{MJD} to the absolute magnitude M_s at rest-frame phase t, via

$$M_s(t) = m_s(t) - \mu_{\Lambda\mathrm{CDM}}(z_s) - K^s_{OQ} - A^s_O, \quad (4)$$

where z_s is the spectroscopic redshift of the SN s with respect to the CMB, including any local flow models (see Table 2). The phase $t \equiv (t_{\mathrm{MJD}} - t_{B\max,s})/(1 + z_{\mathrm{helio},s})$ is the rest-frame observation time, corrected for cosmological time dilation, $z_{\mathrm{helio},s}$ is the heliocentric redshift, and $t_{B\max}$ is the time of B-band maximum light. The term K_{OQ} is the K-correction from the observed band O to the rest-frame band Q, and A_O is the Milky Way foreground extinction defined as $A_O = R_O E(B - V)_{\mathrm{MW}}$, where R_O is the total-to-selective

---

[7] However, even if earlier SDSS data releases report a smaller redshift error, we use the SDSS DR13 (2016) reported heliocentric redshift from NED where available (Albareti et al. 2017; http://www.sdss.org/dr13/data_access/bulk/).
[8] https://cosmicflows.iap.fr/lookup/. We used defaults of $\Omega_M = 0.3$ (implicitly $\Omega_\Lambda = 0.7$ for a flat universe), $H_0 = 73.24 \, \mathrm{km \, s^{-1} \, Mpc^{-1}}$ (Riess et al. 2016), $\beta = 0.43$, and bulk flows of $(V_x, V_y, V_z) = (89, -131, 17) \, \mathrm{km \, s^{-1}}$ (Carrick et al. 2015).
[9] We use the metallicity corrected values μ_Z and σ_Z from Table 4 of Freedman et al. (2001).

[10] We do not propagate the uncertainty on H_0 in Equation (2) because we have fixed the Hubble scale for this work.
[11] Estimates in the literature range from $\sigma_{\mathrm{pec}} = 150$–$400 \, \mathrm{km \, s^{-1}}$: $\sigma_{\mathrm{pec}} = 150 \, \mathrm{km \, s^{-1}}$ (Radburn-Smith et al. 2004), $300 \, \mathrm{km \, s^{-1}}$ (Davis et al. 2011), $\sigma_{\mathrm{pec}} = 360 \, \mathrm{km \, s^{-1}}$ (Kessler et al. 2009a), or $\sigma_{\mathrm{pec}} = 400 \, \mathrm{km \, s^{-1}}$ (Wood-Vasey et al. 2007).

Table 3
SNe Ia Recession Velocities

SN Name[a]	R.A. (deg) α(2000)[b]	Decl. (deg) δ(2000)[b]	Host Galaxy (or Cluster)[c]	v_{helio} (km s^{-1})[d]	v_{CMB} (km s^{-1})[e]	$v_{CMB,flow}$ (km s^{-1})[f]	Ref(s).[g]	Code[h]
SN1998bu	161.69167	11.83528	NGC 3368	888 ± 1	757 ± 70	242 ± 150	NED; F01	Ceph
SN1999ee	334.04167	−36.84444	IC 5179	3419 ± 3	3160 ± 3	3368 ± 150	NED; C15	Flow
SN1999ek	84.13167	16.63833	UGC 03329	5266 ± 2	5292 ± 2	5340 ± 150	NED; C15	Flow
SN2000E	309.30750	66.09722	NGC 6951	1424 ± 1	1267 ± 1	1685 ± 150	NED; C15	Flow
SN2000bh	185.31292	−21.99889	ESO 573-G 014	6854 ± 8	7196 ± 8	7188 ± 150	NED; C15	Flow
SN2000ca	203.84583	−34.16028	ESO 383-G 032	7080 ± 60	7351 ± 62	7167 ± 150	NED; C15	Flow
SN2001ba	174.50750	−32.33083	MCG -05-28-001	8861 ± 10	9193 ± 10	9060 ± 150	NED; C15	Flow
SN2001bt	288.44500	−59.28972	IC 4830	4388 ± 10	4331 ± 10	4260 ± 150	NED; C15	Flow
SN2001cn	281.57417	−65.76167	IC 4758	4543 ± 38	4523 ± 38	4626 ± 150	NED; C15	Flow
SN2001cz	191.87583	−39.58000	NGC 4679	4643 ± 8	4930 ± 8	5124 ± 150	NED; C15	Flow
SN2001el	56.12750	−44.63972	NGC 1448	1168 ± 2	1340 ± 42	1568 ± 150	NED; R16	Ceph
SN2002dj	198.25125	−19.51917	NGC 5018	2816 ± 1	2479 ± 457	2023 ± 150	NED; Co12	Misc
SN2003du	218.64917	59.33444	UGC 9391	1914 ± 4	2809 ± 105	3165 ± 150	NED; R16	Ceph
SN2003hv	46.03875	−26.08556	NGC 1201	1686 ± 11	1470 ± 101	1723 ± 150	NED; Tu13	Misc
SN2004S	101.43125	−31.23111	MCG -05-16-021	2788 ± 1	2937 ± 1	3213 ± 150	NED; C15	Flow
SN2004ef	340.54175	19.99456	UGC 12158	9289 ± 5	8931 ± 5	9015 ± 150	NED; C15	Flow
SN2004eo	308.22579	9.92853	NGC 6928	4684 ± 1	4398 ± 1	4560 ± 150	NED; C15	Flow
SN2004ey	327.28254	0.44422	UGC 11816	4749 ± 1	4405 ± 1	4617 ± 150	NED; C15	Flow
SN2004gs	129.59658	17.62772	MCG +03-22-020	8214 ± 2	8475 ± 2	8590 ± 150	NED; C15	Flow
SN2005bo	192.42096	−11.09647	NGC 4708	4166 ± 8	4503 ± 9	4314 ± 150	NED; C15	Flow
SN2005cf	230.38417	−7.41306	MCG -01-39-003	1929 ± 5	2077 ± 109	2034 ± 150	NED; R16	Ceph
SN2005el	77.95300	5.19428	NGC 1819	4470 ± 5	4466 ± 5	4574 ± 150	NED; C15	Flow
SN2005iq	359.63542	−18.70917	ESO 538- G 013	10206 ± 37	9880 ± 36	10058 ± 150	NED; C15	Flow
SN2005kc	338.53058	5.56842	NGC 7311	4524 ± 1	4159 ± 1	4343 ± 150	NED; C15	Flow
SN2005ki	160.11758	9.20233	NGC 3332	5833 ± 3	6185 ± 3	6080 ± 150	NED; C15	Flow
SN2005lu	39.01546	−17.26389	ESO 545-G038	9596 ± 11	9389 ± 11	9515 ± 150	NED; C15	Flow
SN2005na	105.40258	14.13325	UGC 3634	7891 ± 25	8045 ± 25	8162 ± 150	NED; C15	Flow
SN2006D	193.14142	−9.77522	MCG -01-33-034	2556 ± 5	2891 ± 6	2691 ± 150	NED; C15	Flow
SN2006N	92.13000	64.72361	CGCG 308-009	4280 ± 25	4278 ± 25	4354 ± 150	NED; C15	Flow
SN2006ac	190.43708	35.08528	NGC 4619	6923 ± 3	7175 ± 3	7113 ± 150	NED; C15	Flow
SN2006ax	171.01442	−12.29144	NGC 3663	5014 ± 6	5382 ± 6	5386 ± 150	NED; C15	Flow
SN2006bh	340.06708	−66.48508	NGC 7329	3252 ± 4	3148 ± 4	3222 ± 150	NED; C15	Flow
SN2006bt	239.12721	20.04592	CGCG 108-013	9618 ± 2	9714 ± 2	9211 ± 150	NED; K17	Flow
SN2006cp	184.81208	22.42722	UGC 7357	6682 ± 1	6990 ± 1	6673 ± 150	NED; C15	Flow
SN2006ej	9.74904	−9.01572	NGC 191A	6110 ± 2	5780 ± 2	6152 ± 150	NED; C15	Flow
SN2006kf	55.46033	8.15694	UGC 2829	6007 ± 3	5862 ± 3	5821 ± 150	NED; C15	Flow
SN2006lf	69.62292	44.03361	UGC 3108	3954 ± 5	3885 ± 5	3627 ± 150	NED; C15	Flow
SN2007A	6.31942	12.88681	NGC 105	5290 ± 26	4940 ± 24	5162 ± 150	NED; C15	Flow
SN2007af	215.58763	−0.39378	NGC 5584	1638 ± 4	1667 ± 53	1418 ± 150	NED; R16	Ceph
SN2007ai	243.22392	−21.63019	MCG -04-38-004	9492 ± 41	9595 ± 41	9815 ± 150	NED; C15	Flow
SN2007as	141.90004	−80.17756	ESO 018-G 018	5268 ± 138	5368 ± 141	5503 ± 150	NED; C15	Flow
SN2007bc	169.81071	20.80903	UGC 6332	6221 ± 2	6548 ± 2	6333 ± 150	NED; C15	Flow
SN2007bd	127.88867	−1.19944	UGC 4455	9126 ± 30	9408 ± 31	9318 ± 150	NED; C15	Flow
SN2007ca	202.77421	−15.10183	MCG -02-34-061	4217 ± 3	4520 ± 3	4339 ± 150	NED; C15	Flow
SN2007co	275.76500	29.89722	MCG +05-43-016	8083 ± 33	7963 ± 33	8229 ± 150	NED; C15	Flow
SN2007cq	333.66833	5.08028	2MASX J22144070+0504435	7807 ± 24	7448 ± 23	7564 ± 150	Ch13; C15	Flow
SN2007jg	52.46175	0.05683	SDSS J032950.83+000316.0	11113 ± 4	10955 ± 4	11379 ± 150	NED; C15	Flow
SN2007le	354.70171	−6.52258	NGC 7721	2017 ± 1	1660 ± 1	1939 ± 150	NED; C15	Flow
SN2007qe	358.55417	27.40917	NSF J235412.09+272432.3	7183 ± 15	6842 ± 14	7067 ± 150	Ch13; C15	Flow
SN2007sr	180.47000	−18.97269	NGC 4038	1641 ± 9	1327 ± 75	611 ± 150	NED; R16	Ceph
SN2007st	27.17696	−48.64939	NGC 692	6350 ± 9	6195 ± 9	6330 ± 150	NED; C15	Flow
SN2008C	104.29804	20.43714	UGC 3611	4983 ± 4	5121 ± 4	5260 ± 150	NED; C15	Flow
SN2008af	224.86875	16.65333	UGC 9640	10020 ± 2	10199 ± 2	10195 ± 150	NED; C15	Flow
SN2008ar	186.15800	10.83817	IC 3284	7846 ± 3	8180 ± 3	8680 ± 150	NED; C15	Flow
SN2008bc	144.63012	−63.97378	KK 1524	4523 ± 36	4711 ± 37	4677 ± 150	NED; C15	Flow
SN2008bf	181.01208	20.24517	ambiguous	7045 ± 50	7365 ± 52	7608 ± 150	K17; C15	Flow
SN2008fl	294.18683	−37.55125	NGC 6805	5960 ± 31	5815 ± 30	5980 ± 150	NED; C15	Flow
SN2008fr	17.95475	14.64083	SDSS J011149.19+143826.5	11692 ± 600	11373 ± 584	11503 ± 150	NED; C15	Flow
SN2008fw	157.23321	−44.66544	NGC 3261	2563 ± 5	2851 ± 6	2587 ± 150	NED; C15	Flow
SN2008gb	44.48792	46.86583	UGC 2427	11092 ± 50	10921 ± 49	11428 ± 150	NED; C15	Flow
SN2008gg	21.34600	−18.17244	NGC 539	9598 ± 7	9321 ± 7	9330 ± 150	NED; C15	Flow
SN2008gl	20.22842	4.80531	UGC 881	10198 ± 35	9885 ± 34	9954 ± 150	NED; C15	Flow
SN2008gp	50.75304	1.36189	MCG +00-9-74	9901 ± 21	9732 ± 21	10030 ± 150	NED; C15	Flow

Table 3
(Continued)

SN Name[a]	R.A. (deg) $\alpha(2000)$[b]	Decl. (deg) $\delta(2000)$[b]	Host Galaxy (or Cluster)[c]	v_{helio} (km s^{-1})[d]	v_{CMB} (km s^{-1})[e]	$v_{\mathrm{CMB,flow}}$ (km s^{-1})[f]	Ref(s).[g]	Code[h]
SN2008hj	1.00796	−11.16875	MCG -02-01-014	11360 ± 39	11018 ± 38	11140 ± 150	NED; C15	Flow
SN2008hm	51.79542	46.94444	2MFGC 02845	5895 ± 23	5752 ± 22	6282 ± 150	NED; C15	Flow
SN2008hs	36.37333	41.84306	NGC 0910 (Abell 347)	5207 ± 21	5655 ± 13	6186 ± 150	NED; Dh18	Clus
SN2008hv	136.89192	3.39225	NGC 2765	3775 ± 2	4087 ± 2	4185 ± 150	NED; C15	Flow
SN2008ia	132.64646	−61.27794	ESO 125-G 006	6578 ± 29	6761 ± 30	6754 ± 150	NED; C15	Flow
SN2009D	58.59512	−19.18172	MCG -03-10-052	7497 ± 10	7397 ± 10	7275 ± 150	NED; C15	Flow
SN2009Y	220.59938	−17.24678	NGC 5728	2793 ± 8	3019 ± 9	2827 ± 150	NED; C15	Flow
SN2009aa	170.92617	−22.27069	ESO 570-G20	8187 ± 14	8543 ± 15	8597 ± 150	NED; C15	Flow
SN2009ab	64.15162	2.76417	UGC 2998	3349 ± 6	3260 ± 6	3090 ± 150	NED; C15	Flow
SN2009ad	75.88908	6.65992	UGC 3236	8514 ± 1	8496 ± 1	8602 ± 150	NED; C15	Flow
SN2009ag	107.92004	−26.68508	ESO 492-2	2590 ± 2	2774 ± 2	3056 ± 150	NED; C15	Flow
SN2009al	162.84196	8.57853	NGC 3425	6627 ± 24	6982 ± 25	7007 ± 150	NED; C15	Flow
SN2009an	185.69750	65.85111	NGC 4332	2764 ± 2	2867 ± 2	3207 ± 150	NED; C15	Flow
SN2009bv	196.83542	35.78444	MCG +06-29-039	10966 ± 5	11201 ± 5	11539 ± 150	NED; C15	Flow
SN2009cz	138.75008	29.73531	NGC 2789	6344 ± 3	6601 ± 3	6548 ± 150	NED; C15	Flow
SN2009kk	57.43458	−3.26444	2MFGC 03182	3855 ± 45	3729 ± 44	3653 ± 150	NED; C15	Flow
SN2009kq	129.06292	28.06722	MCG +05-21-001	3507 ± 6	3739 ± 6	3766 ± 150	NED; C15	Flow
SN2010ai	194.85000	27.99639	SDSS J125925.04+275948.2 (Coma)	5507 ± 37	7166 ± 54	7298 ± 150	NED; P14	Clus
SN2010dw	230.66792	−5.92111	2MASX J15224062-0555214	11428 ± 45	11600 ± 46	11759 ± 150	NED; C15	Flow
SN2010iw	131.31250	27.82278	UGC 4570	6458 ± 2	6698 ± 2	6833 ± 150	NED; C15	Flow
SN2010kg	70.03500	7.35000	NGC 1633	4986 ± 2	4931 ± 2	5128 ± 150	NED; C15	Flow
SN2011B	133.95208	78.21750	NGC 2655	1400 ± 1	1419 ± 1	1670 ± 150	NED; C15	Flow
SN2011ao	178.46250	33.36278	IC 2973	3210 ± 1	3487 ± 1	3592 ± 150	NED; C15	Flow
SN2011by	178.94000	55.32611	NGC 3972	852 ± 1	1521 ± 61	1796 ± 150	NED; R16	Ceph
SN2011df	291.89000	54.38639	NGC 6801	4361 ± 6	4205 ± 6	4500 ± 150	NED; C15	Flow
SNf20080514-002	202.30625	11.26889	UGC 8472	6577 ± 3	6866 ± 3	6480 ± 150	NED; C15	Flow

Notes.

[a] SNe Ia name. All SNe Ia in this work are spectroscopically normal (see Section 2.1).

[b] Epoch J2000 equatorial coordinates in decimal degrees.

[c] Host galaxy or cluster from NED or the literature. See Ref(s) column.

[d] Heliocentric recession velocity from NED with smallest reported uncertainty (SDSS DR13 values are used even if earlier SDSS reported smaller uncertainties). When no uncertainty is reported we assume an error of 50 km s^{-1}.

[e] CMB frame recession velocity v_{CMB} using v_{helio}, R.A., decl., and CMB dipole from (Planck Collaboration et al. 2016a).

[f] $v_{\mathrm{CMB,flow}}$ takes v_{CMB}, R.A., decl. as input and further corrects to the CMB frame via the local velocity flow model of Carrick et al. (2015) (hereafter C15), with assumed uncertainty of 150 km s^{-1} (see Section 2.2).

[g] The first reference listed is for v_{helio} from NED or the literature. The second reference is for the effective v_{CMB} derived using either the C15 local flow model or independent distance information for nearby galaxies with $v_{\mathrm{helio}} \lesssim 3000$ km s^{-1}, special cases where host galaxy identification from NED is ambiguous, or some clusters which may have $v > 3000$ km s^{-1} (see Section 2.2 and Table 4). Reference codes: C15: Carrick et al. (2015); Ch11: Childress et al. (2011); Ch13: Childress et al. (2013); Co12: Courtois & Tully (2012); Dh18: Dhawan et al. (2018); F01: Freedman et al. (2001); F15: Friedman et al. (2015); H12: Hicken et al. (2012); K17: Krisciunas et al. (2017); MO00: Mould et al. (2000); P14: Pimbblet et al. (2014); Pr07: Prieto et al. (2007); R14: Rest et al. (2014); R16: Riess et al. (2016); Tu13: Tully et al. (2013); Tu16: Tully et al. (2016).

[h] If Code = Flow, we use $v_{\mathrm{CMB,flow}}$ from C15 in our Hubble diagram. If Code ≠ Flow, we use v_{CMB}. Other codes include Ceph: *HST* Cepheid distances from SHOES Riess et al. (2016) or the *HST* Key Project Freedman et al. (2001); Clus: Mean redshift of galaxy cluster from NED (e.g., Virgo, Coma, Abell*); Misc: Surface Brightness Fluctuations (SBF) or Tully–Fisher relation (TF) (e.g., Courtois & Tully 2012; Tully et al. 2013, 2016).

extinction ratio in filter O and $E(B - V)_{\mathrm{MW}}$ is the Milky Way color excess. We use the Schlafly & Finkbeiner (2011) dust reddening map for $E(B - V)_{\mathrm{MW}}$, and the CCM+O (O'Donnell 1994) reddening laws to determine R_O for the NIR and optical bands, respectively. We assume a V-band total-to-selective extinction ratio for the Milky Way of $R_V = 3.1$.

We determine $t_{B \max}$ and compute the K-correction K_{OQ}^s terms using a module in the SNooPy LC-fitting package (Burns et al. 2011), which uses the normal SNe Ia spectroscopic template of Hsiao et al. (2007) that is "mangled" to match the

actual colors derived from the data. Within SNooPy, the observer frame LCs are transformed into the natural systems of the CfA PAIRITEL/2MASS telescope for the JHK-bands and of the CSP Swope telescope for the Y-band, before being K-corrected to the corresponding rest-frame bandpass.

The theoretical distance modulus is defined as

$$\mu_{\Lambda\mathrm{CDM}}(z_s) = 5\log_{10}\left[\frac{d_L(z_s)}{1\ \mathrm{Mpc}}\right] + 25. \qquad (5)$$

Table 4
SNe Ia With Redshift-independent Distance Moduli

SN Name	Host Galaxy (or Cluster)	μ' (mag)[a]	H_0' (km s^{-1} Mpc^{-1})	$\mu_{\rm eff}$ (mag)[b]	References[c]	Code[d]
SN1998bu	NGC 3368	30.110 ± 0.200	72.00 ± 8.00	30.073 ± 0.200	F01	Ceph
SN2001el	NGC 1448	31.311 ± 0.045	73.24 ± 1.74	31.311 ± 0.045	R16	Ceph
SN2002dj	NGC 5018	32.570 ± 0.400	75.90 ± 3.80	32.647 ± 0.400	Co12	Misc
SN2003du	UGC 9391	32.919 ± 0.063	73.24 ± 1.74	32.919 ± 0.063	R16	Ceph
SN2003hv	NGC 1201	31.120 ± 0.250	74.40 ± 3.00	31.154 ± 0.250	Tu13	Misc
SN2005cf	MCG -01-39-003	32.263 ± 0.102	73.24 ± 1.74	32.263 ± 0.102	R16	Ceph
SN2007af	NGC 5584	31.786 ± 0.046	73.24 ± 1.74	31.786 ± 0.046	R16	Ceph
SN2007sr	NGC 4038	31.290 ± 0.112	73.24 ± 1.74	31.290 ± 0.112	R16	Ceph
SN2011by	NGC 3972	31.587 ± 0.070	73.24 ± 1.74	31.587 ± 0.070	R16	Ceph

Notes.
[a] Reported distance modulus μ' on Hubble scale H_0'.
[b] This is converted to a distance modulus $\mu_{\rm eff}$ on the Hubble scale of $H_0 = 73.24$ km s^{-1} Mpc^{-1} via Equation (1). For SNe Ia with Cepheid distances from Riess et al. (2016), since $H_0' = H_0$ and $\mu' = \mu_{\rm eff}$, effective distance moduli $\mu_{\rm eff}$ are already on the Hubble scale used for this paper. We compute the effective CMB frame recession velocity $v_{\rm eff}$ in Table 3 via Equations (2)–(3) using μ' and H_0' (or equivalently $\mu_{\rm eff}$ and H_0). This is then used to construct an effective redshift or recession velocity for use in Hubble diagrams.
[c] Reference codes: Co12: Courtois & Tully (2012); F01: Freedman et al. (2001); R16: Riess et al. (2016); Tu13: Tully et al. (2013); Tu16: Tully et al. (2016).
[d] Same as in Table 3.

We assume the luminosity distance $d_L(z)$ for a spatially flat ΛCDM universe, ignoring radiation, is approximately given by

$$d_L(z) = \left(\frac{c}{H_0}\right)(1 + z_{\rm helio}) \int_0^z \frac{dz'}{E(z')}, \qquad (6)$$

where $E(z) = \sqrt{\Omega_{\rm m}(1 + z)^3 + \Omega_\Lambda}$ and c is the speed of light.[12] We assume fiducial values for the matter and energy density fractions of $\Omega_{\rm m} = 0.28$ and $\Omega_\Lambda = 0.72$ and a Hubble constant of $H_0 = 73.24$ km s^{-1} Mpc^{-1} (Riess et al. 2016).

Every value of M_s has an error variance,

$$\sigma_M^2 = \sigma_m^2 + \sigma_{\mu_{\rm pec}}^2 + \sigma_A^2 + \sigma_{K{\rm corr}}^2, \qquad (7)$$

where σ_m is the measurement uncertainty of the apparent magnitude m_s, and $\sigma_{\mu_{\rm pec}}$ is the uncertainty in the distance modulus $\mu_{\Lambda{\rm CDM}}(z_s)$ due to the peculiar-velocity and redshift uncertainties, given as

$$\sigma_{\mu_{\rm pec},s}^2(z_s) = \left(\frac{5}{z_s \ln(10)}\right)^2 \left[\left(\frac{\sigma_{\rm pec}}{c}\right)^2 + \sigma_{z,s}^2\right]. \qquad (8)$$

For the SN in Table 4 with independent distance estimates, we use those corresponding distance modulus uncertainties. The term σ_A in Equation (7) is the uncertainty in the Milky Way dust extinction A_O computed as, $\sigma_A = R_O \, \sigma_{\rm EBV}$, where $\sigma_{\rm EBV}$ is the uncertainty in the Milky Way color excess $E(B - V)_{\rm MW}$, and $\sigma_{K{\rm corr}}$ is the K-correction uncertainty estimated using Monte Carlo simulations of the full optical and NIR data set $\{m_s\}$ for a given SN. In this Monte Carlo approach, for each photometric datum at a given MJD time and band, $m_s(T_{\rm MJD})$, we simulate a realization of this datum by drawing a random value from a Gaussian distribution with mean and standard deviation equal to the measured values m_s and σ_m. For each simulated full optical+NIR data set, we compute the K-corrections

and then determine the mean and standard deviation of the distribution of the K-correction values for each photometric datum at a given MJD time and band. We use this standard deviation as an estimate of the uncertainty of the K-correction value for that datum.

3.2. LC Fitting: GP

The GP technique is a non-parametric Bayesian method that we use to fit the NIR LCs for each SNe Ia in Table 2. A GP defines a prior over functions. Realizations from a GP, evaluated on a discrete set of times, are random vectors drawn from a joint multivariate Gaussian distribution, $\mathcal{N}$, of dimension equal to the number of components in the vector. Given a data set, the GP formalism allows us to coherently determine the posterior mean function that fits the data set along with its posterior covariance. The GP methodology is especially helpful in accounting for missing data (in our cases, phases with no observations), and when the data are correlated as in the case of the SNe Ia LCs. Rasmussen & Williams (2006) provide an introduction to GPs for machine learning.

The following description applies to a LC of a single SN in a given NIR band. We model the absolute magnitude M at phase t as a noisy measurement of the latent (true) absolute magnitude $\mathcal{M}$ at that phase, given by $M(t) = \mathcal{M}(t) + \epsilon$, where $\epsilon \sim \mathcal{N}(0, \sigma_M^2)$. In vector notation we express the collection of absolute magnitude data of a given LC as $\boldsymbol{M} \equiv [M(t_1), M(t_2),..., M(t_n)]^\top$, measured at phases $\boldsymbol{t} \equiv [t_1, t_2,..., t_n]^\top$, where n is the number of data in the LC, and $\top$ denotes the transpose.

Using the GP method, we estimate the posterior mean, $\boldsymbol{\mu}^{\rm post}$, and the posterior covariance, $\boldsymbol{\Sigma}^{\rm post}$, of the latent absolute magnitudes $\boldsymbol{\mathcal{M}}^* \equiv [\mathcal{M}(t_1^*), \mathcal{M}(t_2^*),..., \mathcal{M}(t_{n^*}^*)]^\top$ on a regular grid of phases $\boldsymbol{t}^* \equiv [t_1^*, t_2^*,..., t_{n^*}^*]^\top$, where n^* is the number of times in the grid determined from a sequence of phases between $t_{\min,s}$ and $t_{\max,s}$ in steps of 0.5 days, where $t_{\min,s}$ and $t_{\max,s}$ are the minimum and maximum phases in $\boldsymbol{t}^*$. Thus the number of times in the regular grid is $n^* = (t_{\max,s} - t_{\min,s})/0.5$. In

---

[12] As noted by Calcino & Davis (2017), using the CMB frame redshift z instead of the heliocentric redshift $z_{\rm helio}$ in Equation (6) causes only a small error, which has a negligible effect on our analysis, especially for the low-redshift sample analyzed in this work.
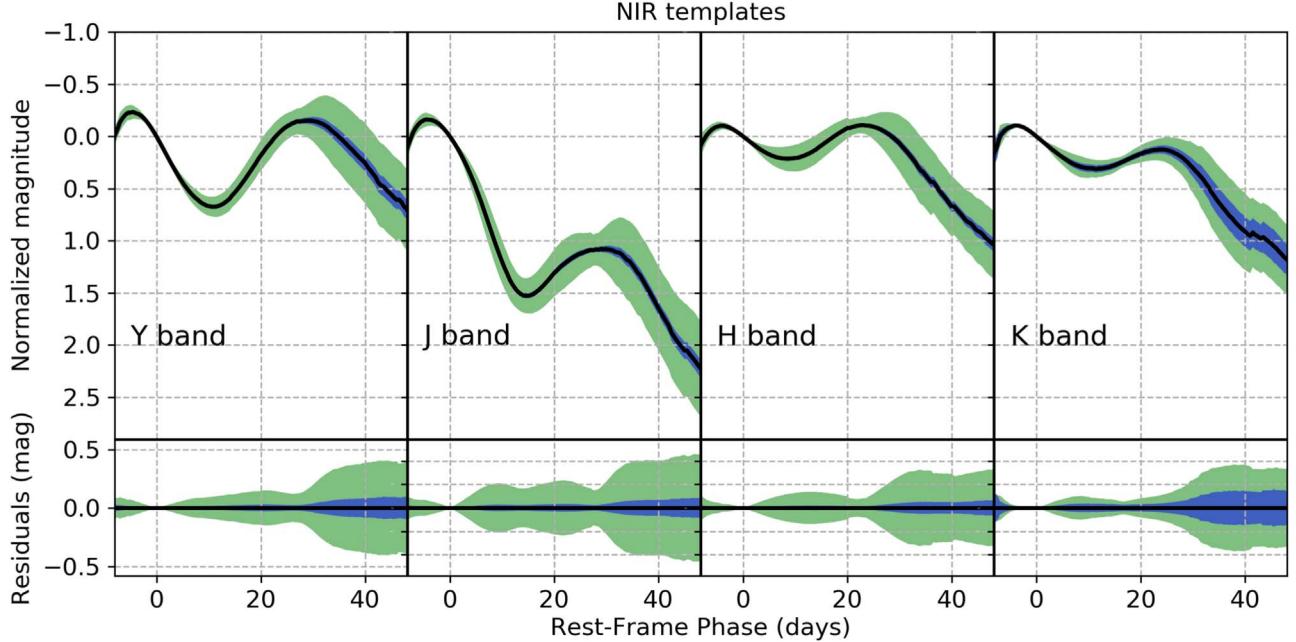
Figure 1. Upper and lower panels show the normalized mean $YJHK_s$ templates and residual plots, respectively. By construction, we normalize the templates so that they have magnitude zero at $t^* = 0$, with reference to the time of B-band maximum light. The numerical values of these templates are tabulated with 1 day sampling in Table 5. The black curves show the normalized mean magnitude $\theta(t^*)$ versus rest-frame phase t^*, while the green and blue bands correspond to the population standard deviation, $\sigma_\theta(t^*)$, and the uncertainty in θ, respectively, determined using the hierarchical Bayesian model and GP method described in Section 3. We use 28, 67, 68, and 25 SNe Ia for which we can determine μ^L as described in Section 3.2 to build the Y, J, H and K_s templates, respectively.

Appendix A, we provide the mathematical details to determine μ^{post} and Σ^{post}.

3.2.1. Normalization of the Gaussian Process Light Curves

Our goal with the GP fitting is to determine the *shape* of the LC to be used later in Section 3.3 to construct NIR templates to fit the data and estimate distance moduli. Once we determine the posterior mean and covariance of the latent absolute magnitude LC for a given SN s using the GP method, we *normalize* the LCs to extract the information about their shape regardless of their absolute magnitudes. The normalized LC $L(t)$ is the function, over phase, of the difference in magnitudes relative to the peak phase, so that $L(t_{B\max}) = 0$.

To estimate the distance moduli, we choose to use the phase of B-band maximum light, $t_{B\max}$, as the reference time to derive the distances. In Section 4.2, we also implement the estimation of distance moduli using the time of NIR-band maximum light instead of $t_{B\max}$ as the reference time.

We define the vector $\boldsymbol{L}$, corresponding to the normalized LC derived from the latent absolute magnitude LC $\boldsymbol{\mathcal{M}}^*$, evaluated on the phase grid $\boldsymbol{t}^*$, as

$$\boldsymbol{L} \equiv \boldsymbol{\mathcal{M}}^* - \mathcal{M}_0 \boldsymbol{1} \qquad (9)$$

where $\mathcal{M}_0$ is the latent absolute magnitude at $t_{B\max}$ and $\boldsymbol{1}$ is a vector of dimension n^* with all its elements equal to one. Since this is a linear transformation of $\boldsymbol{\mathcal{M}}^*$ into $\boldsymbol{L}$, and $\boldsymbol{\mathcal{M}}^*$ is Gaussian, $\boldsymbol{L}$ is also Gaussian and described completely by its mean $\boldsymbol{\mu}^L$ and covariance $\boldsymbol{\Sigma}^L$. See Appendix A.1 for details. In the following section we use ($\boldsymbol{\mu}^L$, $\boldsymbol{\Sigma}^L$) to construct the NIR LC templates.

3.3. Hierarchical Bayesian Model for the Normalized Magnitudes

In this section, we describe how we construct NIR LC templates for the Y, J, H, and K_s bands that correspond to the mean *shape* of SNe Ia LCs in each of these bands. To do so, we combine the normalized LCs described by ($\boldsymbol{\mu}^L$, $\boldsymbol{\Sigma}^L$), from all the SNe at a given phase t^* using a hierarchical Bayesian model to determine the mean normalized magnitude. We then repeat the procedure described below over all the phases in $\boldsymbol{t}^*$ to construct the final NIR LC templates.

First, we assume the normalized magnitude at phase t^*, μ_s^L, for the SN s is drawn from a Gaussian distribution with true value η_s and standard deviation $\sigma_{\eta,s}$,

$$\mu_s^L \sim \mathcal{N}(\eta_s, \sigma_{\eta,s}^2), \qquad (10)$$

where the value of $\sigma_{\eta,s}^2$ is given by the (t_s^*, t_s^*) element in the diagonal of the covariance matrix $\boldsymbol{\Sigma}_s^L$ (see Equation (42)). Next, we assume that the set of values $\{\eta_s\}$ from all the N_T^* SNe at phase t^* are independent draws from a Gaussian population distribution with population mean θ and variance σ_θ^2,

$$p(\{\eta_s\}|\theta, \sigma_\theta^2) = \prod_{s=1}^{N_T^*} \mathcal{N}(\eta_s|\theta, \sigma_\theta^2). \qquad (11)$$

In Appendix B, we write the expression for the joint posterior distribution of the hierarchical model and describe additional decompositions in order to make the computations more tractable to determine the posterior inference[13] of ($\{\eta_s\}$, θ, σ_θ) given the data $\{(\mu_s^L, \sigma_{\eta,s})\}$ at phase t^*.

---

[13] We use the median of the posterior probability distribution as the best estimated value.

Table 5
Normalized $YJHK_s$ LC Templates

t^* (days)	$\theta^{(Y)}$ (mag)	$\sigma_\theta^{(Y)}$ (mag)	$\theta^{(J)}$ (mag)	$\sigma_\theta^{(J)}$ (mag)	$\theta^{(H)}$ (mag)	$\sigma_\theta^{(H)}$ (mag)	$\theta^{(K)}$ (mag)	$\sigma_\theta^{(K)}$ (mag)
−10	0.303 ± 0.067	0.168	0.428 ± 0.037	0.136	0.367 ± 0.047	0.184	0.439 ± 0.290	0.178
−9	0.152 ± 0.034	0.108	0.261 ± 0.025	0.106	0.213 ± 0.032	0.136	0.289 ± 0.335	0.194
−8	−0.007 ± 0.026	0.092	0.092 ± 0.020	0.094	0.075 ± 0.023	0.104	0.150 ± 0.125	0.112
−7	−0.135 ± 0.023	0.092	−0.038 ± 0.015	0.076	−0.010 ± 0.016	0.070	0.001 ± 0.058	0.106
−6	−0.204 ± 0.018	0.078	−0.115 ± 0.013	0.070	−0.065 ± 0.012	0.054	−0.058 ± 0.034	0.066
−5	−0.228 ± 0.016	0.072	−0.153 ± 0.012	0.070	−0.093 ± 0.010	0.046	−0.088 ± 0.021	0.034
−4	−0.224 ± 0.012	0.056	−0.159 ± 0.010	0.060	−0.102 ± 0.007	0.034	−0.103 ± 0.016	0.020
−3	−0.200 ± 0.008	0.042	−0.148 ± 0.008	0.050	−0.092 ± 0.006	0.032	−0.096 ± 0.011	0.014
−2	−0.151 ± 0.005	0.028	−0.116 ± 0.005	0.038	−0.069 ± 0.004	0.024	−0.073 ± 0.008	0.010
−1	−0.082 ± 0.003	0.014	−0.065 ± 0.003	0.022	−0.037 ± 0.002	0.014	−0.040 ± 0.004	0.006
0	0.000 ± 0.000	0.000	0.000 ± 0.000	0.000	0.000 ± 0.000	0.000	0.000 ± 0.000	0.000
1	0.090 ± 0.002	0.012	0.075 ± 0.003	0.024	0.039 ± 0.002	0.016	0.041 ± 0.005	0.014
2	0.184 ± 0.005	0.024	0.162 ± 0.007	0.050	0.079 ± 0.005	0.032	0.083 ± 0.011	0.030
3	0.276 ± 0.007	0.036	0.259 ± 0.010	0.080	0.115 ± 0.007	0.048	0.125 ± 0.017	0.046
4	0.363 ± 0.009	0.050	0.369 ± 0.014	0.108	0.147 ± 0.009	0.064	0.163 ± 0.022	0.062
5	0.441 ± 0.011	0.060	0.492 ± 0.018	0.140	0.173 ± 0.012	0.078	0.200 ± 0.026	0.074
6	0.510 ± 0.013	0.072	0.628 ± 0.022	0.168	0.194 ± 0.013	0.092	0.233 ± 0.030	0.086
7	0.568 ± 0.015	0.080	0.774 ± 0.025	0.188	0.207 ± 0.015	0.104	0.262 ± 0.034	0.096
8	0.612 ± 0.016	0.086	0.921 ± 0.026	0.202	0.214 ± 0.017	0.114	0.284 ± 0.037	0.100
9	0.650 ± 0.016	0.088	1.066 ± 0.028	0.210	0.214 ± 0.018	0.122	0.298 ± 0.037	0.100
10	0.670 ± 0.017	0.092	1.199 ± 0.027	0.208	0.208 ± 0.018	0.128	0.306 ± 0.038	0.094
11	0.676 ± 0.017	0.096	1.316 ± 0.027	0.200	0.198 ± 0.019	0.134	0.309 ± 0.035	0.086
12	0.666 ± 0.019	0.104	1.419 ± 0.026	0.186	0.179 ± 0.020	0.138	0.309 ± 0.035	0.080
13	0.640 ± 0.020	0.108	1.487 ± 0.024	0.170	0.156 ± 0.020	0.138	0.305 ± 0.034	0.078
14	0.600 ± 0.022	0.116	1.525 ± 0.024	0.166	0.127 ± 0.021	0.138	0.295 ± 0.033	0.074
15	0.540 ± 0.023	0.118	1.529 ± 0.024	0.170	0.089 ± 0.019	0.134	0.278 ± 0.032	0.068
16	0.477 ± 0.024	0.126	1.513 ± 0.026	0.182	0.053 ± 0.019	0.128	0.257 ± 0.028	0.058
17	0.409 ± 0.025	0.132	1.478 ± 0.028	0.195	0.017 ± 0.019	0.122	0.234 ± 0.027	0.056
18	0.336 ± 0.026	0.138	1.429 ± 0.029	0.208	−0.018 ± 0.018	0.116	0.211 ± 0.028	0.064
19	0.261 ± 0.026	0.142	1.373 ± 0.030	0.216	−0.049 ± 0.017	0.108	0.188 ± 0.030	0.074
20	0.183 ± 0.027	0.144	1.312 ± 0.032	0.226	−0.079 ± 0.016	0.100	0.169 ± 0.031	0.082
21	0.114 ± 0.029	0.150	1.263 ± 0.033	0.232	−0.091 ± 0.014	0.080	0.149 ± 0.033	0.088
22	0.054 ± 0.028	0.148	1.221 ± 0.034	0.236	−0.102 ± 0.014	0.076	0.138 ± 0.034	0.094
23	−0.007 ± 0.027	0.142	1.183 ± 0.032	0.228	−0.108 ± 0.014	0.082	0.130 ± 0.036	0.100
24	−0.056 ± 0.026	0.134	1.151 ± 0.032	0.218	−0.102 ± 0.016	0.094	0.126 ± 0.039	0.110
25	−0.095 ± 0.025	0.126	1.124 ± 0.029	0.198	−0.092 ± 0.019	0.120	0.132 ± 0.043	0.122
26	−0.123 ± 0.024	0.120	1.106 ± 0.026	0.180	−0.075 ± 0.023	0.152	0.147 ± 0.047	0.134
27	−0.144 ± 0.024	0.124	1.091 ± 0.025	0.170	−0.050 ± 0.027	0.182	0.172 ± 0.054	0.156
28	−0.147 ± 0.026	0.134	1.085 ± 0.024	0.154	−0.018 ± 0.031	0.214	0.205 ± 0.060	0.174
29	−0.151 ± 0.031	0.162	1.081 ± 0.028	0.178	0.021 ± 0.036	0.244	0.248 ± 0.068	0.200
30	−0.149 ± 0.038	0.196	1.082 ± 0.034	0.224	0.067 ± 0.041	0.272	0.302 ± 0.084	0.238
31	−0.137 ± 0.046	0.238	1.090 ± 0.040	0.274	0.124 ± 0.043	0.294	0.356 ± 0.095	0.262
32	−0.115 ± 0.053	0.274	1.112 ± 0.048	0.322	0.183 ± 0.046	0.312	0.414 ± 0.111	0.306
33	−0.083 ± 0.058	0.304	1.134 ± 0.054	0.354	0.248 ± 0.049	0.316	0.484 ± 0.118	0.322
34	−0.038 ± 0.065	0.332	1.186 ± 0.059	0.382	0.324 ± 0.052	0.326	0.566 ± 0.133	0.342
35	0.007 ± 0.070	0.340	1.232 ± 0.063	0.396	0.375 ± 0.052	0.320	0.636 ± 0.138	0.350
36	0.054 ± 0.075	0.356	1.305 ± 0.065	0.408	0.438 ± 0.053	0.320	0.699 ± 0.144	0.358
37	0.105 ± 0.078	0.364	1.378 ± 0.065	0.396	0.472 ± 0.050	0.298	0.762 ± 0.146	0.362
38	0.156 ± 0.077	0.370	1.464 ± 0.068	0.408	0.545 ± 0.050	0.294	0.816 ± 0.148	0.372
39	0.208 ± 0.077	0.372	1.555 ± 0.069	0.408	0.605 ± 0.050	0.294	0.868 ± 0.141	0.368
40	0.256 ± 0.082	0.384	1.647 ± 0.068	0.402	0.672 ± 0.050	0.292	0.912 ± 0.148	0.370
41	0.325 ± 0.084	0.388	1.736 ± 0.069	0.406	0.703 ± 0.049	0.274	0.955 ± 0.142	0.356
42	0.390 ± 0.086	0.396	1.820 ± 0.071	0.418	0.759 ± 0.050	0.282	0.947 ± 0.140	0.334
43	0.469 ± 0.090	0.404	1.922 ± 0.076	0.436	0.818 ± 0.053	0.294	0.981 ± 0.133	0.332
44	0.507 ± 0.094	0.404	1.992 ± 0.077	0.440	0.852 ± 0.055	0.302	0.987 ± 0.149	0.335
45	0.557 ± 0.091	0.400	2.055 ± 0.081	0.454	0.908 ± 0.060	0.312	1.028 ± 0.149	0.338

Note. Mean NIR LC templates in the $YJHK_s$-bands using the hierarchical Bayesian model and Gaussian process method described in Section 3. These are referenced to the time of B-band maximum light, such that $t^* = 0$ at $t_{B\,\mathrm{max}}$. See Figure 1.

We repeat the above procedure for all phases in the range $t^* = (-10, 45)$ days, every 0.5 days, to determine (θ, σ_θ) for all t^* in this range. Figure 1 shows the $YJHK_s$ templates constructed with this procedure and Table 5 reports the numerical values of the templates. The posterior estimates of the population mean and variance of the normalized LC,
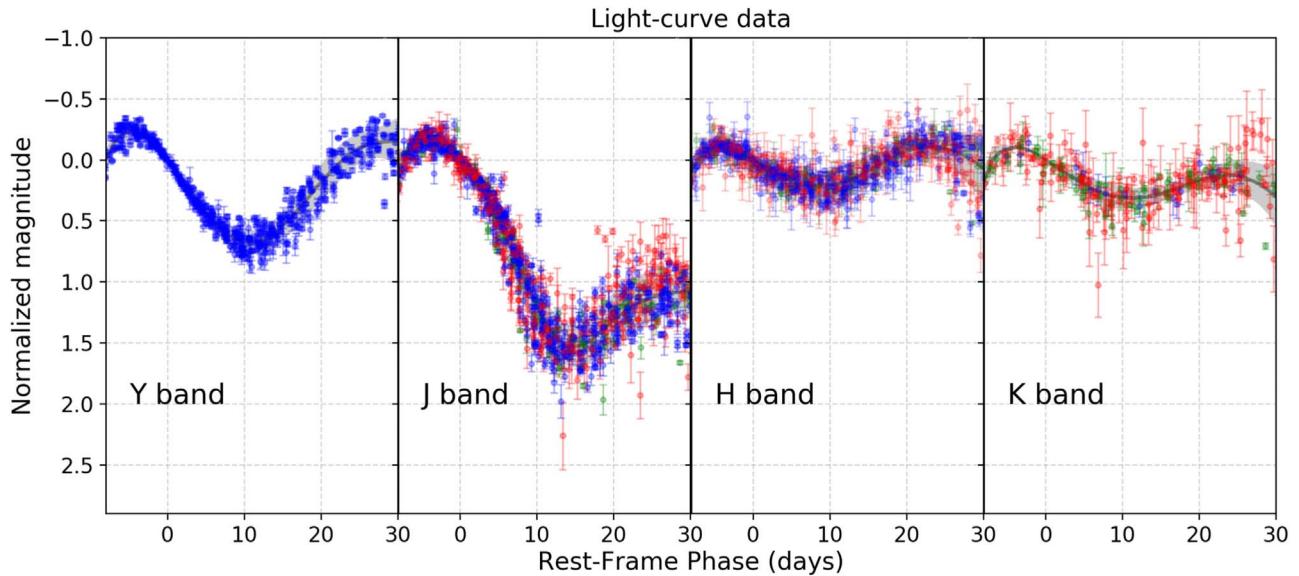
Figure 2. Normalized SNe Ia LC data vs. rest-frame phase t^* for the $YJHK_s$ bands. Points are color coded by NIR photometric data source, including the CfA (red; Wood-Vasey et al. 2008; Friedman et al. 2015), the CSP (blue; Krisciunas et al. 2017), and other data from the literature (green; see Table 2 and references therein). Note that only the CSP used a Y-band filter. The black lines and gray bands in the background correspond to the NIR mean LC templates and population standard deviation shown in Figure 1. The data for each supernova s were normalized by subtracting the estimated apparent magnitude, $\hat{m}_{0,s}$, obtained from the template fit from the apparent magnitude LC. The template fit in the plot is limited to the rest-frame phase range of $(-8, 30)$ days, since this was the phase range of data that minimized the scatter in the Hubble Diagram residuals using the template method discussed in Sections 3–4. Data beyond >30 days were used to help fit the mean LC template in Figure 1, but the increased scatter at those phases limited the utility of that phase range for distance estimates.

$(\theta, \sigma_\theta^2)$, and the uncertainty in the determination of θ are shown in Figure 1 as black curves, green bands, and blue bands, respectively.

4. Hubble Diagram

We implement two different methods to derive the distance modulus for each SN from the NIR LCs. We refer to these as the *template method* and the *Gaussian-process method*. The GP method requires data near the NIR maximum for all NIR bands being used, while the template method works for arbitrarily sampled data, even if the LC is sparse near maximum. For this reason, we have more objects in the template method Hubble diagrams. We describe these methods in more detail in the following sections.

All of these NIR-only approaches approximately treat the information in each of the $YJHK_s$ bands as independent. However, this simple approach does not take maximal advantage of the cross-band correlations between each of the NIR and optical bands, as is done using a more sophisticated hierarchical Bayesian model (e.g., BAYESN: Mandel et al. 2009, 2011, 2014). Nor does this approach use the fact that there is only one true distance to the SN.

To alleviate this problem, we also derive the distance modulus for each SN from the combined distance moduli in each NIR band. However, instead of computing a simple average distance modulus from the individual distance moduli, we instead estimate the covariance matrix of the $YJHK_s$ distance moduli (and submatrices of it) and then derive the weighted average distance modulus. The advantage of this procedure is that it takes into account the correlations among the magnitudes in the NIR bands and then derives more realistic mean distance moduli and their uncertainties. More details are in Section 4.3.

For our NIR-only Hubble diagrams, only NIR LCs are used to directly construct distance moduli. However, auxiliary optical data are used to estimate $t_{B\,\max}$, $\Delta m_{15}(B)$, and mangled K-corrections, and are employed in the input data selection cuts described in Section 2.1.

We make the scripts that were written to perform the analysis presented in this work publicly available at: https://github.com/ArturoAvelino/SNIRfit.

4.1. Distance Modulus: Template Method

To determine the photometric distance modulus μ_s of the SN s in a given NIR band, we use the normalized mean template, θ, computed in Section 3 to determine the apparent magnitude at phase zero, $m_{0,s} \equiv m_s(t = 0)$, by fitting the template to the sometimes sparse photometric LC data $\{m_s(t)\}$. We define the difference

$$\Delta m_s(t) \equiv m_s(t) - \theta(t) - m_{0,s}, \qquad (12)$$

where $m_s(t)$ and $\theta(t)$ are the apparent magnitude and the magnitude of the normalized template at phase t, respectively. We can express this difference for all the n phases in a given LC as the vector,

$$\Delta \boldsymbol{m}_s \equiv \begin{pmatrix} \Delta m_s(t_1) \\ \Delta m_s(t_2) \\ \vdots \\ \Delta m_s(t_n) \end{pmatrix}. \qquad (13)$$

Subsequently, to determine $m_{0,s}$ we minimize the negative of the log likelihood function $\mathcal{L}(m_{0,s})$ defined as

$$-2 \ln \mathcal{L}(m_{0,s}) = \Delta \boldsymbol{m}_s^\top \cdot \boldsymbol{C}^{-1} \cdot \Delta \boldsymbol{m}_s + \text{constant}, \qquad (14)$$

where $\boldsymbol{C}$ is the n-dimensional covariance matrix where the (t_i, t_j) component is given by:

$$C_{ij} \equiv \text{Cov}(\Delta m_s(t_i), \Delta m_s(t_j)) \qquad (15)$$

Table 6
Mean $YJHK_s$ Absolute Magnitudes at $t_{B\,max}$ or t_{NIR} Max

Band	N_{SN}	$\langle M \rangle$ (mag)	Std. Deviation (mag)
		Template method	
Y	44	-18.12	0.15
J	87	-18.34	0.17
H	81	-18.18	0.17
K_s	32	-18.35	0.21
		GP method at NIR max	
Y	29	-18.39	0.11
J	52	-18.52	0.14
H	44	-18.30	0.11
K_s	14	-18.37	0.18
		GP method at B max	
Y	29	-18.16	0.12
J	52	-18.34	0.15
H	44	-18.19	0.12
K_s	14	-18.28	0.17

Note. We use the sample mean values of the absolute magnitudes, $\langle M \rangle$, in each band to determine the distance modulus in the template and GP methods using Equations (19) and (23), respectively. For the template method $\langle M \rangle \equiv \langle M_0 \rangle$ and for the GP method $\langle M \rangle \equiv \langle M_{NIRmax} \rangle$, $\langle M_{B\,max} \rangle$. Figures 3–5 show the histograms of $M_{0,s}$ and $M_{NIRmax,s}$, respectively. In this table, we also present the sample standard deviation of the absolute magnitude sample distribution just as a reference; we do not use those values in any part of the computations.

$$= \sigma_\theta(t_i)\,\sigma_\theta(t_j)\exp\left[-\frac{(t_i - t_j)^2}{2l^2}\right] + \hat{\sigma}_{m,s}^2(t_i)\,\delta_{ij}, \qquad (16)$$

where $\sigma_\theta(t)$ is the population standard deviation of the sample distribution of magnitudes at phase t, determined from Equation (45) during the training process used to construct the mean LC template, $\hat{\sigma}_{m,s}^2(t_i)$ is the photometric error of the datum $m_s(t_i)$, and l is the hyperparameter of the GP kernel determined from Equation (40) and with values shown in Table 16.

From Equation (14), we can calculate an analytic expression for the maximum likelihood estimator (MLE) of the apparent magnitude at B-band maximum light, $\hat{m}_{0,s}$, given by:

$$\hat{m}_{0,s} = \left[\sum_{i,j}^n (C^{-1})_{ij}\right]^{-1} \times \sum_i^n \left[(m_s(t_i) - \theta(t_i))\sum_j^n (C^{-1})_{ij}\right], \qquad (17)$$

with the MLE of the uncertainty of $\hat{m}_{0,s}$ given as

$$\hat{\sigma}_{fit,s} = \left[\sum_{i,j}^n (C^{-1})_{ij}\right]^{-1/2}, \qquad (18)$$

which corresponds to the fitting error of the light curve. This error incorporates the photometric measurement error and the sparsity of the actual data points.
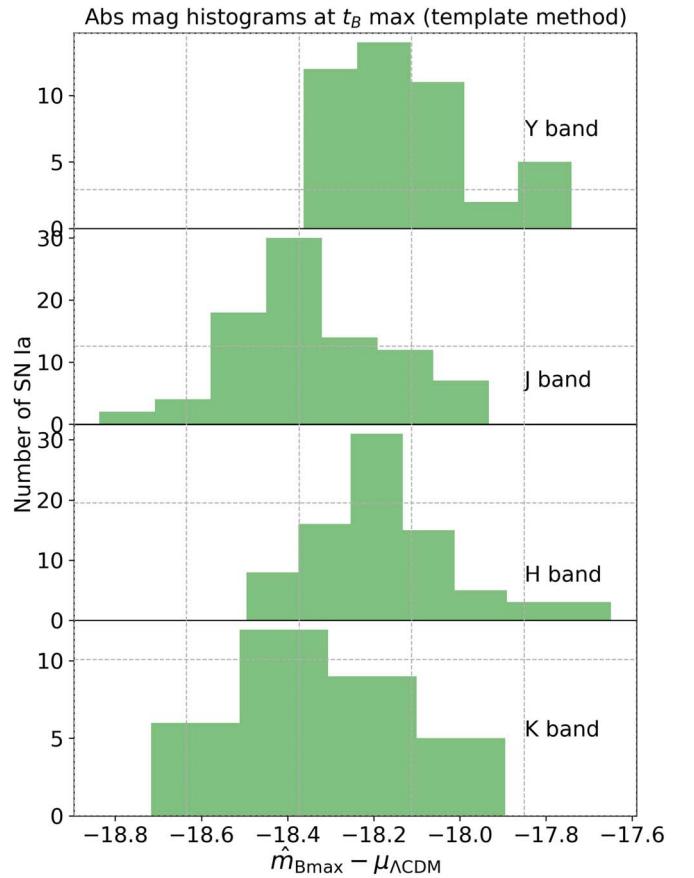
Figure 3. Histograms of the absolute magnitudes at phase zero ($t^* = t_{B\,max}$), defined as $M_{0,s} \equiv \hat{m}_{0,s} - \mu_{\Lambda CDM}(z_s)$ for the SNe Ia sample using the template method. The sample mean, standard deviation, and the number of SNe in each histogram are shown in Table 6.

Now, from the distribution of absolute magnitudes at phase zero estimated as $M_{0,s} \equiv \hat{m}_{0,s} - \mu_{\Lambda CDM}(z_s)$ (see Figure 3), we compute the sample mean absolute magnitude, $\langle M_0 \rangle$, and the sample standard deviation of the distribution, obtaining the values reported in Table 6. The sample standard deviation describes the total scatter of the absolute magnitude estimates. Below, we decompose this into the contributions from peculiar-velocity distance errors, measurement/fitting errors, and intrinsic dispersion.

Finally, we estimate the photometric distance modulus for SN s in a given NIR band as

$$\hat{\mu}_s = \hat{m}_{0,s} - \langle M_0 \rangle. \qquad (19)$$

The uncertainty on $\hat{\mu}_s$ is composed of two sources of error: the fitting uncertainty $\hat{\sigma}_{fit,s}$ estimated in Equation (18) for each individual SN, and the *intrinsic scatter*, σ_{int}, which primarily comes from the intrinsic variation of SNe Ia absolute magnitudes and is estimated by fitting an entire sample of SNe Ia on the Hubble diagram (see Appendix C for more details). The variance of the photometric distance modulus is therefore given as

$$\hat{\sigma}_{\mu,s}^2 = \hat{\sigma}_{fit,s}^2 + \hat{\sigma}_{int}^2. \qquad (20)$$

The Hubble residual for SN s is defined as

$$\Delta\mu_s \equiv \hat{\mu}_s - \mu_{\Lambda CDM}(z_s). \qquad (21)$$

The uncertainty on $\mu_{\Lambda CDM}(z_s)$ is given by Equation (8). The variance on the Hubble residual for SN s, $\sigma_{\Delta,s}^2$, comes from the

Table 7
Hubble Residual Intrinsic Scatter, $\sigma_{\rm int}$, and rms

Band	Method	$N_{\rm SN}$	$\sigma_{\rm int}$ (mag) ($\sigma_{\rm pec} = 150$ km s^{-1})	$\sigma_{\rm int}$ (mag) ($\sigma_{\rm pec} = 250$ km s^{-1})	wrms (mag) ($\sigma_{\rm pec} = 150$ km s^{-1})	rms (mag)
Optical *BVR*	SALT2	56	0.133 ± 0.022	0.107 ± 0.025	0.174 ± 0.020	0.179 ± 0.018
Optical *BVR*	SNooPy	56	0.128 ± 0.018	0.111 ± 0.020	0.159 ± 0.019	0.174 ± 0.021
Any *YJHK$_s$*	Template	56	0.112 ± 0.016	0.096 ± 0.019	0.140 ± 0.016	0.138 ± 0.014
Any *YJHK$_s$*	GP (NIR max)	56	0.047 ± 0.018	$0.000 \pm 0.000^{\rm a}$	0.100 ± 0.013	0.117 ± 0.014
Any *YJHK$_s$*	GP (*B* max)	56	0.066 ± 0.016	0.044 ± 0.023	0.106 ± 0.010	0.115 ± 0.011

Notes. We compare the Hubble residual scatter for the optical and NIR bands using exactly the same 56 SNe for several methods. We compute the intrinsic scatter, $\sigma_{\rm int}$ (see Appendix C), the inverse-variance wrms, and the simple rms, using two standard LC fitters: SALT2 (Guy et al. 2007) and SNooPy (Burns et al. 2011) to fit the optical *BVR*-band LC data, as well as the three NIR methods implemented in this work: NIR LC templates at *B*-max [Template], and GP regression at NIR-max [GP (NIR max) or *B*-band maximum [GP (*B* max)]. We are limited to 56 SNe Ia because these are all the SNe that we can fit using the GP method. Columns 4 and 5 show $\sigma_{\rm int}$, assuming $\sigma_{\rm pec} = 150$ and 250 km s^{-1}, respectively. The estimated intrinsic scatter $\sigma_{\rm int}$ decreases as the assumed peculiar-velocity uncertainty $\sigma_{\rm pec}$ increases from commonly assumed values of 150 km s^{-1} (Radburn-Smith et al. 2004) to 250 km s^{-1} (Scolnic et al. 2018), making $\sigma_{\rm int}$ somewhat model dependent. By contrast, the wrms value only changes by thousandths of a magnitude for $\sigma_{\rm pec}$ in the same range. Column 6 shows the wrms assuming $\sigma_{\rm pec} = 150$ km s^{-1}. Column 7 shows the simple rms, which makes no assumptions about error weighting and does not depend on $\sigma_{\rm pec}$. Both optical methods apply LC shape and dust corrections but still yield a larger scatter than the NIR methods quantified with either the $\sigma_{\rm int}$, wrms, or rms (see also Table 8). Figures 7–10 show Hubble diagrams and residuals for this subsample.
[a] For $\sigma_{\rm pec} = 250$ km s^{-1}, the estimated value of $\sigma_{\rm int}$ is consistent with zero. See the paragraph below Equation (B.7) in Blondin et al. (2011) for the explicit approximation we use to estimate the uncertainty, which breaks down at $\sigma_{\rm int} = 0$.

Table 8
Hubble Residual Intrinsic Scatter, $\sigma_{\rm int}$, and rms

Band	Method	$N_{\rm SN}$	$\sigma_{\rm int}$ (mag) ($\sigma_{\rm pec} = 150$ km s^{-1})	$\sigma_{\rm int}$ (mag) ($\sigma_{\rm pec} = 250$ km s^{-1})	wrms (mag) ($\sigma_{\rm pec} = 150$ km s^{-1})	rms (mag)
Y	Template	44	0.105 ± 0.018	0.093 ± 0.021	0.139 ± 0.013	0.152 ± 0.016
Y	GP (NIR max)	29	0.066 ± 0.020	0.037 ± 0.032	0.102 ± 0.015	0.111 ± 0.018
Y	GP (*B* max)	29	0.080 ± 0.019	0.062 ± 0.024	0.110 ± 0.013	0.118 ± 0.017
J	Template	87	0.136 ± 0.016	0.122 ± 0.018	0.170 ± 0.013	0.175 ± 0.013
J	GP (NIR max)	52	0.107 ± 0.017	0.090 ± 0.021	0.136 ± 0.017	0.139 ± 0.016
J	GP (*B* max)	52	0.124 ± 0.019	0.110 ± 0.021	0.153 ± 0.020	0.151 ± 0.021
H	Template	81	0.126 ± 0.016	0.112 ± 0.018	0.162 ± 0.015	0.166 ± 0.016
H	GP (NIR max)	44	0.032 ± 0.027	$0.000 \pm 0.000^{\rm a}$	0.095 ± 0.010	0.114 ± 0.015
H	GP (*B* max)	44	0.063 ± 0.020	0.037 ± 0.033	0.111 ± 0.011	0.120 ± 0.013
K	Template	32	0.175 ± 0.032	0.163 ± 0.035	0.211 ± 0.023	0.207 ± 0.020
K	GP (NIR max)	14	0.093 ± 0.054	0.077 ± 0.060	0.163 ± 0.033	0.179 ± 0.029
K	GP (*B* max)	14	0.094 ± 0.054	0.059 ± 0.069	0.162 ± 0.035	0.170 ± 0.027
Any *YJHK$_s$*	Template	89	0.123 ± 0.014	0.107 ± 0.016	0.154 ± 0.013	0.161 ± 0.013
JH	Template	81	0.127 ± 0.015	0.112 ± 0.017	0.158 ± 0.015	0.164 ± 0.015
JH	GP (NIR max)	42	0.039 ± 0.024	$0.000 \pm 0.000^{\rm a}$	0.096 ± 0.011	0.114 ± 0.016
JH	GP (*B* max)	42	0.069 ± 0.019	0.046 ± 0.028	0.112 ± 0.014	0.118 ± 0.015
YJH	Template	40	0.093 ± 0.018	0.080 ± 0.022	0.121 ± 0.013	0.137 ± 0.018
YJH	GP (NIR max)	21	0.044 ± 0.028	$0.000 \pm 0.000^{\rm a}$	0.088 ± 0.014	0.087 ± 0.013
YJH	GP (*B* max)	21	0.068 ± 0.023	0.056 ± 0.031	0.097 ± 0.014	0.098 ± 0.014

Notes. Scatter in the Hubble residuals for different NIR band subsets, quantified by the intrinsic scatter, $\sigma_{\rm int}$, the wrms, and the simple rms, using three methods: NIR LC templates at *B*-max (Template), GP regression at NIR-max [GP (NIR max)], or *B*-band maximum [GP (*B* max)]. Column 3 shows the number of SNe Ia in each Hubble diagram. Also see Table 7. Columns 4 and 5 show $\sigma_{\rm int}$, assuming $\sigma_{\rm pec} = 150$ and 250 km s^{-1}, respectively. Note that by increasing the value of $\sigma_{\rm pec}$, the $\sigma_{\rm int}$ decreases even to zero in some cases with uncertainty denoted by 0.000. For the GP method, we use exactly the same SNe at *B*-max or NIR-max. For all NIR band subsets, the GP (NIR max) method produces the smallest scatter, followed by the GP (*B*-max) method, while the template method always yields the largest scatter and wrms. Figures 6–9 and 12–14 show Hubble diagrams and residuals for most of the NIR subsets listed in this table.
[a] For $\sigma_{\rm pec} = 250$ km s^{-1}, the estimated value of $\sigma_{\rm int}$ in these cases is consistent with zero. See the paragraph below Equation (B.7) in Blondin et al. (2011) for the explicit approximation we use to estimate the uncertainty, which breaks down at $\sigma_{\rm int} = 0$.

propagation of uncertainties on $\hat{\mu}_s$ and $\mu_{\Lambda{\rm CDM}}(z_s)$, that is,

$$\sigma^2_{\Delta,s} = \hat{\sigma}^2_{{\rm fit},s} + \hat{\sigma}^2_{\rm int} + \sigma^2_{\mu_{\rm pec},s}. \qquad (22)$$

In addition to $\sigma_{\rm int}$, to quantify the dispersion in the Hubble residuals, we also compute both the rms and the inverse-variance weighted rms (wrms, see Appendix C). The rms and wrms are measures of the total scatter in the Hubble diagram.

The wrms is relatively insensitive to the assumed value of the peculiar-velocity uncertainty, and the formula for the rms does not depend on the assumed value of $\sigma_{\rm pec}$ at all and is therefore more straightforward to compare with other works.

For the template method, the values of $\hat{\mu}_s$, $\sigma_{\rm int}$, and wrms in the Hubble diagram residual for a given NIR band depend on the phase range of the NIR LC template used to determine the distance modulus. We found that phase range of $t^* = (-8, 30)$

Table 9
Hubble Residual Intrinsic Scatter, $\sigma_{\rm int}$, and rms

Band	Subsample	Method	$N_{\rm SN}$	$\sigma_{\rm int}$ (mag) ($\sigma_{\rm pec} = 150$ km s^{-1})	wrms (mag) ($\sigma_{\rm pec} = 150$ km s^{-1})	rms (mag)
J	CfA	Template	29	0.142 ± 0.029	0.179 ± 0.023	0.179 ± 0.022
J	CSP	Template	48	0.129 ± 0.020	0.160 ± 0.017	0.166 ± 0.019
J	Others	Template	10	0.159 ± 0.055	0.196 ± 0.046	0.201 ± 0.039
J	CfA	GP (NIR max)	15	0.125 ± 0.037	0.158 ± 0.040	0.149 ± 0.032
J	CSP	GP (NIR max)	31	0.094 ± 0.019	0.118 ± 0.015	0.113 ± 0.014
J	Others	GP (NIR max)	6	0.156 ± 0.071	0.195 ± 0.056	0.217 ± 0.053
J	CfA	GP (B max)	15	0.146 ± 0.044	0.182 ± 0.045	0.172 ± 0.043
J	CSP	GP (B max)	31	0.110 ± 0.020	0.129 ± 0.015	0.119 ± 0.013
J	Others	GP (B max)	6	0.188 ± 0.078	0.221 ± 0.092	0.226 ± 0.076
H	CfA	Template	27	0.173 ± 0.033	0.205 ± 0.029	0.200 ± 0.029
H	CSP	Template	44	0.102 ± 0.018	0.135 ± 0.017	0.140 ± 0.019
H	Others	Template	10	0.094 ± 0.053	0.147 ± 0.032	0.170 ± 0.036
H	CfA	GP (NIR max)	13	$0.000 \pm 0.000^{*}$	0.107 ± 0.019	0.116 ± 0.021
H	CSP	GP (NIR max)	25	0.041 ± 0.027	0.088 ± 0.013	0.085 ± 0.012
H	Others	GP (NIR max)	6	$0.000 \pm 0.000^{*}$	0.106 ± 0.035	0.189 ± 0.051
H	CfA	GP (B max)	13	$0.000 \pm 0.000^{*}$	0.106 ± 0.021	0.108 ± 0.018
H	CSP	GP (B max)	25	0.071 ± 0.023	0.107 ± 0.013	0.101 ± 0.012
H	Others	GP (B max)	6	0.052 ± 0.119	0.135 ± 0.042	0.195 ± 0.042

Note. Dispersion in the J- and H-band Hubble residuals by subsample (See caption of Figure 8). In most cases, the CSP JH data yield smaller values of the various measures of dispersion (intrinsic scatter, wrms, and rms) than the data from the CfA or Others subsamples, while the CfA subsample yields smaller dispersions than the Others subsample. The uncertainties on the dispersions are smaller for the CSP versus CfA samples because the photometric uncertainties for the CSP data are typically at least two to three times smaller at the brightest light-curve point than the CfA data (Friedman et al. 2015). However, for each Hubble diagram method in Table 9 (Template, NIR max, B max), for both the J- and H bands, the dispersions are still consistent with one another to within 1–2σ for the CSP, CfA, and Others subsamples. For the Y and K_s bands, all or most of the data is from the CSP and CfA, respectively, so it is either impossible (Y-band) or not useful (K-band) to perform similar comparisons for these subsamples.

days in each of the $YJHK_s$ bands minimized the scatter in the Hubble residual, as measured by $\sigma_{\rm int}$ or wrms.

Tables 7–9 report the dispersion in the Hubble residuals when using the template method to derive distance moduli from the NIR bands, in the rows labeled "Template" under the Method column. Section 4.2 describes an additional method to derive distance moduli by determining the apparent magnitude at either the B-band maximum or NIR-band maximum using GP, for which we compare the scatter in Table 10. Section 4.4 uses two well-known methods to derive distance moduli from the optical BVR bands and computes the scatter in the Hubble residuals, which we compare to that found using the GP method at the NIR maximum in Table 11.

Table 12 reports the distance moduli $\hat{\mu}_s$ and their fitting uncertainty $\hat{\sigma}_{{\rm fit},s}$ that we obtain with this procedure for each SN in each band.

4.2. Distance Modulus: GP Method

The nearby low-z NIR sample now contains a sufficient number of well-sampled SNe Ia around maximum light in the $YJHK_s$-bands. We can therefore now also explore referencing various distance estimation approaches to the times of these NIR maxima, rather than B-max, for which there has long been sufficiently well-sampled optical photometry.

An alternative approach that we implement to derive distance moduli is to determine the apparent magnitude at the time of NIR maximum light, $t_{\rm NIRmax}$, and B maximum light, $t_{B\,{\rm max}}$, using the GP technique to interpolate the LC data. The method follows the same procedure as the one described in

Section 3.2, but instead of GP fitting the absolute magnitude LCs, $\{M_s(t)\}$, we directly GP fit the *apparent* magnitude LCs, $\{m_s(t)\}$. By doing this, we do not include $\sigma_{\mu_{\rm pec}}$ in the error budget for each $m_s(t)$ because we do not subtract $\mu_{\Lambda{\rm CDM}}(z)$.

To determine the posterior mean of the apparent magnitude LC, $\{\bar{m}_s(t^*)\}$, and the posterior covariance of a GP fit to $\{m_s(t)\}$ we use Equations (38) and (39) where we set $\sigma^2_{\mu_{\rm pec},s} = 0$. For each LC, we use the average of the apparent magnitude data as the GP prior mean, and use the same values for the hyperparameters of the GP kernel shown in Table 16, given that the shape and dispersion of the apparent magnitude LC data is very similar to the absolute magnitude LCs we fitted with GP in Section 3.2 for each SN. We verified that the GP fits to the LCs are insensitive to these choices.

We only consider LCs that have data around $t_{\rm NIRmax}$ or $t_{B\,{\rm max}}$ so that we can determine the GP fit at those references phases. By construction, $t_{B\,{\rm max}}$ corresponds to a rest-frame phase $t^* = 0$ days. To determine the NIR maximum using the GP method, we require LCs to have at least one data point observed at a phase $t_{\rm NIRmax} < -2.5$ days. This requirement excludes 33 of the 89 SNe Ia used in the template-method sample, leaving us with only 56 SNe Ia that are suitable for the GP method.

We also limit the search for the maximum to the phase range $-8.5 < t_{\rm NIRmax} < -2.5$ days to remove cases where the maximum of the GP posterior mean happens *after* $t_{B\,{\rm max}}$, which we found can be an artifact of the GP fit when there are too few data points before $t_{B\,{\rm max}}$. For the rest of this section we denote the subscripts "NIRmax" and "Bmax" simply as "max."

From each set $\{\bar{m}_s(t^*)\}$, we estimate, $\hat{m}_{{\rm max},s}$, the GP interpolated apparent magnitude at $t_{{\rm max},s}$. We then estimate

Table 10
Gaussian Process Method Intrinsic Scatter for *B* Max vs. NIR Max

NIR Band(s)	$\Delta\sigma_{\rm int}$ (mag)	$n - \sigma$	Δwrms (mag)	$n - \sigma$	Δrms (mag)	$n - \sigma$
Y	0.014 ± 0.028	0.49	0.009 ± 0.020	0.42	0.007 ± 0.025	0.26
J	0.018 ± 0.025	0.70	0.017 ± 0.026	0.65	0.012 ± 0.026	0.46
H	0.031 ± 0.034	0.92	0.016 ± 0.014	1.12	0.006 ± 0.020	0.32
K_s	0.001 ± 0.076	0.01	-0.001 ± 0.048	-0.03	-0.009 ± 0.040	-0.23
Any $YJHK_s$	0.019 ± 0.024	0.77	0.006 ± 0.016	0.38	-0.002 ± 0.018	-0.10
JH	0.030 ± 0.031	0.99	0.016 ± 0.018	0.89	0.004 ± 0.021	0.17
YJH	0.024 ± 0.037	0.66	0.008 ± 0.020	0.41	0.011 ± 0.019	0.58

Note. Similar to Table 10, we show $\Delta\sigma_{\rm int}$, Δwrms, and Δrms, defined here as the difference in Hubble residuals scatter between the Gaussian process method referenced to *B* max or NIR max. As in Table 10, the uncertainties are given by the quadrature sum of the $\sigma_{\rm int}$ or wrms uncertainties from columns 4 or 6 of Tables 7 and 8 for $\sigma_{\rm pec} = 150$ km s^{-1}. Columns 3, 5, and 7 show $n - \sigma$ defined as the number *n* of standard deviations σ by which the NIR data referenced to NIR max yields *smaller* intrinsic scatter, wrms, or rms than when referenced to *B*-max, respectively. For every individual band and subset of NIR bands, the GP method yields smaller estimated intrinsic scatter when referencing to NIR max instead of *B* max, where the largest difference is $n - \sigma = 0.99\sigma$ for *JH* band. This trend is also observed when comparing the wrms values, again excluding K_s band where our sample lacks enough data to draw meaningful conclusions.

the distance modulus as

$$\hat{\mu}_s = \hat{m}_{{\rm max},s} - \langle M_{\rm max} \rangle, \tag{23}$$

where $\langle M_{\rm max} \rangle$ is the mean absolute magnitude at $t_{{\rm max},s}$ from all the SNe in a given NIR band (see Figures 4 and 5), with $M_{{\rm max},s} \equiv \hat{m}_{{\rm max},s} - \mu_{\Lambda{\rm CDM}}(z_s)$. The uncertainty on the photometric distance modulus $\hat{\mu}_s$ in this case is $\hat{\sigma}_{{\rm fit},s}$, which is equal to the uncertainty in the apparent magnitude at $t_{{\rm max},s}$ inferred from the GP fit to the LC.

Table 13 shows the distance moduli inferred from the GP method for each of the *Y*, *J*, *H*, and K_s bands.

4.3. Distance Modulus from the Combined NIR Bands

From the estimated distance moduli ($\hat{\mu}_s^Y$, $\hat{\mu}_s^J$, $\hat{\mu}_s^H$, $\hat{\mu}_s^K$) for a given SN *s* determined from each NIR band using either of the three methods described above, we estimate the weighted average of the distance modulus μ_s from each method. First we define the vector of residuals

$$\delta\boldsymbol{\mu}_s \equiv \begin{pmatrix} \hat{\mu}_s^Y - \mu_s \\ \hat{\mu}_s^J - \mu_s \\ \hat{\mu}_s^H - \mu_s \\ \hat{\mu}_s^K - \mu_s \end{pmatrix}, \tag{24}$$

where $\hat{\mu}_s^Y$, $\hat{\mu}_s^J$, $\hat{\mu}_s^H$, $\hat{\mu}_s^K$ are determined by either Equations (19) or (23), for the template or GP methods, respectively. Then, to estimate μ_s, we minimize the negative of the likelihood function $\mathcal{L}(\mu_s)$ defined as

$$-2\ln\mathcal{L}(\mu_s) = \delta\boldsymbol{\mu}_s^\top \cdot C_\mu^{-1} \cdot \delta\boldsymbol{\mu}_s + {\rm constant}, \tag{25}$$

where C_μ is the sample covariance matrix computed from the Hubble residuals (see Equation (21)) $\{\Delta\mu_s^Y, \Delta\mu_s^J, \Delta\mu_s^H, \Delta\mu_s^K\}$, the collection of distance-modulus residuals from all SNe Ia with observations in the four $YJHK_s$ bands. For supernovae with observations in only three, two, or one bands, we construct the respective covariance matrices based on those SN subsamples, and the vector defined in Equation (24) becomes three-, two-, or one-dimensional, respectively. In Appendix D, we provide numerical values of the covariance matrix C_μ for these different subcases.

We derive an analytic expression for the minimization of Equation (25) with respect to μ_s and obtain the maximum likelihood estimate for the combined distance modulus given by,

$$\hat{\mu}_s = \sum_b w_b \, \hat{\mu}_s^b, \tag{26}$$

where $\hat{\mu}_s^b \in \{\hat{\mu}_s^Y, \hat{\mu}_s^J, \hat{\mu}_s^H, \hat{\mu}_s^K\}$ (the index *b* stands for *band*), and

$$w_b = \left[\sum_{b'}(C^{-1})_{bb'}\right] \times \left[\sum_{b',b''}(C^{-1})_{b'b''}\right]^{-1}. \tag{27}$$

Now, assuming that the uncertainties in the distance modulus estimated from each individual $YJHK_s$ band, $\hat{\sigma}_{{\rm fit},s,Y}$, $\hat{\sigma}_{{\rm fit},s,J}$, $\hat{\sigma}_{{\rm fit},s,H}$, $\hat{\sigma}_{{\rm fit},s,K}$, are independent between bands *b* and also independent of the intrinsic scatter $\sigma_{\rm int}$, then we can propagate the uncertainty in the combined distance modulus due to the fitting only as:

$$\hat{\sigma}_{{\rm fit},s} = \sqrt{\sum_b w_b^2 \, \hat{\sigma}_{s,b}^2}, \tag{28}$$

where $\hat{\sigma}_{s,b} \equiv \hat{\sigma}_{{\rm fit},s,Y}$, $\hat{\sigma}_{{\rm fit},s,J}$, $\hat{\sigma}_{{\rm fit},s,H}$, $\hat{\sigma}_{{\rm fit},s,K}$.

The last column in Tables 12–14 shows the combined distance moduli we obtain with this procedure for the template and GP methods, respectively. The reported uncertainties correspond to $\hat{\sigma}_{{\rm fit},s}$ in all cases. Figures 6–9 show the Hubble diagrams and residuals from combining the NIR distance moduli.

4.4. Distance Modulus from Optical Bands

We wish to assess how well the SNe Ia observed in NIR bands perform as standard candles, specifically when using $t_{\rm NIRmax}$ as opposed to $t_{B\,{\rm max}}$, as the time reference to estimate their distance. To do so, we determine the distance moduli using only *optical BVR*-band LCs for exactly the same 56 SNe in the "any $YJHK_s$" Hubble diagram set that was used for the GP method (see left panel in Figure 7 and the SN listed in Table 13). We can then compare the intrinsic scatter and rms or wrms in the Hubble-diagram residuals between the optical-only and NIR-only Hubble diagrams. A smaller intrinsic scatter, wrms, or rms, including the uncertainties, would indicate evidence that SNe Ia are better standard candles using that data and Hubble diagram construction method.

Table 11
Optical-NIR Intrinsic Scatter

Optical *BVR* Method–NIR band(s)	$\Delta\sigma_{int}$ (mag)	$n - \sigma$	Δwrms (mag)	$n - \sigma$	Δrms (mag)	$n - \sigma$
SALT2–*Y*	0.067 ± 0.029	2.3	0.073 ± 0.025	2.9	0.068 ± 0.026	2.6
SNooPy–*Y*	0.062 ± 0.027	2.3	0.057 ± 0.024	2.4	0.063 ± 0.028	2.2
SALT2–*J*	0.027 ± 0.028	1.0	0.038 ± 0.026	1.5	0.040 ± 0.024	1.6
SNooPy–*J*	0.021 ± 0.025	0.8	0.023 ± 0.025	0.9	0.035 ± 0.027	1.3
SALT2–*H*	0.101 ± 0.035	2.9	0.079 ± 0.022	3.6	0.065 ± 0.023	2.8
SNooPy–*H*	0.095 ± 0.033	2.9	0.063 ± 0.021	3.0	0.060 ± 0.026	2.3
SALT2–K_s	0.040 ± 0.058	0.7	0.011 ± 0.039	0.3	0.000 ± 0.035	0.0
SNooPy–K_s	0.034 ± 0.057	0.6	-0.005 ± 0.038	-0.1	-0.005 ± 0.036	-0.1
SALT2-any $YJHK_s$	0.086 ± 0.028	3.0	0.074 ± 0.024	3.2	0.062 ± 0.023	2.7
SNooPy–any $YJHK_s$	0.080 ± 0.026	3.1	0.059 ± 0.023	2.6	0.057 ± 0.025	2.3
SALT2–*JH*	0.095 ± 0.032	2.9	0.078 ± 0.023	3.5	0.065 ± 0.024	2.7
SNooPy–*JH*	0.089 ± 0.030	2.9	0.062 ± 0.022	2.8	0.060 ± 0.026	2.3
SALT2–*YJH*	0.089 ± 0.036	2.5	0.086 ± 0.024	3.5	0.092 ± 0.022	4.1
SNooPy–*YJH*	0.084 ± 0.034	2.5	0.070 ± 0.024	3.0	0.087 ± 0.025	3.5

Note. We show $\Delta\sigma_{int}$, Δwrms, and Δrms, where the first is defined as the difference in Hubble residuals intrinsic scatter between the optical *BVR* data, fit using SALT2 or SNooPy, and the indicated subset of NIR data using the GP method at NIR max. The quantities Δwrms and Δrms are defined in a similar way to $\Delta\sigma_{int}$ but using wrms and rms instead of the intrinsic scatter, respectively. The uncertainties are given by the quadrature sum of the σ_{int}, wrms, or rms, uncertainties from columns 4, 6, or 7, respectively, of Tables 7 and 8 for $\sigma_{pec} = 150$ km s^{-1}. Columns 3, 5, and 7 show $n - \sigma$ defined as the number n of standard deviations σ by which the NIR data yields *smaller* σ_{int}, wrms, or rms than the optical data using these methods, respectively. Excluding the K_s-band on its own, where our LC compilation contains much less data than the *YJH* bands, in general, NIR data subsets yield smaller rms than the optical data at the $\sim$1.3–4.1σ level. In the best case, the *JH*, *YJH*, and *YJHK_s*-bands perform $\sim$2.3–4.1σ better than either SALT2 or SNooPy fits to the *BVR* data in terms of the rms, while in the worst case, *J*-band, still performs 1.3σ better than optical data. For simplicity, the stated uncertainties on the difference in dispersion estimates between any two methods ignores the fact that the actual peculiar-velocity distance errors are exactly the same between the optical and NIR samples, since they contain exactly the same SN. The effect of accounting for this correlation is to decrease the uncertainty of the difference, and increase the significance (Section 5).

4.4.1. SALT2 Distance Modulus

We use the optical photometric data compiled in the public SNANA (Kessler et al. 2009b) database[14] but replace the CMB redshift values in the SNANA photometric files with the z_{CMB} values in Table 2. Using the latest SALT2 model (SALT2.JLA-B14) (Guy et al. 2007) already trained on the JLA sample (Betoule et al. 2014), we fit the optical data and determine the SALT2 light-curve fit parameters for each SN. For the CSP data, we added an additional 0.01 mag in quadrature to the photometric errors to obtain more conservative uncertainties on those values when fitting the data in SALT2. We use the SALT2 outputs including the apparent magnitude m_B at B-band maximum light, the stretch parameter x_1, and the color term c, as well as their correlations.

We convert the SALT2-fit parameters to distance moduli for each SN using the Tripp formula (Tripp 1998),

$$\mu_s = m_{B,s} - M_B + \alpha x_{1,s} - \beta c_s, \qquad (29)$$

where M_B is the expected absolute magnitude at B-band maximum light for a SNe Ia with $x_1 = 0$, $c = 0$, while α and β are coefficients parameterizing correlations between luminosity and stretch or luminosity and color, respectively.

For the global parameters M, α, β we use the values reported by Scolnic et al. (2018); $\alpha = 0.147$, $\beta = 3.00$, and assume the fiducial values of $H_0 = 73.24$ km s^{-1} Mpc^{-1} and $M_B = -19.36$ mag. We then adjust the latter to $M_B = -19.44$ mag so that the weighted-average Hubble residual is zero.

The standard deviation of the measurement error $\sigma_{fit,s}$ from the SALT2 fitting comes from propagating the uncertainties on Equation (29), including their correlations. Interestingly we found that for the SNe with high Milky Way color excess $E(B - V) > 0.2$ the uncertainty on $m_{B,s}$ is larger than the propagated uncertainty on the SALT2 distance modulus, μ_s, derived from optical bands. This evidence further emphasizes how SNe Ia are more negatively affected by dust when deriving distances using optical data, as compared to NIR observations.

The variance of the photometric distance modulus is given by

$$\sigma_{\mu,s}^2 = \sigma_{fit,s}^2 + \sigma_{int}^2. \qquad (30)$$

Using SALT2 in this way, we obtain an intrinsic scatter in the Hubble residuals of $\sigma_{int} = 0.133 \pm 0.022$, an inverse-variance wrms of wrms = 0.174 ± 0.020 mag, and a simple rms = 0.179 ± 0.018 mag. The third column of Table 15 and the left panel of Figure 10 show the distance moduli derived from the SALT2 fits, along with the Hubble diagram and residuals, respectively. The uncertainties shown in Table 15 and Figure 10 are the values of $\sigma_{fit,s}$.

Note that we are not applying the usual SALT2 cuts to this subsample of SNe because we are interested in comparing the scatter in the Hubble residuals using exactly the same 56 SNe Ia used in the "any $YJHK_s$" Hubble diagram for the GP method. We find that when applying the SALT2 cut on color, $-0.3 < c < 0.3$, there is only one SN Ia in the subsample that does not pass this cut. All SNe Ia in the sample pass these SALT2 cuts: $-3 < x_1 < 3$, uncertainty in $x_1 < 1$, and uncertainty in $t_{B\,max} < 2$ days. However, 21 SNe Ia fail to

---
[14] http://snana.uchicago.edu. Version 2017 October 18.

Table 12
Type Ia SNe *YJHK_s* Distance Moduli from Template Method

SN Name	Source	$\hat{\mu}^{\mathrm{Y}}$ (mag)	$\hat{\mu}^{\mathrm{J}}$ (mag)	$\hat{\mu}^{\mathrm{H}}$ (mag)	$\hat{\mu}^{\mathrm{K}}$ (mag)	$\hat{\mu}$ (mag)
SN1998bu	CfA	...	30.11 ± 0.03	30.02 ± 0.02	29.97 ± 0.01	30.03 ± 0.013
SN1999ee	K04b	...	33.30 ± 0.02	33.27 ± 0.02	...	33.28 ± 0.016
SN1999ek	K04c	...	34.27 ± 0.02	34.27 ± 0.02	...	34.27 ± 0.016
SN2000bh	K04b	34.83 ± 0.07	35.00 ± 0.06	34.83 ± 0.04	...	34.81 ± 0.041
SN2000ca	K04b	...	34.87 ± 0.02	34.92 ± 0.02	...	34.91 ± 0.016
SN2000E	V03	...	31.72 ± 0.04	31.91 ± 0.04	31.78 ± 0.04	31.81 ± 0.022
SN2001ba	K04b	...	35.56 ± 0.04	35.54 ± 0.04	35.66 ± 0.04	35.58 ± 0.023
SN2001bt	K04c	...	33.94 ± 0.04	33.97 ± 0.03	33.92 ± 0.03	33.94 ± 0.021
SN2001cn	K04c	...	34.06 ± 0.06	34.00 ± 0.06	33.95 ± 0.09	34.00 ± 0.039
SN2001cz	K04c	...	33.88 ± 0.04	33.96 ± 0.06	33.96 ± 0.07	33.94 ± 0.034
SN2001el	K03	...	31.32 ± 0.03	31.27 ± 0.03	31.24 ± 0.03	31.28 ± 0.017
SN2002dj	P08	...	32.99 ± 0.03	33.00 ± 0.03	32.97 ± 0.03	32.99 ± 0.015
SN2003du	St07	...	32.64 ± 0.04	32.76 ± 0.03	32.72 ± 0.03	32.71 ± 0.020
SN2003hv	L09	...	31.38 ± 0.02	31.43 ± 0.02	31.45 ± 0.02	31.42 ± 0.011
SN2004ef	CSP	35.54 ± 0.07	35.66 ± 0.12	35.56 ± 0.10	...	35.54 ± 0.073
SN2004eo	CSP	33.91 ± 0.01	33.95 ± 0.01	33.98 ± 0.02	...	33.95 ± 0.013
SN2004ey	CSP	34.01 ± 0.02	33.95 ± 0.03	34.04 ± 0.04	...	34.04 ± 0.026
SN2004gs	CSP	35.36 ± 0.07	35.65 ± 0.10	35.57 ± 0.09	...	35.47 ± 0.068
SN2004S	K07	...	33.05 ± 0.04	33.10 ± 0.03	33.10 ± 0.05	33.08 ± 0.023
SN2005bo	CfA	...	33.77 ± 0.11	33.81 ± 0.08	33.87 ± 0.06	33.81 ± 0.050
SN2005cf	CfA	...	32.22 ± 0.02	32.21 ± 0.02	32.34 ± 0.01	32.25 ± 0.009
SN2005el	CSP	33.95 ± 0.02	34.02 ± 0.03	33.99 ± 0.03	...	33.97 ± 0.020
SN2005iq	CSP	35.69 ± 0.02	35.76 ± 0.03	35.78 ± 0.05	...	35.74 ± 0.033
SN2005kc	CSP	33.86 ± 0.02	33.88 ± 0.03	33.88 ± 0.02	...	33.87 ± 0.019
SN2005ki	CSP	34.58 ± 0.02	34.64 ± 0.03	34.65 ± 0.04	...	34.62 ± 0.029
SN2005lu	CSP	35.89 ± 0.11	...	...	...	35.89 ± 0.106
SN2005na	CfA	...	35.31 ± 0.13	...	35.48 ± 0.15	35.38 ± 0.097
SN2006ac	CfA	...	35.20 ± 0.08	35.32 ± 0.12	35.03 ± 0.09	35.20 ± 0.059
SN2006ax	CSP	34.18 ± 0.01	34.15 ± 0.02	34.23 ± 0.02	...	34.22 ± 0.014
SN2006bh	CSP	33.27 ± 0.03	33.32 ± 0.04	33.31 ± 0.03	...	33.29 ± 0.025
SN2006bt	CSP	...	35.33 ± 0.04	...	...	35.33 ± 0.039
SN2006cp	CfA	...	35.12 ± 0.11	34.90 ± 0.08	34.47 ± 0.10	34.85 ± 0.054
SN2006D	CfA	...	32.93 ± 0.03	32.94 ± 0.04	33.03 ± 0.04	32.97 ± 0.021
SN2006ej	CSP	34.42 ± 0.14	34.60 ± 0.09	...	...	34.49 ± 0.094
SN2006kf	CSP	34.65 ± 0.02	34.75 ± 0.02	34.74 ± 0.03	...	34.70 ± 0.022
SN2006lf	CfA	...	33.48 ± 0.03	33.54 ± 0.04	...	33.53 ± 0.030
SN2006N	CfA	...	34.05 ± 0.11	33.92 ± 0.09	33.74 ± 0.09	33.91 ± 0.058
SN2007A	CSP	34.30 ± 0.02	34.18 ± 0.05	34.26 ± 0.04	...	34.29 ± 0.029
SN2007af	CSP	31.91 ± 0.01	31.96 ± 0.01	31.93 ± 0.01	...	31.92 ± 0.009
SN2007ai	CSP	35.57 ± 0.02	35.42 ± 0.03	35.38 ± 0.03	...	35.46 ± 0.022
SN2007as	CSP	34.26 ± 0.02	34.27 ± 0.02	34.34 ± 0.04	...	34.31 ± 0.025
SN2007bc	CSP	34.68 ± 0.03	34.80 ± 0.04	34.82 ± 0.06	...	34.76 ± 0.042
SN2007bd	CSP	35.54 ± 0.03	35.58 ± 0.04	35.60 ± 0.08	...	35.57 ± 0.057
SN2007ca	CSP	34.17 ± 0.01	34.07 ± 0.01	34.01 ± 0.02	...	34.07 ± 0.016
SN2007co	CfA	...	...	...	34.99 ± 0.11	34.99 ± 0.110
SN2007cq	CfA	...	34.87 ± 0.03	34.84 ± 0.08	...	34.85 ± 0.060
SN2007jg	CSP	36.05 ± 0.02	36.16 ± 0.02	...	...	36.09 ± 0.014
SN2007le	CSP	32.36 ± 0.01	32.24 ± 0.01	32.24 ± 0.01	...	32.29 ± 0.007
SN2007qe	CfA	...	34.70 ± 0.17	34.91 ± 0.07	35.26 ± 0.15	34.95 ± 0.075
SN2007sr	CSP	31.68 ± 0.05	31.67 ± 0.06	31.68 ± 0.03	...	31.68 ± 0.029
SN2007st	CSP	...	34.22 ± 0.09	34.55 ± 0.04	...	34.46 ± 0.041
SN2008af	CfA	...	35.98 ± 0.19	35.90 ± 0.24	35.96 ± 0.18	35.94 ± 0.124
SN2008ar	CSP	35.30 ± 0.02	35.30 ± 0.04	35.17 ± 0.06	...	35.22 ± 0.038
SN2008bc	CSP	34.07 ± 0.02	34.02 ± 0.04	33.95 ± 0.04	...	34.00 ± 0.029
SN2008bf	CSP	34.96 ± 0.01	34.95 ± 0.01	35.07 ± 0.06	...	35.03 ± 0.042
SN2008C	CSP	34.27 ± 0.08	34.24 ± 0.09	34.31 ± 0.06	...	34.30 ± 0.053
SN2008fl	CSP	34.42 ± 0.03	34.52 ± 0.05	34.55 ± 0.03	...	34.49 ± 0.024
SN2008fr	CSP	36.11 ± 0.06	36.23 ± 0.14	...	...	36.16 ± 0.067
SN2008fw	CSP	33.07 ± 0.11	33.06 ± 0.14	32.94 ± 0.12	...	32.98 ± 0.091
SN2008gb	CfA	...	35.98 ± 0.08	35.78 ± 0.09	35.83 ± 0.11	35.86 ± 0.053
SN2008gg	CSP	35.63 ± 0.05	35.60 ± 0.10	35.63 ± 0.07	...	35.63 ± 0.051
SN2008gl	CSP	35.97 ± 0.02	35.70 ± 0.03	35.72 ± 0.05	...	35.83 ± 0.033
SN2008gp	CSP	35.55 ± 0.02	35.50 ± 0.03	35.69 ± 0.06	...	35.65 ± 0.038

Table 12
(Continued)

SN Name	Source	$\hat{\mu}^{\mathrm{Y}}$ (mag)	$\hat{\mu}^{\mathrm{J}}$ (mag)	$\hat{\mu}^{\mathrm{H}}$ (mag)	$\hat{\mu}^{\mathrm{K}}$ (mag)	$\hat{\mu}$ (mag)
SN2008hj	CSP	36.03 ± 0.05	36.02 ± 0.07	35.91 ± 0.07	...	35.95 ± 0.049
SN2008hm	CfA	...	34.59 ± 0.02	34.76 ± 0.06	34.57 ± 0.04	34.65 ± 0.027
SN2008hs	CfA	...	34.86 ± 0.06	34.90 ± 0.06	34.82 ± 0.07	34.86 ± 0.035
SN2008hv	CSP	33.80 ± 0.02	33.78 ± 0.02	33.81 ± 0.04	...	33.81 ± 0.026
SN2008ia	CSP	34.80 ± 0.02	34.72 ± 0.03	34.66 ± 0.03	...	34.72 ± 0.022
SN2009aa	CSP	35.23 ± 0.03	35.27 ± 0.04	35.25 ± 0.03	...	35.24 ± 0.026
SN2009ab	CSP	33.46 ± 0.02	33.51 ± 0.03	33.56 ± 0.03	...	33.52 ± 0.023
SN2009ad	CSP	35.24 ± 0.01	35.21 ± 0.02	35.33 ± 0.04	...	35.30 ± 0.025
SN2009ag	CSP	33.06 ± 0.00	33.11 ± 0.01	33.08 ± 0.01	...	33.07 ± 0.005
SN2009al	CfA	...	34.92 ± 0.05	34.84 ± 0.03	...	34.87 ± 0.028
SN2009an	CfA	...	33.46 ± 0.03	33.40 ± 0.03	33.51 ± 0.04	33.45 ± 0.017
SN2009bv	CfA	...	36.03 ± 0.05	35.82 ± 0.05	...	35.88 ± 0.040
SN2009cz	CSP	34.69 ± 0.05	34.68 ± 0.06	34.73 ± 0.04	...	34.71 ± 0.037
SN2009D	CSP	34.90 ± 0.02	34.90 ± 0.01	34.90 ± 0.02	...	34.90 ± 0.014
SN2009kk	CfA	...	33.92 ± 0.05	34.04 ± 0.07	...	34.01 ± 0.051
SN2009kq	CfA	...	33.53 ± 0.09	33.65 ± 0.09	33.52 ± 0.06	33.57 ± 0.048
SN2009Y	CSP	32.97 ± 0.01	32.96 ± 0.02	32.97 ± 0.01	...	32.97 ± 0.011
SN2010ai	CfA	...	35.04 ± 0.03	34.87 ± 0.06	...	34.92 ± 0.047
SN2010dw	CfA	...	36.12 ± 0.04	...	...	36.12 ± 0.045
SN2010iw	CfA	...	34.70 ± 0.04	34.63 ± 0.06	34.73 ± 0.10	34.68 ± 0.039
SN2010kg	CfA	...	34.24 ± 0.04	34.14 ± 0.04	34.40 ± 0.11	34.25 ± 0.037
SN2011ao	CfA	...	33.35 ± 0.03	33.29 ± 0.03	33.22 ± 0.06	33.29 ± 0.023
SN2011B	CfA	...	31.62 ± 0.07	31.68 ± 0.05	...	31.66 ± 0.038
SN2011by	CfA	...	31.76 ± 0.06	31.74 ± 0.04	...	31.75 ± 0.032
SN2011df	CfA	...	33.97 ± 0.01	33.90 ± 0.03	33.83 ± 0.12	33.90 ± 0.037
SNf20080514-002	CfA	...	35.03 ± 0.04	34.97 ± 0.07	35.23 ± 0.05	35.07 ± 0.032

Note. Distance moduli and their fitting uncertainties $\hat{\sigma}_{\mathrm{fit},s}$, estimated from the different NIR bands, either alone (see columns 3–6) or combined (column 7), using the template method. Corresponding Hubble diagrams are shown in Figures 6 and 12. Reference codes for the data Source are the same as in Table 2.

pass the SALT2 cut requiring that the probability that the data are represented by the model, given the χ^2 per degree of freedom of the fit, is larger than 0.001 (a.k.a, FIT-PROB > 0.001). However, a low fit probability does not necessarily indicate a poor SNe Ia light-curve fit and may instead be an indication that the photometric uncertainties or the model uncertainties are unrealistically small. We visually inspected the light-curve fits of these 21 SNe Ia, finding that they are reasonably well-fit by the model and can therefore be used to yield accurate distance measurements.

4.4.2. SNooPy Distance Modulus

As a second cross check of the scatter in the optical-only Hubble diagram, we also fit the *BVR*-bands LCs using the `EBV_model` of SNooPy LC fitting package (Burns et al. 2011), where every observed apparent magnitude m_s in band $O \equiv B$, V, R is compared to the model

$$m_s(t) = \mu_s + T_Q(t, \Delta m_{15,s}) + M_Q(\Delta m_{15,s})$$
$$+ R_O E(B-V)_{\mathrm{MW},s} + R_Q E(B-V)_{\mathrm{host},s}$$
$$+ K^s_{OQ}(z_s, t, E(B-V)_{\mathrm{MW},s}, E(B-V)_{\mathrm{host},s}), \quad (31)$$

where $T_Q(t, \Delta m_{15,s})$ is a light-curve template for the rest-frame band Q that depends on t and $\Delta m_{15,s}$, and $M_{Q,s}(\Delta m_{15,s})$ is the absolute magnitude band Q. In this model, the free parameters that SNooPy estimates (along with their uncertainties) are μ_s, $\Delta m_{15,s}$, $E(B-V)_{\mathrm{host},s}$ and $t_{B\,\mathrm{max}}$. We consider the estimated uncertainty on μ_s output by SNooPy as the $\sigma_{\mathrm{fit},s}$ in our analysis.

We refer the reader to Burns et al. (2011) for details on how SNooPy estimates the uncertainty on μ_s.

We obtain an intrinsic scatter in the Hubble residuals of $\sigma_{\mathrm{int}} = 0.128 \pm 0.018$, a wrms $= 0.159 \pm 0.019$ mag, and an rms $= 0.174 \pm 0.021$ mag. The fourth column of Table 15 and right panel of Figure 10 show the distance moduli derived from the SNooPy fits, along with the Hubble diagram and residuals, respectively. In Figure 11, we compare the scatter between NIR and optical Hubble residuals, by plotting the histograms and the cumulative distribution functions for Hubble residuals using the same supernovae (see Section 5).

5. Discussion

Tables 7 and 8 summarize the scatter in the Hubble residuals measured with the either the intrinsic scatter σ_{int}, the wrms, or the rms. We compute these for both our fiducial peculiar-velocity uncertainty of $\sigma_{\mathrm{pec}} = 150\,\mathrm{km\,s}^{-1}$ as well as the value $\sigma_{\mathrm{pec}} = 250\,\mathrm{km\,s}^{-1}$ used in Scolnic et al. (2018). Figures 12–14, show the Hubble diagrams (top panels) and Hubble residuals plots (bottom panels) for the individual NIR bands when using the three methods developed in this work to derive distances: template and GP at the times of *NIR* and *B* max, respectively.

While the formula for rms in Equation (54) does not depend on the assumed value of σ_{pec} (see Appendix C), the value of σ_{int} is relatively sensitive to the assumed value of σ_{pec}. In particular, larger assumed values of σ_{pec} yield smaller inferred values of σ_{int} (see columns 4 and 5 of Tables 7 and 8). The assumption of $\sigma_{\mathrm{pec}} = 150\,\mathrm{km\,s}^{-1}$ in this work therefore yields a more conservative estimate of σ_{int} compared with larger values of σ_{pec} because in the latter case, most of the scatter in the Hubble
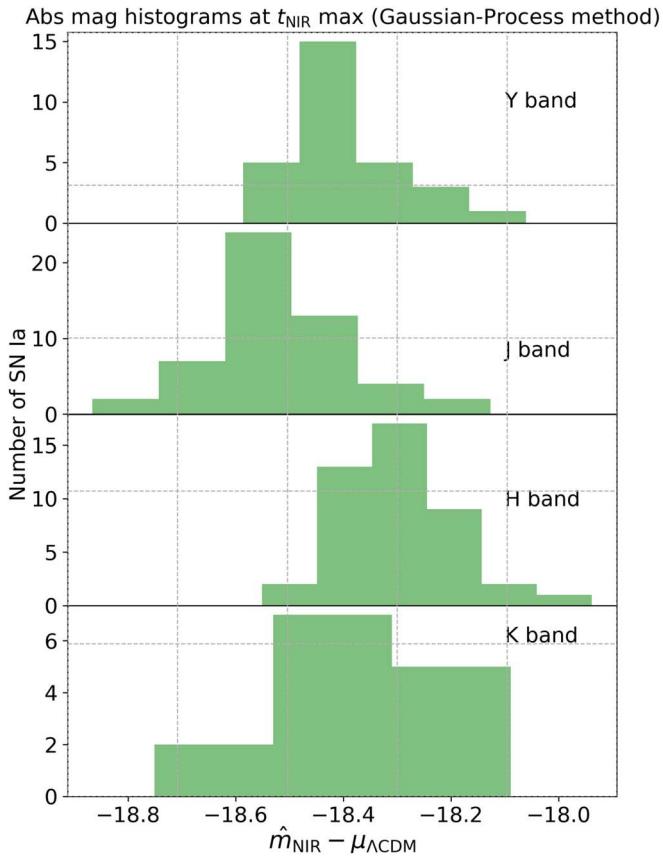
Figure 4. Histograms of the absolute magnitudes at phase $=\mathrm{NIR}_{\max}$, defined as $M_{\mathrm{NIR}_{\max},s} \equiv \hat{m}_{\mathrm{NIR}\max,s} - \mu_{\Lambda\mathrm{CDM}}(z_s)$ for the SNe Ia sample in the GP method at NIR max. The sample mean, standard deviation, and the number of SNe in each histogram are shown in Table 6.

Figure 5. Histograms of the absolute magnitudes at phase $=B_{\max}$, defined as $M_{B_{\max},s} \equiv \hat{m}_{B\max,s} - \mu_{\Lambda\mathrm{CDM}}(z_s)$ for the SNe Ia sample in the GP method at B max. The sample mean, standard deviation, and the number of SNe in each histogram are shown in Table 6.

residuals can be explained as arising solely from peculiar velocities. For instance, the Hubble residuals using only H-band LCs from the GP (NIR max) method produce an intrinsic scatter of zero when assuming $\sigma_{\mathrm{pec}} = 250\,\mathrm{km\,s^{-1}}$. We found that wrms is less sensitive than σ_{int} to the assumed value of σ_{pec}, producing differences of ~ 0.001 mag between $\sigma_{\mathrm{pec}} = 150$ and $\sigma_{\mathrm{pec}} = 250\,\mathrm{km\,s^{-1}}$.

Of the three NIR methods used to derive distance moduli, the GP method at NIR max yields smaller rms, wrms, and intrinsic scatter in the Hubble residuals than the template and GP methods at B max applied to the same 56 SNe Ia with data from any of the $YJHK_s$ bands. When we combine the GP distance moduli for these same SNe Ia referenced to the NIR maxima, we find an rms $= 0.117 \pm 0.014$, wrms $= 0.100 \pm 0.013$, and intrinsic scatter of $\sigma_{\mathrm{int}} = 0.047 \pm 0.018$ mag. Using the GP method instead referenced to B-max for the same SNe Ia yields rms $= 0.115 \pm 0.011$, wrms $= 0.106 \pm 0.010$, and $\sigma_{\mathrm{int}} = 0.066 \pm 0.016$ mag. The NIR maxima and B-max thus yield comparable dispersion in the Hubble residuals for each individual NIR band subset with the GP method (see Table 11).

By comparison, when using the NIR template method referenced to B-max for these same SNe Ia, we find a larger value of rms $= 0.138 \pm 0.014$, wrms $= 0.140 \pm 0.016$, and $\sigma_{\mathrm{int}} = 0.112 \pm 0.016$ mag.

When we create the Hubble diagram using optical-only LCs of the same 56 SNe, we find rms $= 0.179 \pm 0.018$, wrms $= 0.174 \pm 0.020$, and $\sigma_{\mathrm{int}} = 0.133 \pm 0.022$ mag when using SALT2, and rms $= 0.174 \pm 0.021$, wrms $= 0.159 \pm 0.019$, and $\sigma_{\mathrm{int}} = 0.128 \pm 0.018$ mag with SNooPy.

It is also of interest to compare the results for different observed subsamples. First, note that only the CSP observed with a Y-band filter, so it is not possible to compare these observations to other Y-band samples. Similarly, there are relatively few CSP K-band observations compared to the CfA and Others in the literature, so such K-band comparisons are not particularly useful. However, there are sufficient J- and H-band observations to perform useful comparisons by subsample, which we present in Table 9.

As seen in Table 9, for each Hubble diagram method (Template, NIR max, B max), the CSP JH data yield smaller values than the data from the CfA or Others in the literature for the various measures of dispersion, including intrinsic scatter, wrms, and rms. In most cases the CfA sample yields smaller dispersions than the Others sample. The uncertainties on the dispersions are smaller for the CSP versus CfA samples because the photometric uncertainties for the CSP data are typically at least two to three times smaller at the brightest light-curve point than the CfA data (Friedman et al. 2015). In addition, the smaller number of CfA versus CSP light curves that passed our data analysis cuts leads to a larger inferred uncertainty on the dispersions for the CfA sample. However, for all of our Hubble-diagram-creation methods listed in Table 9, for each of the J and H bands, the dispersions are still consistent with one another to within 1–2σ for the samples from the CSP, CfA, and Others. This yields evidence that, for each method, estimates of the dispersion from each data sample are consistent with being drawn from the same intrinsic population of SNe Ia.
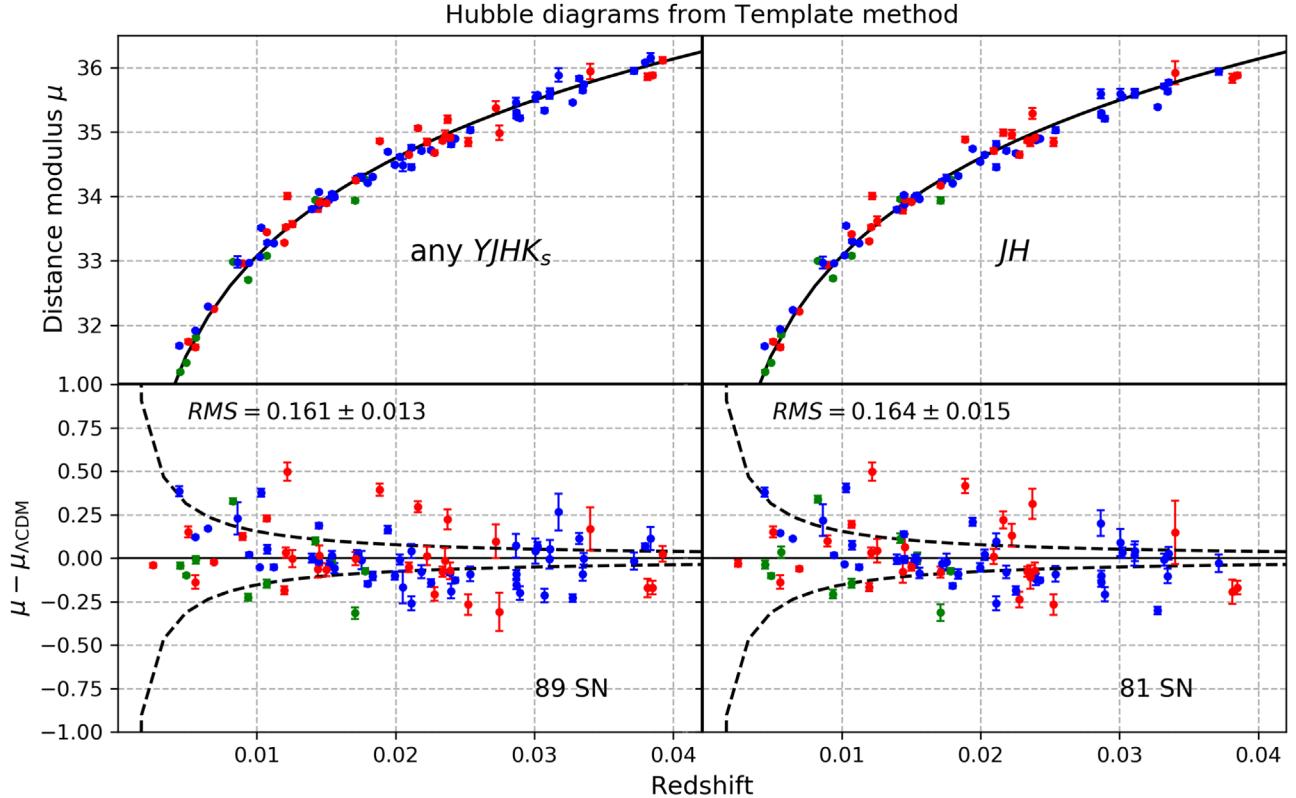
Figure 6. $YJHK_s$ Hubble diagrams (top row) and residuals (bottom row) using the template method on the 89 SNe that passed our cuts. The error bars plotted for each SN correspond to the fitting uncertainties $\hat{\sigma}_{fit,s}$. The left panel corresponds to the case when we determine a single distance modulus by combining any of the available 1, 2, 3, or 4 $YJHK_s$ distance moduli for a given SNe Ia. The right panel shows the case when we require only SNe Ia with J- and H-band data, which allows us to include the majority of data from the CfA and CSP samples. Points are color coded by NIR photometric data source, including the CfA (red; Wood-Vasey et al. 2008; Friedman et al. 2015), the CSP (blue; Krisciunas et al. 2017), and other data from the literature (green; see Table 2 and references therein). Note that only the CSP used a Y-band filter. Table 8 summarizes the intrinsic scatter in the Hubble diagrams, while Table 12 reports the numerical values of the distance moduli from this figure.

Overall, as shown in Table 10, depending on the NIR $YJHK_s$ subset, the NIR-only GP method yields an rms in the Hubble residuals that is as much as $\sim$2.3–4.1σ *smaller* than the SALT2 and SNooPy fits using optical-only BVR data. Furthermore, our "any $YJHK_s$" set of 56 SNe Ia yields an rms for our GP method at NIR max that is 0.057 ± 0.025 mag smaller than SNooPy and 0.062 ± 0.023 mag smaller that SALT2 applied to the corresponding BVR data, again at the $\sim$2.7σ level. We interpret the smaller intrinsic scatter as additional evidence, at the $\sim$2.5–3.1σ level, that NIR SNe Ia LCs at NIR maximum, without LC shape or dust corrections, are already *better* standard candles than optical-only SNe Ia LCs referenced to B-max that apply such corrections. In addition, it is possible that NIR data or a combination of NIR and optical could yield even smaller intrinsic scatter if employing a method that applies LC shape and dust corrections, for example, using a hierarchical Bayesian approach like BAYESN (Mandel et al. 2009, 2011).

In Table 10, we note that the uncertainty on the difference in the dispersion estimates between any two methods has been computed conservatively. The uncertainty of the dispersion of each individual method has been computed independently, and then the uncertainty in the difference is found by adding in quadrature, assuming the independence of the samples and therefore the individual uncertainties. However, this ignores the fact that the SNe in our optical sample are exactly the same ones as those in our NIR sample. Therefore, the actual peculiar-velocity distance errors must be the same in each sample (and not just the variance of these errors). Because of this common component of scatter, the dispersion estimate for the optical Hubble diagram is

positively correlated with that for the NIR Hubble diagram in each comparison. The effect of this positive correlation is to reduce the variance in the differences in dispersion. Using our estimates of σ_{int}, $\sigma_{fit,s}$, and $\sigma_{\mu_{pec},s}$ for the sample and each method, we ran simulations to account for this correlation and quantify this effect. For example, we find that the uncertainty in Δrms for "SNooPy– any $YJHK_s$" is $\sim$30% smaller than naive uncertainty assuming independent samples, resulting in a significance greater than 3σ.

For the Hubble diagrams created using just one of the $YJHK_s$ bands, when using the GP method at NIR max, the Y band has the smallest scatter with an rms of 0.111 ± 0.018 mag. When using the template method, the Y band has also the smallest scatter with rms $= 0.152 \pm 0.016$.

For every individual band and subset of NIR bands shown in Table 11, the GP method yields *smaller* intrinsic scatter when referencing to NIR max instead of B max, by mean amounts of up to $\sim$0.03 mag for the same SNe Ia at up to the $\sim$1.0 σ level. While not as statistically significant as the NIR versus optical comparison in Table 10, we note that the NIR maxima yield smaller intrinsic scatter σ_{int} and wrms than B max *for all subsets* of the NIR data except for K_s.[15] While NIR data at NIR max are *better* standard candles in comparison to optical data, they are also *at least as good as or better* than when referenced to B-max. Therefore, future analyses should consider using t_{NIRmax} as the reference time instead of the traditional $t_{B\,max,s}$.

---

[15] The only exception we tested is the K_s-band, which has only 14 SNe Ia LCs, where we find an essentially equivalent wrms $\sim$ 0.163 mag when referenced to either NIR max or B-max.

Table 13
SNe Ia *YJHKs* Distance Moduli from Gaussian-Process Method at NIR Max

SN Name	Source	$\hat{\mu}^{\mathrm{Y}}$ (mag)	$\hat{\mu}^{\mathrm{J}}$ (mag)	$\hat{\mu}^{\mathrm{H}}$ (mag)	$\hat{\mu}^{\mathrm{K}}$ (mag)	$\hat{\mu}$ (mag)
SN1998bu	CfA	...	30.09 ± 0.03	30.03 ± 0.03	29.87 ± 0.02	29.99 ± 0.018
SN1999ee	K04b	...	33.30 ± 0.02	33.32 ± 0.02	...	33.32 ± 0.016
SN1999ek	K04c	...	34.24 ± 0.02	34.28 ± 0.02	...	34.27 ± 0.014
SN2000ca	K04b	...	34.94 ± 0.03	...	...	34.94 ± 0.034
SN2000E	V03	...	31.72 ± 0.02	31.93 ± 0.03	31.71 ± 0.04	31.84 ± 0.022
SN2001ba	K04b	...	35.55 ± 0.02	35.55 ± 0.03	35.56 ± 0.08	35.55 ± 0.031
SN2001bt	K04c	...	33.91 ± 0.03	33.96 ± 0.02	33.83 ± 0.03	33.91 ± 0.014
SN2001cz	K04c	...	33.90 ± 0.05	34.03 ± 0.11	33.87 ± 0.11	33.97 ± 0.072
SN2001el	K03	...	31.45 ± 0.02	31.34 ± 0.03	31.17 ± 0.04	31.30 ± 0.022
SN2002dj	P08	...	33.01 ± 0.03	33.03 ± 0.02	32.89 ± 0.03	32.98 ± 0.017
SN2004eo	CSP	33.97 ± 0.01	33.97 ± 0.01	33.97 ± 0.01	...	33.97 ± 0.011
SN2004ey	CSP	34.03 ± 0.01	33.96 ± 0.01	34.06 ± 0.04	...	34.08 ± 0.038
SN2005cf	CfA	...	32.21 ± 0.06	32.17 ± 0.03	32.25 ± 0.03	32.20 ± 0.020
SN2005el	CSP	33.88 ± 0.01	33.95 ± 0.01	33.97 ± 0.01	...	33.96 ± 0.013
SN2005iq	CSP	35.76 ± 0.03	35.75 ± 0.04	35.74 ± 0.07	...	35.74 ± 0.069
SN2005kc	CSP	33.92 ± 0.01	33.90 ± 0.01	33.89 ± 0.02	...	33.90 ± 0.015
SN2005ki	CSP	34.58 ± 0.01	34.59 ± 0.01	34.55 ± 0.03	...	34.55 ± 0.027
SN2006ax	CSP	34.17 ± 0.01	34.16 ± 0.01	34.22 ± 0.02	...	34.22 ± 0.019
SN2006bh	CSP	33.31 ± 0.01	33.30 ± 0.01	33.31 ± 0.01	...	33.31 ± 0.012
SN2006bt	CSP	...	35.51 ± 0.04	...	...	35.51 ± 0.041
SN2006D	CfA	...	32.85 ± 0.02	32.92 ± 0.04	32.86 ± 0.06	32.90 ± 0.029
SN2006kf	CSP	34.73 ± 0.01	34.77 ± 0.01	34.75 ± 0.04	...	34.74 ± 0.039
SN2006lf	CfA	...	33.40 ± 0.03	33.42 ± 0.05	...	33.42 ± 0.043
SN2007A	CSP	34.26 ± 0.01	34.17 ± 0.02	...	...	34.27 ± 0.012
SN2007af	CSP	31.92 ± 0.01	32.00 ± 0.00	31.92 ± 0.01	...	31.90 ± 0.007
SN2007ai	CSP	35.67 ± 0.02	...	...	...	35.67 ± 0.025
SN2007as	CSP	...	...	34.37 ± 0.04	...	34.37 ± 0.044
SN2007bc	CSP	...	34.84 ± 0.02	...	...	34.84 ± 0.019
SN2007bd	CSP	35.54 ± 0.02	35.56 ± 0.04	...	...	35.54 ± 0.023
SN2007ca	CSP	...	...	34.01 ± 0.03	...	34.01 ± 0.025
SN2007jg	CSP	36.09 ± 0.02	36.11 ± 0.02	...	...	36.09 ± 0.021
SN2007le	CSP	32.33 ± 0.01	32.23 ± 0.01	32.26 ± 0.01	...	32.28 ± 0.006
SN2008ar	CSP	35.33 ± 0.01	35.34 ± 0.03	35.28 ± 0.05	...	35.28 ± 0.054
SN2008bc	CSP	34.02 ± 0.01	33.98 ± 0.02	34.01 ± 0.03	...	34.02 ± 0.031
SN2008bf	CSP	34.98 ± 0.01	34.87 ± 0.01	...	...	34.98 ± 0.010
SN2008gb	CfA	...	...	...	36.31 ± 0.21	36.31 ± 0.211
SN2008gp	CSP	35.63 ± 0.03	35.53 ± 0.05	35.75 ± 0.07	...	35.76 ± 0.074
SN2008hj	CSP	35.98 ± 0.02	36.08 ± 0.04	...	...	35.97 ± 0.026
SN2008hs	CfA	...	34.86 ± 0.05	...	34.67 ± 0.11	34.77 ± 0.059
SN2008hv	CSP	33.77 ± 0.00	33.72 ± 0.01	33.72 ± 0.02	...	33.73 ± 0.022
SN2009aa	CSP	35.31 ± 0.01	35.28 ± 0.01	35.28 ± 0.02	...	35.28 ± 0.018
SN2009ad	CSP	35.27 ± 0.01	35.27 ± 0.02	35.37 ± 0.05	...	35.37 ± 0.048
SN2009ag	CSP	33.20 ± 0.01	33.20 ± 0.01	33.12 ± 0.01	...	33.12 ± 0.009
SN2009al	CfA	...	35.07 ± 0.02	34.88 ± 0.03	...	34.91 ± 0.029
SN2009an	CfA	...	33.40 ± 0.02	33.42 ± 0.03	33.39 ± 0.03	33.41 ± 0.019
SN2009bv	CfA	...	36.07 ± 0.04	36.01 ± 0.13	...	36.02 ± 0.108
SN2009cz	CSP	34.77 ± 0.01	34.72 ± 0.02	34.77 ± 0.04	...	34.78 ± 0.038
SN2009D	CSP	34.98 ± 0.01	34.91 ± 0.01	34.95 ± 0.02	...	34.97 ± 0.018
SN2009Y	CSP	33.02 ± 0.01	32.98 ± 0.01	32.97 ± 0.02	...	32.98 ± 0.018
SN2010ai	CfA	...	35.05 ± 0.05	34.99 ± 0.10	34.85 ± 0.09	34.95 ± 0.063
SN2010kg	CfA	...	34.22 ± 0.03	34.16 ± 0.03	34.33 ± 0.14	34.22 ± 0.047
SN2011ao	CfA	...	33.33 ± 0.05	33.23 ± 0.03	...	33.24 ± 0.023
SN2011B	CfA	...	31.66 ± 0.16	...	...	31.66 ± 0.156
SN2011by	CfA	...	31.71 ± 0.05	31.68 ± 0.03	...	31.69 ± 0.026
SN2011df	CfA	...	33.94 ± 0.03	33.89 ± 0.05	...	33.90 ± 0.041
SNf20080514-002	CfA	...	35.03 ± 0.14	34.92 ± 0.12	...	34.94 ± 0.101

Note. Distance moduli and their fitting uncertainties $\hat{\sigma}_{\mathrm{fit},s}$, estimated from the different NIR bands, either alone (see columns 3–6) or combined (column 7) using the GP method at NIR max. The Hubble diagrams from these data are shown in Figures 7 and 13. Reference codes for the data Source are the same as in Table 2.

As an additional comparison between NIR and optical Hubble residuals, in Figure 11, we plot the histograms (dashed lines) with their Gaussian approximation (left panel), and the cumulative distribution function (right panel) for Hubble residuals using the same 56 SNe Ia used for the "any *YJHKs*" GP method at NIR max (lower left panel on Figure 7), SALT2 (lower left panel of

Table 14
SNe Ia *YJHK*$_s$ Distance Moduli from Gaussian-process Method at *B* Max

SN Name	Source	$\hat{\mu}^{\mathrm{Y}}$ (mag)	$\hat{\mu}^{\mathrm{J}}$ (mag)	$\hat{\mu}^{\mathrm{H}}$ (mag)	$\hat{\mu}^{\mathrm{K}}$ (mag)	$\hat{\mu}$ (mag)
SN1998bu	CfA	...	30.11 ± 0.02	30.04 ± 0.02	29.90 ± 0.02	29.98 ± 0.014
SN1999ee	K04b	...	33.31 ± 0.02	33.28 ± 0.02	...	33.29 ± 0.013
SN1999ek	K04c	...	34.26 ± 0.02	34.31 ± 0.02	...	34.30 ± 0.013
SN2000ca	K04b	...	34.86 ± 0.02	...	...	34.86 ± 0.019
SN2000E	V03	...	31.77 ± 0.04	31.96 ± 0.05	31.68 ± 0.06	31.85 ± 0.041
SN2001ba	K04b	...	35.43 ± 0.09	35.54 ± 0.07	35.47 ± 0.09	35.51 ± 0.055
SN2001bt	K04c	...	33.86 ± 0.06	34.02 ± 0.05	33.81 ± 0.06	33.94 ± 0.039
SN2001cz	K04c	...	33.81 ± 0.05	34.01 ± 0.07	33.90 ± 0.08	33.97 ± 0.058
SN2001el	K03	...	31.36 ± 0.02	31.30 ± 0.03	31.20 ± 0.04	31.25 ± 0.023
SN2002dj	P08	...	32.97 ± 0.02	33.00 ± 0.02	32.87 ± 0.03	32.95 ± 0.018
SN2004eo	CSP	33.96 ± 0.01	33.94 ± 0.01	33.99 ± 0.01	...	33.98 ± 0.009
SN2004ey	CSP	34.06 ± 0.02	33.92 ± 0.02	34.07 ± 0.04	...	34.08 ± 0.027
SN2005cf	CfA	...	32.23 ± 0.01	32.22 ± 0.01	32.28 ± 0.01	32.24 ± 0.009
SN2005el	CSP	33.96 ± 0.01	33.97 ± 0.02	34.01 ± 0.02	...	33.99 ± 0.017
SN2005iq	CSP	35.70 ± 0.02	35.76 ± 0.03	35.80 ± 0.06	...	35.76 ± 0.042
SN2005kc	CSP	33.90 ± 0.01	33.88 ± 0.02	33.89 ± 0.02	...	33.90 ± 0.013
SN2005ki	CSP	34.59 ± 0.02	34.61 ± 0.03	34.58 ± 0.03	...	34.58 ± 0.022
SN2006ax	CSP	34.20 ± 0.01	34.13 ± 0.01	34.21 ± 0.01	...	34.21 ± 0.010
SN2006bh	CSP	33.28 ± 0.03	33.34 ± 0.09	33.31 ± 0.05	...	33.30 ± 0.037
SN2006bt	CSP	...	35.43 ± 0.04	...	...	35.43 ± 0.041
SN2006D	CfA	...	32.89 ± 0.03	32.91 ± 0.05	32.94 ± 0.05	32.92 ± 0.035
SN2006kf	CSP	34.68 ± 0.01	34.73 ± 0.01	34.76 ± 0.03	...	34.73 ± 0.022
SN2006lf	CfA	...	33.45 ± 0.03	33.57 ± 0.05	...	33.54 ± 0.038
SN2007A	CSP	34.34 ± 0.01	34.19 ± 0.04	...	...	34.30 ± 0.015
SN2007af	CSP	31.95 ± 0.01	31.96 ± 0.01	31.96 ± 0.01	...	31.95 ± 0.007
SN2007ai	CSP	35.57 ± 0.03	...	...	...	35.57 ± 0.027
SN2007as	CSP	...	...	34.30 ± 0.04	...	34.30 ± 0.036
SN2007bc	CSP	...	34.75 ± 0.04	...	...	34.75 ± 0.037
SN2007bd	CSP	35.56 ± 0.02	35.60 ± 0.04	...	...	35.57 ± 0.020
SN2007ca	CSP	...	...	34.02 ± 0.02	...	34.02 ± 0.021
SN2007jg	CSP	36.08 ± 0.02	36.24 ± 0.03	...	...	36.12 ± 0.018
SN2007le	CSP	32.41 ± 0.01	32.24 ± 0.01	32.26 ± 0.01	...	32.32 ± 0.005
SN2008ar	CSP	35.37 ± 0.03	35.41 ± 0.05	35.34 ± 0.08	...	35.35 ± 0.053
SN2008bc	CSP	34.14 ± 0.02	34.08 ± 0.03	33.93 ± 0.03	...	34.00 ± 0.023
SN2008bf	CSP	35.01 ± 0.02	34.98 ± 0.02	...	...	35.00 ± 0.012
SN2008gb	CfA	...	...	...	36.28 ± 0.20	36.28 ± 0.200
SN2008gp	CSP	35.59 ± 0.01	35.50 ± 0.03	35.67 ± 0.06	...	35.65 ± 0.044
SN2008hj	CSP	35.99 ± 0.05	36.05 ± 0.10	...	...	36.01 ± 0.044
SN2008hs	CfA	...	34.96 ± 0.09	...	34.60 ± 0.13	34.64 ± 0.115
SN2008hv	CSP	33.88 ± 0.01	33.83 ± 0.02	33.72 ± 0.03	...	33.78 ± 0.022
SN2009aa	CSP	35.22 ± 0.02	35.18 ± 0.03	35.22 ± 0.03	...	35.23 ± 0.023
SN2009ad	CSP	35.28 ± 0.01	35.24 ± 0.02	35.35 ± 0.04	...	35.33 ± 0.027
SN2009ag	CSP	33.11 ± 0.00	33.12 ± 0.00	33.09 ± 0.00	...	33.10 ± 0.003
SN2009al	CfA	...	35.02 ± 0.04	34.86 ± 0.04	...	34.90 ± 0.033
SN2009an	CfA	...	33.48 ± 0.02	33.37 ± 0.03	33.49 ± 0.05	33.42 ± 0.026
SN2009bv	CfA	...	35.94 ± 0.08	36.03 ± 0.07	...	36.01 ± 0.058
SN2009cz	CSP	34.72 ± 0.08	34.77 ± 0.12	34.72 ± 0.06	...	34.71 ± 0.054
SN2009D	CSP	34.96 ± 0.02	34.90 ± 0.01	34.90 ± 0.02	...	34.92 ± 0.015
SN2009Y	CSP	33.01 ± 0.01	32.91 ± 0.02	32.98 ± 0.01	...	32.99 ± 0.011
SN2010ai	CfA	...	35.02 ± 0.03	34.91 ± 0.09	34.89 ± 0.08	34.89 ± 0.065
SN2010kg	CfA	...	34.42 ± 0.08	34.13 ± 0.08	34.26 ± 0.25	34.17 ± 0.113
SN2011ao	CfA	...	33.35 ± 0.03	33.30 ± 0.03	...	33.31 ± 0.022
SN2011B	CfA	...	31.78 ± 0.43	...	...	31.78 ± 0.434
SN2011by	CfA	...	31.67 ± 0.06	31.64 ± 0.04	...	31.65 ± 0.034
SN2011df	CfA	...	33.99 ± 0.01	33.93 ± 0.03	...	33.94 ± 0.022
SNf20080514-002	CfA	...	35.03 ± 0.04	34.99 ± 0.07	...	35.00 ± 0.054

Note. Same as Table 13 but using the GP method at *B* max. The Hubble diagrams from these data are shown in Figures 8 and 14. Reference codes for the data Source are the same as in Table 2.

Figure 10), and SNooPy (lower right panel of Figure 10). The Gaussian approximations of the histograms in the left panel of Figure 11 show that the Hubble residuals are more narrowly

distributed for the NIR data (solid red curve) compared to both optical methods (solid green and blue), while in the right panel of Figure 11 the cumulative distribution function curve for the NIR

Hubble diagrams from Gaussian-Process method at t_{NIR} max
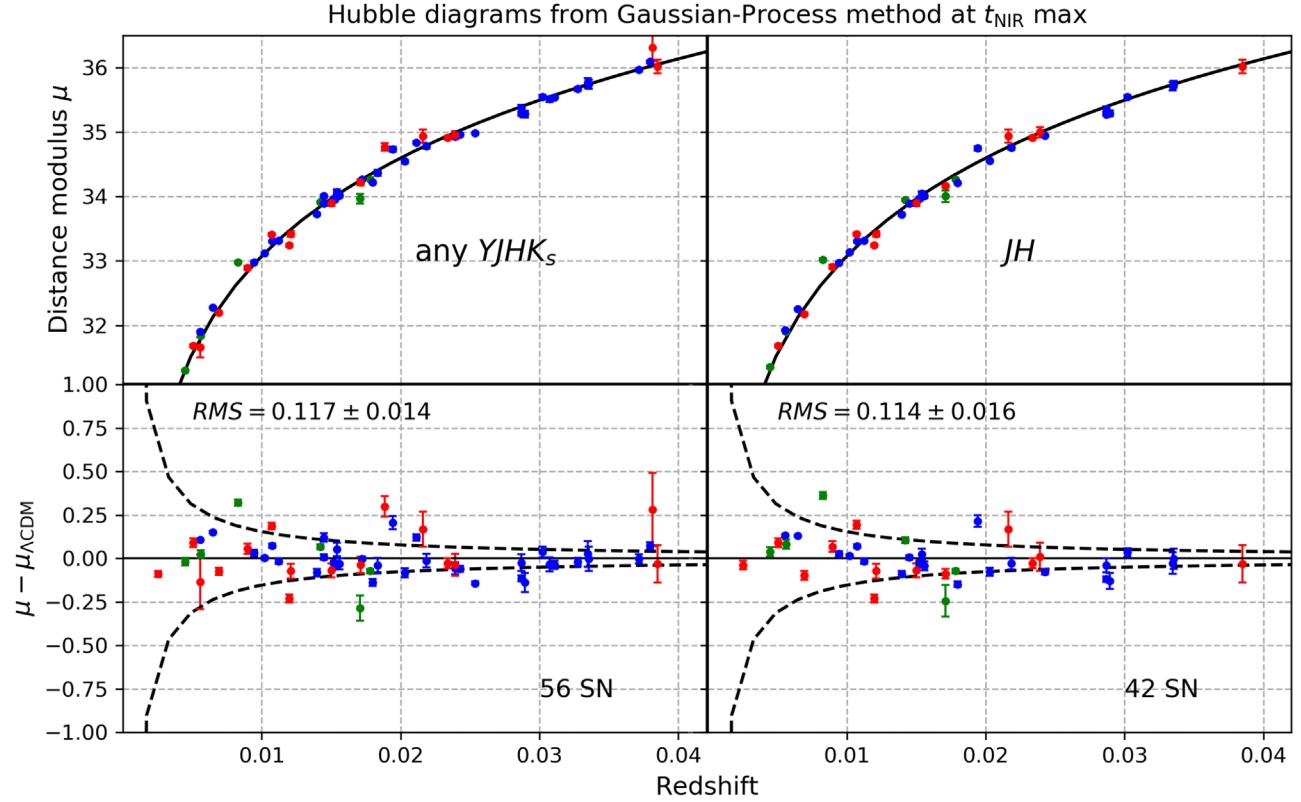
Figure 7. Similar to Figure 6, but for $YJHK_s$ Hubble diagrams (top row) and residuals (bottom row) using the GP method at NIR max. Again, Tables 7 and 8 summarize the intrinsic scatter in the Hubble diagrams, while Table 13 lists numerical values of the distance moduli from this figure.

Hubble diagrams from Gaussian-Process method at t_B max
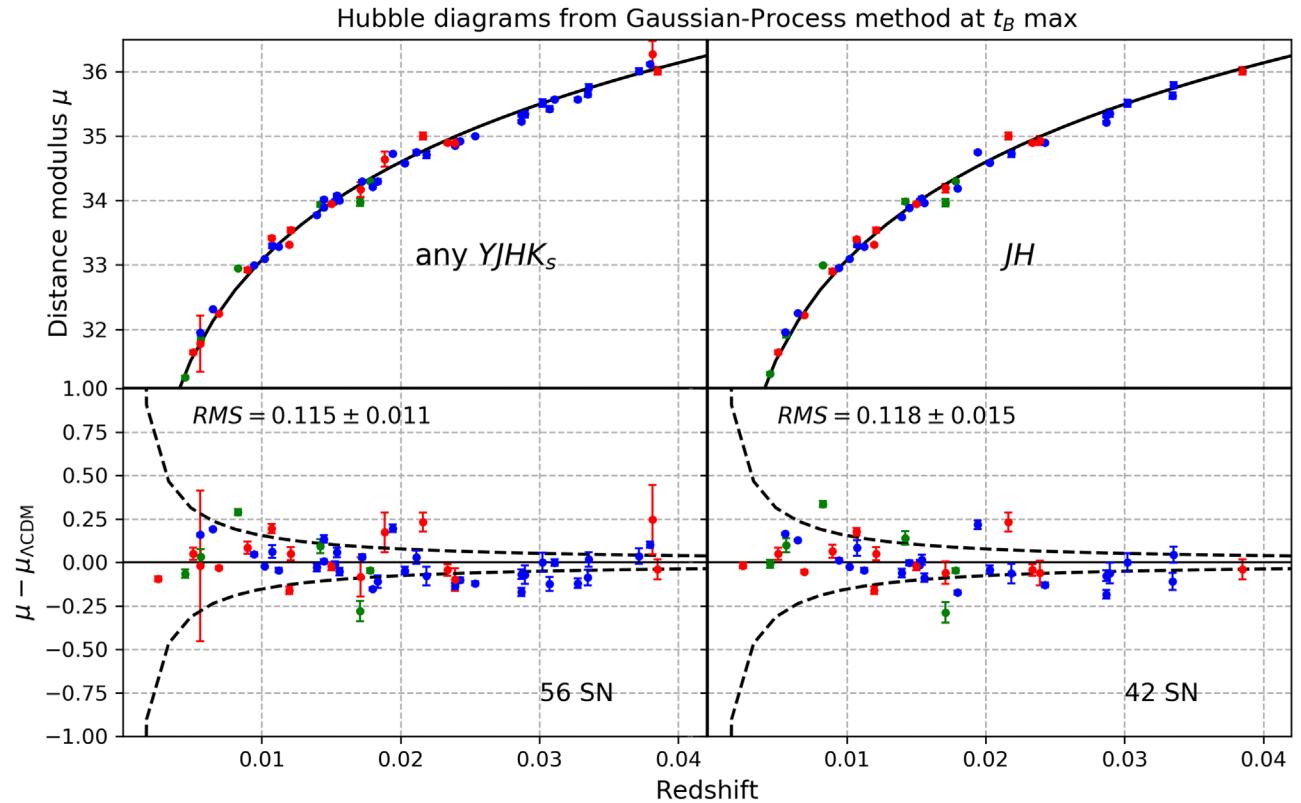
Figure 8. Similar to Figure 7, but for $YJHK_s$ Hubble diagrams (top row) and residuals (bottom row) using the GP method at B max. Again, Tables 7 and 8 summarize the intrinsic scatter in the Hubble diagram while Table 14 shows numerical values of the distance moduli from this figure.
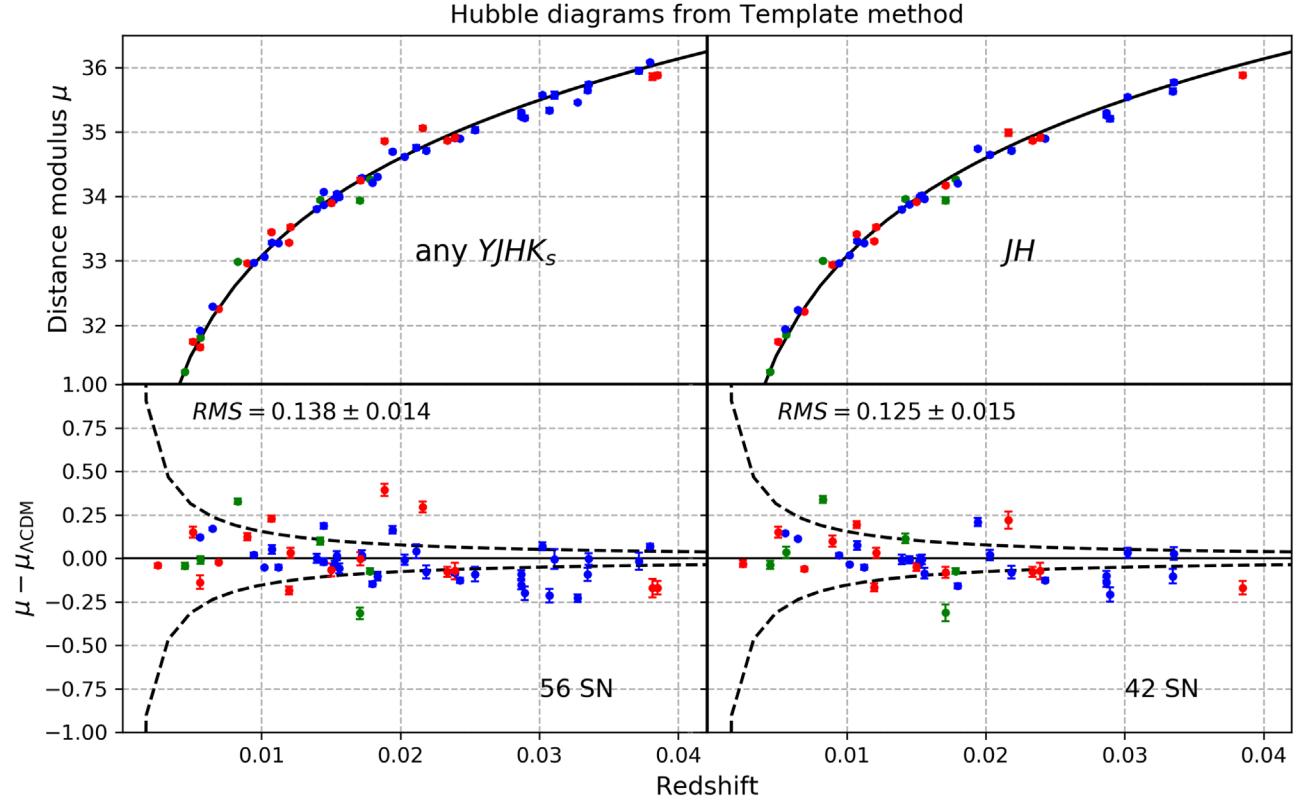
Figure 9. Similar to Figure 6 but applying the template method to exactly the same 56 SNe shown in Figures 7 and 8. Again, Table 7 summarizes the intrinsic scatter in the Hubble diagram while Table 12 shows numerical values of the distance moduli from this figure.
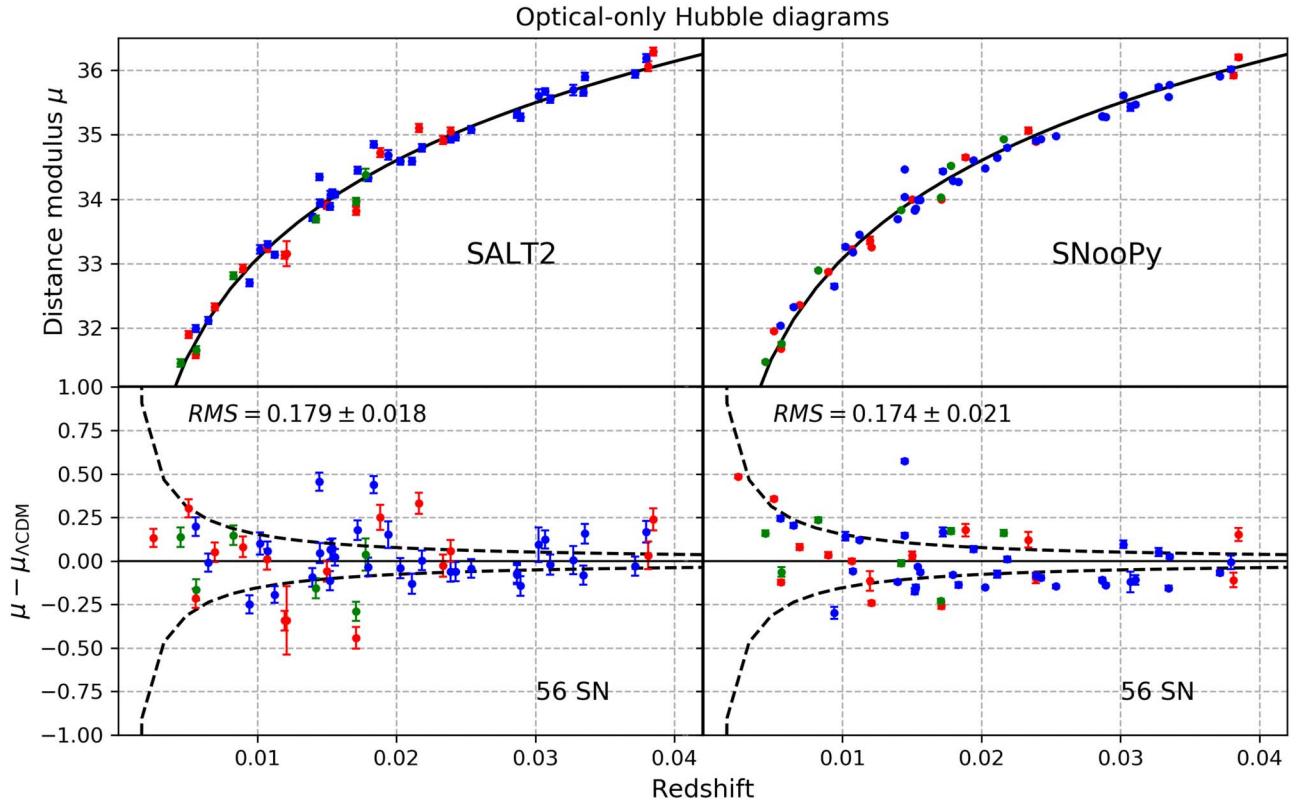
Figure 10. Hubble diagram (top row) and residuals (bottom row) using SALT2 and SNooPy to fit only the *optical BVR*-band LCs for exactly same sample of 56 SNe Ia used for the "any *YJHK$_s$*," GP (NIR max) Hubble diagram shown in the left panel of Figure 7 and listed in Table 13. As emphasized in Tables 7–10, the intrinsic scatter is clearly larger in these optical only Hubble diagrams compared with the GP NIR max ones constructed for the same 56 SNe Ia. Table 15 shows numerical values of the distance moduli from this figure.
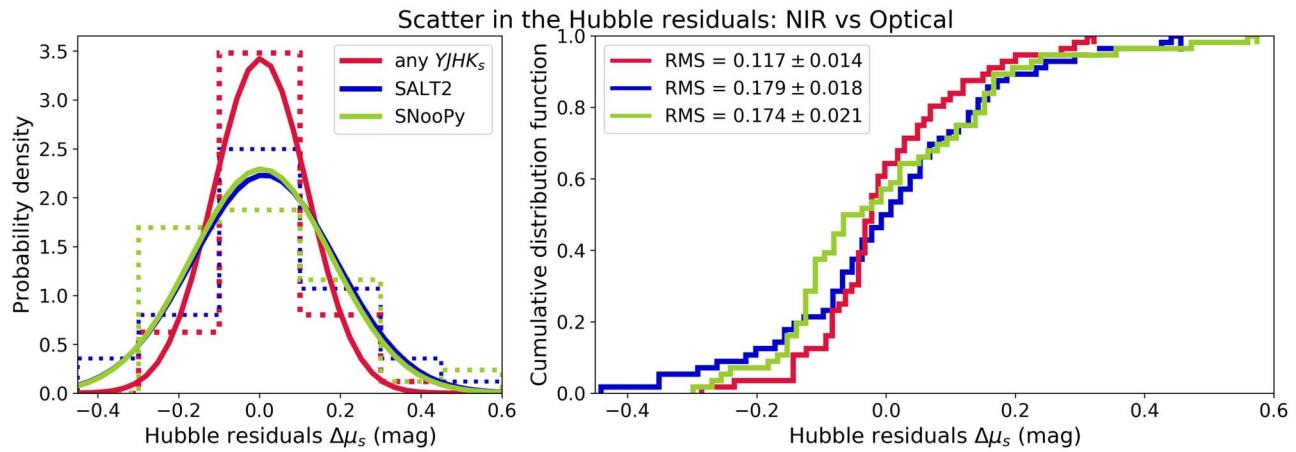
Figure 11. Comparing the scatter in the Hubble residuals, $\{\Delta\mu_s\}$, as defined in Equation (21), using NIR and optical methods for the same 56 SNe Ia. The red, green, and blue colors correspond to the Hubble residuals from the "any $YJHK_s$" GP (NIR max) method (lower left panel of Figure 7), SALT2 (lower left panel of Figure 10), and SNooPy (lower right panel of Figure 10), respectively. The left panel shows histograms (dashed lines) and Gaussian approximation to the histograms (solid lines) of the Hubble residuals, where we observe that the distribution of the NIR Hubble residuals (red) is *narrower* than either optical distribution (blue or green). The right panel shows the corresponding cumulative probability distribution functions, where we also note that the slope of the NIR curve is *steeper* than the optical curves, asymptotic to 1 at a smaller value of $\Delta\mu$, again indicating that the Hubble residual scatter is smaller in the NIR compared to the optical.
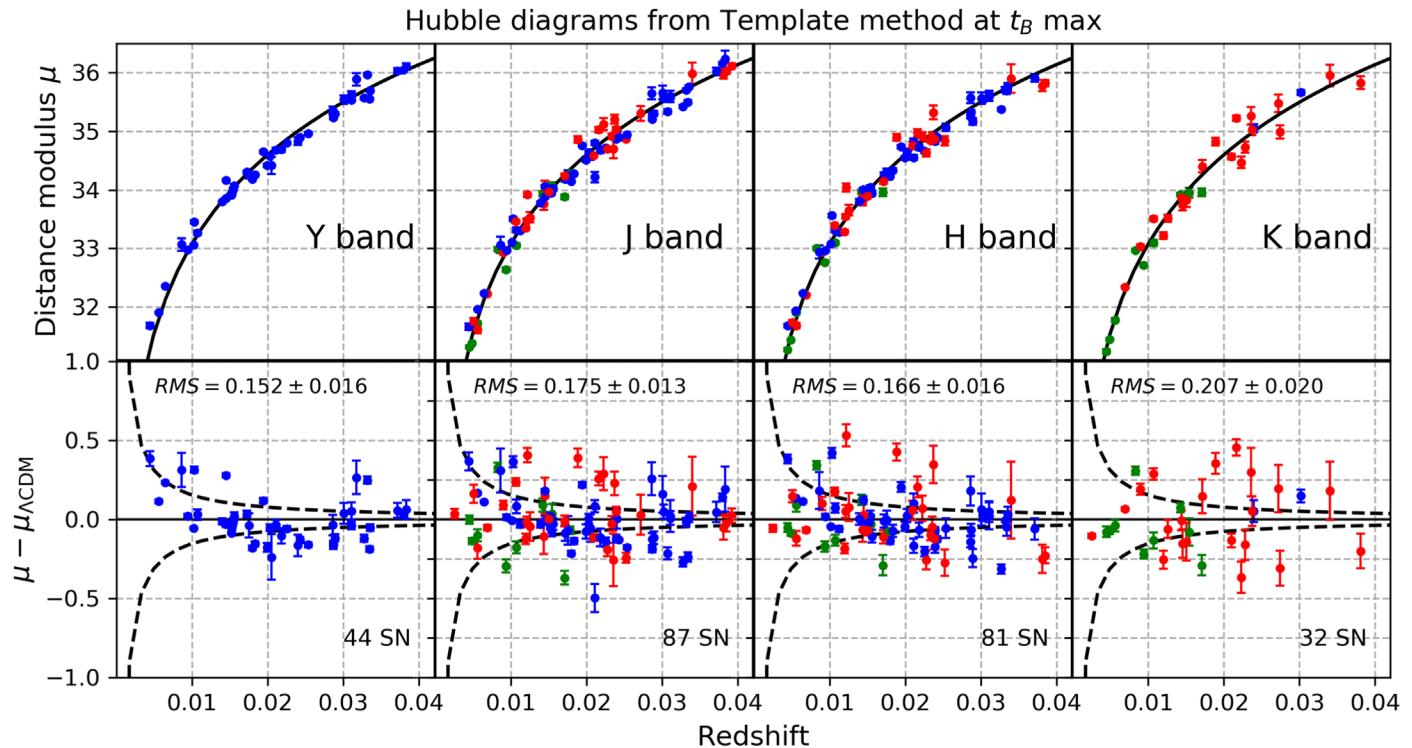
Figure 12. Individual $YJHK_s$ Hubble diagrams (top row) and residuals (bottom row) using the template method. Points are color coded by NIR photometric data source, including the CfA (red; Wood-Vasey et al. 2008; Friedman et al. 2015), the CSP (blue; Krisciunas et al. 2017), and other data from the literature (green; see Table 2). Note that only the CSP used a Y-band filter. In Table 12, we report the numerical values of the distance moduli shown in this figure. Table 8 shows the intrinsic scatter in the Hubble diagram.

Hubble residuals is steeper than for either optical curve. Both approaches suggest that the Hubble residual scatter is smaller in the NIR compared to the optical; a larger sample of SNe Ia in the NIR would strengthen the evidence for this conclusion.

6. Conclusions

This work bolsters and confirms a growing body of evidence that SNe Ia in NIR are excellent standard candles in the $YJHK_s$

bands in comparison to the optical BVR bands. Depending on the NIR data subset, when using multiple NIR bands, our GP method performs 2.3–4.1σ better in rms than either the SALT2 or SNooPy LC fitters for the same 56 SNe Ia using BVR data and applying LC shape and color corrections. Using a suitable subset of the existing low-redshift sample including 89 spectroscopically normal SNe Ia with NIR data, $YJHK_s$ (or JH or YJH) photometry alone already provides a simple means to estimate accurate and precise host galaxy distances in each

Hubble diagrams from Gaussian-Process method at t_{NIR} max
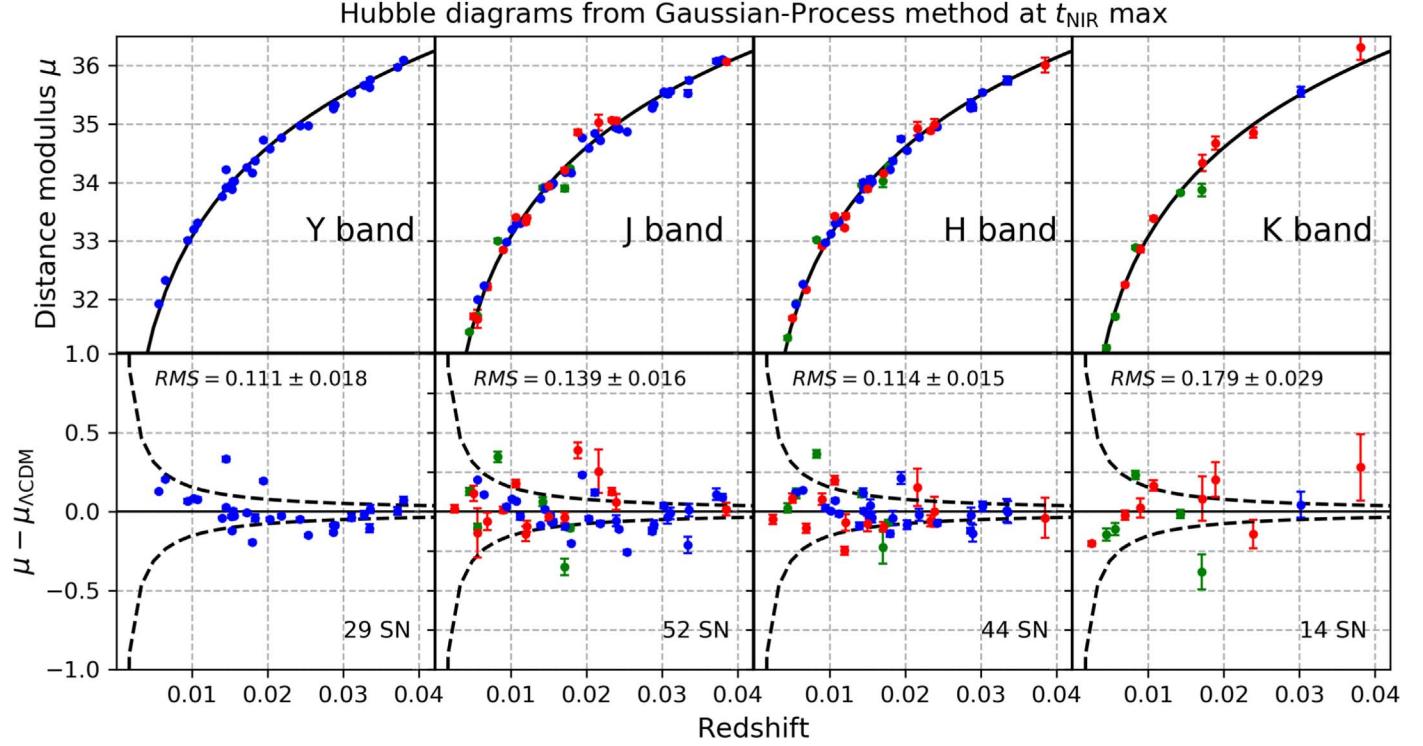
Figure 13. Individual $YJHK_s$ Hubble diagrams (top row) and residuals (bottom row) using the GP method at NIR max. See the caption of Figure 12. In Table 13, we report the numerical values of the distance moduli shown in this figure.

Hubble diagrams from Gaussian-Process method at t_B max
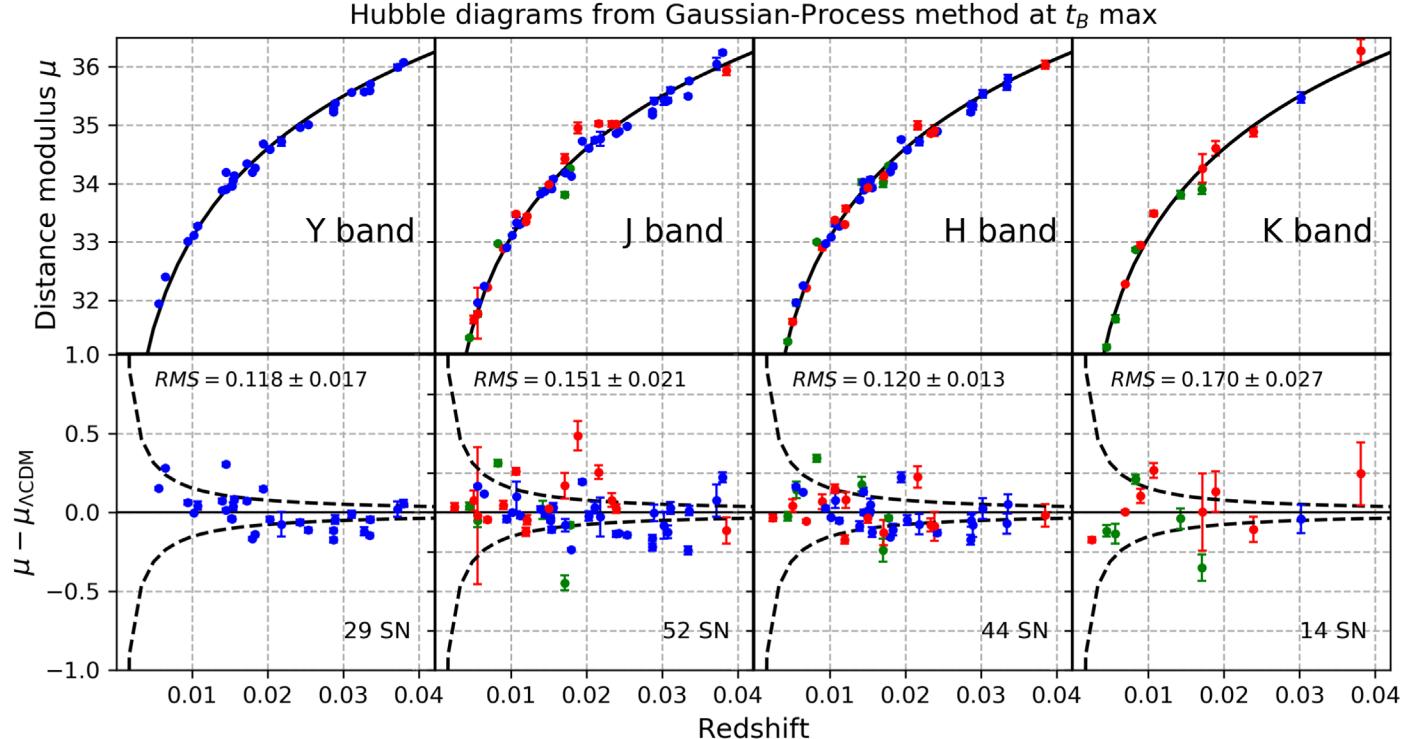
Figure 14. Individual $YJHK_s$ Hubble diagrams (top row) and residuals (bottom row) using the GP method at B max. See the caption of Figure 12. In Table 14, we report the numerical values of the distance moduli shown in this figure.

band, without the LC shape or host galaxy dust reddening corrections required for optical data.

In this work, we employed a hierarchical Bayesian model combined with a GP LC fitter to construct new mean NIR LC templates. We then used these templates, along with Milky Way dust corrections, NIR K-corrections, and the measured spectroscopic redshifts (corrected for local velocity flows) and redshift-independent distance information (e.g., Cepheids) for special cases, to estimate host-galaxy distances and uncertainties and construct Hubble diagrams in each of the individual

Table 15
SNe Ia Distance Moduli from the Optical *BVR* Bands

SN Name	Source	SALT2 (mag)	SNooPy (mag)
SN1998bu	CfA	30.214 ± 0.052	30.562 ± 0.009
SN2005cf	CfA	32.327 ± 0.056	32.355 ± 0.017
SN2006D	CfA	32.923 ± 0.060	32.877 ± 0.015
SN2006lf	CfA	33.153 ± 0.196	33.254 ± 0.013
SN2008gb	CfA	36.062 ± 0.079	35.920 ± 0.042
SN2008hs	CfA	34.721 ± 0.072	34.649 ± 0.036
SN2009al	CfA	34.916 ± 0.064	35.065 ± 0.045
SN2009an	CfA	33.236 ± 0.059	33.225 ± 0.013
SN2009bv	CfA	36.292 ± 0.064	36.204 ± 0.036
SN2010ai	CfA	35.051 ± 0.062	34.895 ± 0.029
SN2010kg	CfA	33.814 ± 0.062	33.999 ± 0.018
SN2011ao	CfA	33.130 ± 0.057	33.359 ± 0.056
SN2011B	CfA	31.585 ± 0.055	31.678 ± 0.014
SN2011by	CfA	31.898 ± 0.052	31.953 ± 0.012
SN2011df	CfA	33.909 ± 0.060	33.999 ± 0.022
SN1999ee	K04b	33.138 ± 0.048	33.454 ± 0.010
SN2000ca	K04b	34.933 ± 0.058	34.910 ± 0.014
SN2001ba	K04b	35.607 ± 0.100	35.609 ± 0.020
SN2004eo	CSP	33.884 ± 0.054	33.823 ± 0.017
SN2004ey	CSP	34.096 ± 0.057	33.991 ± 0.006
SN2005el	CSP	34.070 ± 0.057	33.853 ± 0.015
SN2005iq	CSP	35.903 ± 0.057	35.771 ± 0.011
SN2005kc	CSP	33.936 ± 0.057	34.038 ± 0.013
SN2005ki	CSP	34.589 ± 0.057	34.479 ± 0.007
SN2006ax	CSP	34.329 ± 0.053	34.284 ± 0.010
SN2006bh	CSP	33.292 ± 0.055	33.178 ± 0.011
SN2006bt	CSP	35.672 ± 0.052	35.429 ± 0.060
SN2006kf	CSP	34.686 ± 0.077	34.602 ± 0.017
SN2007A	CSP	34.447 ± 0.057	34.436 ± 0.025
SN2007af	CSP	31.993 ± 0.053	32.041 ± 0.015
SN2007ai	CSP	35.695 ± 0.081	35.742 ± 0.023
SN2007as	CSP	34.848 ± 0.049	34.273 ± 0.015
SN2007bc	CSP	34.588 ± 0.057	34.645 ± 0.020
SN2007bd	CSP	35.554 ± 0.059	35.467 ± 0.027
SN2007ca	CSP	34.343 ± 0.053	34.462 ± 0.012
SN2007jg	CSP	36.189 ± 0.062	36.014 ± 0.039
SN2007le	CSP	32.117 ± 0.053	32.330 ± 0.014
SN2008ar	CSP	35.274 ± 0.057	35.279 ± 0.010
SN2008bc	CSP	34.074 ± 0.047	33.990 ± 0.010
SN2008bf	CSP	35.083 ± 0.054	34.979 ± 0.010
SN2008gp	CSP	35.659 ± 0.055	35.584 ± 0.012
SN2008hj	CSP	35.943 ± 0.056	35.905 ± 0.013
SN2008hv	CSP	33.715 ± 0.054	33.691 ± 0.011
SN2009aa	CSP	35.318 ± 0.056	35.284 ± 0.007
SN2009ad	CSP	35.328 ± 0.056	35.289 ± 0.011
SN2009ag	CSP	33.219 ± 0.064	33.261 ± 0.025
SN2009cz	CSP	34.797 ± 0.057	34.803 ± 0.017
SN2009D	CSP	34.965 ± 0.054	34.930 ± 0.015
SN2009Y	CSP	32.700 ± 0.053	32.650 ± 0.034
SN1999ek	K04c	34.380 ± 0.092	34.517 ± 0.017
SN2000E	V03	31.655 ± 0.060	31.756 ± 0.028
SN2001bt	K04c	33.691 ± 0.057	33.836 ± 0.016
SN2001cz	K04c	33.964 ± 0.056	34.026 ± 0.011
SN2001el	K03	31.457 ± 0.055	31.479 ± 0.017
SN2002dj	P08	32.810 ± 0.056	32.899 ± 0.014
SNf20080514-002	CfA	35.102 ± 0.061	34.933 ± 0.017

Note. Distance moduli estimated by fitting the optical *BVR* bands for the same 56 SNe listed in Table 13 using the SALT2 and SNooPy fitters. The Hubble diagrams for these 2 cases are shown in Figure 10. Reference codes for the data Source are the same as in Table 2.

YJHK$_s$ bands. When considering NIR-only methods, our GP method referenced to the time of NIR maximum yields slightly smaller Hubble diagram intrinsic scatter and error wrms than when referenced to *B* max and significantly smaller intrinsic scatter compared to the template method.

Our approach is intermediate in complexity between earlier analyses by our group by Wood-Vasey et al. (2008) and the BAYESN approach detailed in Mandel et al. (2009, 2011). The BAYESN methodology presents a coherent, principled, hier-archical Bayesian model that takes into account the full correlation structure between all the input optical and NIR bandpasses, both in color and phase, in order to determine the posterior distributions for distance moduli μ, host galaxy dust estimates A_V, and separate R_V values for each SN. Nevertheless, BAYESN is considerably more complex to implement than the simpler analysis methods in this work, which worked relatively well for our sample of NIR data.

Compared to optical LCs, NIR SNe Ia LCs have a narrow luminosity distribution, and are less sensitive to host galaxy dust extinction. This could help to limit systematic galaxy distance errors that arise from the degeneracy between the intrinsic SNe Ia colors and reddening of light by dust, which affects optical-only SNe Ia cosmology (Krisciunas et al. 2004a; Wood-Vasey et al. 2008; Mandel et al. 2009, 2011, 2017; Folatelli et al. 2010; Burns et al. 2011, 2014; Kattner et al. 2012; Scolnic et al. 2014a, 2017). Studies combining NIR and optical SNe Ia photometry have already shown that the addition of NIR data is an extremely promising way to break the degeneracy between intrinsic color and dust reddening, allowing distance estimates to become increasingly insensitive to the assumptions behind individual LC-fitting models (Mandel et al. 2011, 2014).

We have recently begun to augment the existing low-z SNe Ia in NIR sample from the CfA, CSP, and other groups using the *HST* RAISIN program in Cycles 20 and 23 (Kirshner 2012, 2014; Foley et al. 2013; Kirshner & The RAISIN TEAM 2014). In RAISIN1, we observed 23 SNe Ia at $z \sim 0.35$ in the rest-frame NIR with WFC3/IR, followed by observations of 24 additional SNe Ia at $z \sim 0.5$ for RAISIN2. Each of these *HST* NIR observations was accompanied by well-sampled ground-based optical photo-metry from Pan-STARRS (PS1; Rest et al. 2014; Jones et al. 2018; Scolnic et al. 2018) and the DES (Dark Energy Survey Collaboration et al. 2016, 2018, 2019a, 2019b, 2019c, 2019d, 2019e). Analysis of the RAISIN data will be presented in future work.

The evidence from this work further emphasizes the promise of NIR wavelength observations not only for the ongoing *HST* RAISIN project, but also for future space studies of cosmic acceleration and dark energy (Beaulieu et al. 2010; Gehrels 2010; Astier et al. 2011; Hounsell et al. 2018; Riess et al. 2018c). Upcoming missions that could exploit nearby NIR data as a low-z anchor include the Large Synoptic Survey Telescope (LSST; Ivezic et al. 2019), the NASA *Wide-Field Infrared Survey Telescope* (*WFIRST*-AFTA; Gehrels 2010; Spergel et al. 2015), the European Space Agency's EUCLID mission (Beaulieu et al. 2010; Wallner et al. 2017), and the NASA *James Webb Space Telescope* (*JWST*; Clampin 2011; Greenhouse 2016).

Near-infrared photometry can also augment our knowledge of the spectral energy distribution of SNe Ia; for example for the implementation of the Type Ia parametrized SALT2 model, which is currently poorly constrained at infrared wavelengths (Pierel et al. 2018a, 2018b). This will dovetail nicely with the NIR capabilities of *JWST* and *WFIRST* and be useful for future SNe Ia surveys.

Methods such as BAYESN (Mandel et al. 2009, 2011), SNooPy (Burns et al. 2011), and SALT2ext (Pierel et al. 2018a, 2018b) that use empirical LC fitters and provide host galaxy distance estimates using both optical and NIR data can be extended to obtain cosmological inferences and dark energy constraints using both low-z and high-z samples. Combining the growing low-redshift SNe Ia in NIR samples from the CfA, CSP, and other samples in the literature with higher redshift optical and NIR data sets will continue to lay the foundation for ongoing and future ground- and space-based SN cosmology experiments, which seek to further test whether dark energy is best described by Einstein's cosmological constant Λ or some other physical mechanism that varies on cosmic timescales.

Appendix A
Gaussian Process Regression

Given the data set of observations in an absolute magnitude NIR LC, (M, t) for a given SN, we want to use this information to estimate the latent absolute magnitudes $\mathcal{M}^*$ at a grid of phases t^* described in Section 3.2. To do so, we define a GP with these data and variables.

Table 16
Values of the GP Hyperparameters

Band	l	σ_K
Y	7.90	0.70
J	7.02	0.95
H	9.81	0.75
K_s	8.19	0.55

To model the covariance $\mathrm{Cov}[\mathcal{M}^*, \mathcal{M}^{*\top}]$ we choose the squared exponential GP kernel that is defined as

$$k(t_i, t_j) = \sigma_K^2 \exp\left[-\frac{(t_i - t_j)^2}{2l^2}\right], \qquad (32)$$

where σ_K and l are the GP kernel hyperparameters, the computation of which is explained at the end of this section. We choose the GP kernel of Equation (32) because it is simple, produces smooth curves, and has the general properties we need to model the observed shapes of the NIR LCs: for two phases very close to each other, $t_i \sim t_j$, their covariance is close to 1, and for distant phases, $t_i \ll t_j$, then $k(t_i, t_j) \sim 0$, such that they are almost uncorrelated.

We also take into account the uncertainty associated with each datum $M(t_i)$ in the variance $\sigma_M^2 = \sigma_m^2 + \sigma_A^2 + \sigma_{K\mathrm{corr}}^2 + \sigma_{\mu_{\mathrm{pec}}}^2$ (see Equation (7) for details), by defining the total covariance between two data points as

$$\mathrm{Cov}[M_i, M_j] = k(t_i, t_j) + \delta_{ij}(\sigma_m^2 + \sigma_{K\mathrm{corr}}^2) + \sigma_{\mu_{\mathrm{pec}}}^2 + \sigma_A^2, \qquad (33)$$

where δ_{ij} is the Kronecker delta function, and we assume that the measurement and K-correction errors are independent between two different M_i and M_j, but that both the peculiar-velocity distance error and the Milky Way extinction error are not independent at different times because they are the same over the whole LC in a single filter for a given SN. In matrix notation we can write Equation (33) for all the data M in a LC as

$$\mathrm{Cov}[M, M^\top] = K(t, t) + W + (\sigma_{\mu_{\mathrm{pec}}}^2 + \sigma_A^2)1 \cdot 1^\top, \qquad (34)$$

where $K(t, t)$ is a square matrix with elements given by Equation (32), W is a diagonal matrix of dimension $n \times n$ with elements given by

$$W_{ij} = \delta_{ij}(\sigma_m^2 + \sigma_{K\mathrm{corr}}^2), \qquad (35)$$

and 1 is a vector of ones, so that the term $(\sigma_{\mu_{\mathrm{pec}}}^2 + \sigma_A^2)1 \cdot 1^\top$, is a square matrix of dimension $n \times n$ with elements all equal to $(\sigma_{\mu_{\mathrm{pec}}}^2 + \sigma_A^2)$.

Following the standard GP formalism (e.g., Chapter 2 of Rasmussen & Williams 2006), we first write the joint distribution of the observed absolute magnitudes, M, and latent absolute magnitudes, $\mathcal{M}^*$, with a constant prior mean as

$$\begin{bmatrix} M \\ M^* \end{bmatrix} \sim N\left(\begin{bmatrix} a1 \\ a1^* \end{bmatrix}, \begin{bmatrix} K(t, t) + W + (\sigma_{\mu_{\mathrm{pec}}}^2 + \sigma_A^2)1 \cdot 1^\top & K(t, t^*) \\ K(t^*, t) & K(t^*, t^*) \end{bmatrix}\right), \qquad (36)$$

where 1 and l* are vectors of ones and of dimensions n and n^* respectively, and a is a scalar that we assign the value of -17.5, -17, -18, and -18 mag for the Y, J, H, and K_s bands, respectively. We assume these values of a just for computational convenience in the GP fitting, and verified that the final templates are insensitive to these choices over a wide range of values for a. The matrices $K(t, t)$, $K(t^*, t)$, $K(t, t^*)$, and $K(t^*, t^*)$, are of dimensions $n \times n$, $n^* \times n$, $n \times n^*$, and $n^* \times n^*$, respectively, with elements defined by Equation (32).

The conditional distribution of $\mathcal{M}^*$ given t, t^* and M, can be written as

$$M^* | t, t^*, M \sim N(\mu^{\text{post}}, \Sigma^{\text{post}}), \qquad (37)$$

where the posterior mean μ^{post} and posterior covariance Σ^{post} are given as

$$\mu^{\text{post}} \equiv \mathbb{E}[M^* | t, t^*, M] = a1 + K(t^*, t)$$
$$\times [K(t, t) + W + (\sigma_{\mu_{\text{pec}}}^2 + \sigma_A^2)1 \cdot 1^\top]^{-1} (M - a1), \quad (38)$$

$$\Sigma^{\text{post}} \equiv \text{Cov}[\mathcal{M}^*, \mathcal{M}^{*\top} | t, t^*, M]$$
$$= K(t^*, t^*) - K(t^*, t)$$
$$\times [K(t, t) + W + (\sigma_{\mu_{\text{pec}}}^2 + \sigma_A^2)1 \cdot 1^\top]^{-1}K(t, t^*).$$
$$(39)$$

The final values we obtain from the GP regression are the vector μ^{post} and the matrix Σ^{post}, which we estimate using Equations (38) and (39), respectively.

The coefficients σ_K and l in Equation (32) are called the *hyperparameters* of the GP kernel that we determine by assuming that the LCs for all the SN in a given NIR band are independent of each other, and that the GP hyperparameters describe the *population* of the SN LCs in a given band rather than each individual LC. With these assumptions, we can write the global marginal likelihood distribution

$$p(\{M\}_s | \{t\}_s, \sigma_K, l)$$
$$= \prod_{s=1}^{N_T} \mathcal{N}(M_s | a\, 1_s,\ K_s(t_s, t_s)$$
$$+ W_s(t_s, t_s) + (\sigma_{\mu_{\text{pec}},s}^2 + \sigma_{A,s}^2)1_s \cdot 1_s^\top), \qquad (40)$$

where the subindex s refers to quantities for SN s, N_T is the number of SNe Ia used to construct the normalized LC template in a given NIR band, and "$\{\ \}_s$" means the collection of values from all the N_T SNe Ia. To compute the MLE values for (σ_K, l), we minimize the negative of the logarithm of Equation (40), obtaining the values shown in Table 16.

A.1. Normalization of the GP Light Curves

In Section 3.2.1, we explained that we are primarily interested in the *shape* of the light curves. For this reason, after determining the posterior light curve described by $(\mu^{\text{post}}, \Sigma^{\text{post}})$, we *normalize* the LC using $t_{B\,\text{max}}$ as the reference time where the light curve will have a value of zero.

First, for computational convenience, we rewrite the linear transformation of Equation (9) as the matrix operation

$$L = AM^*, \qquad (41)$$

where A is a $n^* \times n^*$ square matrix defined as $A \equiv I - V_k$, where I is the identity matrix, and V_k is a matrix containing

only ones in the kth column and zeros everywhere else, assuming that the kth element of t^* correspond to phase $t_k^* = t_{B\,\text{max}}$.

We compute the mean of the normalized LC as, $\mu^L = \mathbb{E}[L|\mathcal{D}] = A\,\mathbb{E}[\mathcal{M}^*|\mathcal{D}] = A\mu^{\text{post}}$, where $\mathcal{D} \equiv (t, t^*, M)$ is the conditional data in Equation (37). And the covariance is given by

$$\Sigma^L = A\Sigma^{\text{post}}A^\top. \qquad (42)$$

From these expressions at $t_k^* = t_{B\,\text{max}}$, the posterior mean and variance of the normalized LCs are both identically zero:

$$\mathbb{E}[L_k|\mathcal{D}] = 0, \qquad \text{Var}[L_k, L_k|\mathcal{D}] = 0, \qquad (43)$$

which is required for self-consistency with the definition of the normalized LC.

Appendix B
Hierarchical Bayesian Model

Using Bayes' theorem, applying the product rule for probability, and assuming conditional independence of the means of the normalized LCs, μ_s^L's, with respect to the population mean and variance $(\theta, \sigma_\theta^2)$, we can write the joint posterior distribution in our hierarchical model as

$$p(\{\eta_s\}, \theta, \sigma_\theta | \{\mu_s^L, \sigma_{\eta,s}\}) \propto p(\theta, \sigma_\theta) \times p(\{\eta_s\}|\theta, \sigma_\theta)$$
$$\times p(\{\mu_s^L\}|\{\eta_s\}, \{\sigma_{\eta,s}\}). \qquad (44)$$

Inserting Equations (10) and (11) into (44), we obtain,

$$p(\{\eta_s\}, \theta, \sigma_\theta | \{\mu_s^L, \sigma_{\eta,s}\}) \propto p(\theta, \sigma_\theta) \times \prod_{s=1}^{N_T^*} N(\eta_s | \theta, \sigma_\theta^2)$$
$$\times \prod_{s=1}^{N_T^*} N(\mu_s^L | \eta_s, \sigma_{\eta,s}^2),$$
$$(45)$$

where N_T^* is the number of SNe for which we have determined the best fitting function at phase t^*. Note that since each LC has a *different* number of photometric data points over *different* phase ranges, this implies that N_T^* is different for each phase t^*.

For computation convenience, following Gelman et al. (2014), we decompose the joint posterior distribution using the product rule as

$$p(\{\eta_s\}, \theta, \sigma_\theta | \{\mu_s^L, \sigma_{\eta,s}\}) \propto p(\{\eta_s\}|\theta, \sigma_\theta, \{\mu_s^L, \sigma_{\eta,s}\})$$
$$\times p(\theta|\sigma_\theta, \{\mu_s^L, \sigma_{\eta,s}\}) \times p(\sigma_\theta|\{\mu_s^L, \sigma_{\eta,s}\}), \qquad (46)$$

where the first factor to the right of the proportionality sign of Equation (46) can be written for the SN s as

$$p(\eta_s|\theta, \sigma_\theta, \mu_s^L, \sigma_{\eta,s}) = \mathcal{N}(\eta_s|\rho_s, R_s), \qquad (47)$$

where

$$\rho_s \equiv \frac{\mu_s^L/\sigma_{\eta,s}^2 + \theta/\sigma_\theta^2}{1/\sigma_{\eta,s}^2 + 1/\sigma_\theta^2}, \qquad (48)$$

and

$$R_s \equiv \frac{1}{1/\sigma_{\eta,s}^2 + 1/\sigma_\theta^2}. \qquad (49)$$

The middle factor to the right of the proportionality sign of Equation (46) can be written as

$$p(\theta \mid \sigma_\theta, \{\mu_s^L, \sigma_{\eta,s}\}) = \mathcal{N}(\theta \mid \hat{\theta}, R), \qquad (50)$$

where

$$\hat{\theta} \equiv \frac{\sum_{s=1}^{N_T^*} \mu_s^L (\sigma_{\eta,s}^2 + \sigma_\theta^2)^{-1}}{\sum_{s=1}^{N_{SN}} (\sigma_{\eta,s}^2 + \sigma_\theta^2)^{-1}}, \qquad (51)$$

and

$$R^{-1} \equiv \sum_{s=1}^{N_T^*} \frac{1}{\sigma_{\eta,s}^2 + \sigma_\theta^2}. \qquad (52)$$

Finally, the last term to the right of the proportionality sign can be written as

$$p(\sigma_\theta \mid \{\mu_s^L, \sigma_{\eta,s}\}) \propto R^{1/2} \prod_{s=1}^{N_T^*} (\sigma_{\eta,s}^2 + \sigma_\theta^2)^{-1/2}$$
$$\times \exp\left(\frac{-(\mu_s^L - \hat{\theta})^2}{2(\sigma_{\eta,s}^2 + \sigma_\theta^2)}\right), \qquad (53)$$

where we are assuming a uniform prior distribution $p(\sigma_\theta) \propto 1$.

We use Equation (46) combined with Equations (47)–(53) to simultaneously determine the posterior best estimates of ($\{\eta_s\}, \theta, \sigma_\theta$) at phase t^*, given the data $\{\mu_s^L, \sigma_{\eta,s}\}$, following the computational procedure described in Appendix C.3, subsection "Marginal and conditional simulation for the normal model", of Gelman et al. (2014). We use the R code presented there to build our R code to make the computations described in this work.

Appendix C
rms, wrms, and the Intrinsic Scatter

We use the rms to quantify the scatter in the Hubble residuals because it is simple and straightforward to compute and compare with the Hubble residuals reported by other authors. The definition we use is

$$\text{rms} = \sqrt{N_{SN}^{-1} \left(\sum_{s=1}^{N_{SN}} \Delta\mu_s^2\right)}, \qquad (54)$$

where N_{SN} is the total number of SNe Ia in the Hubble diagram. We compute the uncertainty on rms using bootstrap resampling.

To weight the rms by the uncertainties in each SN distance modulus estimate in each NIR band, we compute the inverse-variance wrms of the residuals as

$$\text{wrms} = \sqrt{\left(\sum_{s=1}^{N_{SN}} w_s\right)^{-1} \sum_{s=1}^{N_{SN}} w_s \, \Delta\mu_s^2}, \qquad (55)$$

where $w_s \equiv 1/(\hat{\sigma}_{\text{fit},s}^2 + \hat{\sigma}_{\text{int}}^2 + \sigma_{\mu_{\text{pec}},s}^2)$ and $\Delta\mu_s$ is defined in Equation (21). We also compute the uncertainty on wrms using bootstrap resampling.

We determine the *intrinsic scatter*, σ_{int}, in the Hubble residual following the procedure described in Equations (B.6)–(B.7) in Appendix B of Blondin et al. (2011). This dispersion tries to quantify the scatter due to intrinsic differences in the NIR SNe Ia absolute magnitudes only and *not* due to the

peculiar-velocity uncertainty of each SN. The intrinsic scatter corresponds to the remaining dispersion observed in the Hubble-diagram residuals *after* accounting for the uncertainty in distance modulus due to the peculiar-velocity uncertainty, $\sigma_{\mu_{\text{pec}},s}^2$, and the photometric errors $\{\hat{\sigma}_{\text{fit},s}\}$. When comparing our notation to Equations (B.6)–(B.7) of Blondin et al. (2011), note that where we use $\sigma_{\text{fit},s}$, σ_{int} and $\sigma_{\mu_{\text{pec}},s}$, Blondin et al. (2011) instead uses the notation $\sigma_{m,s}$, σ_{pred}, and $\sigma_{\text{pec},s}$, respectively.

Appendix D
Covariance Matrix C_μ of Hubble Residuals

In this section we provide the numerical values for different cases of the covariance matrix C_μ.

For the template method, we find the following values of the sample covariance matrix C_μ for the *YJH* bands:

$$C_\mu = \begin{pmatrix} 0.0227 & 0.0192 & 0.0167 \\ 0.0192 & 0.0246 & 0.0201 \\ 0.0167 & 0.0201 & 0.0211 \end{pmatrix}, \qquad (56)$$

and for the *JHK$_s$* bands:

$$C_\mu = \begin{pmatrix} 0.0356 & 0.0276 & 0.0202 \\ 0.0276 & 0.0317 & 0.0237 \\ 0.0202 & 0.0237 & 0.0426 \end{pmatrix}. \qquad (57)$$

For the GP method, we find the following values for the sample covariance matrix for the *YJH* bands:

$$C_\mu = \begin{pmatrix} 0.0109 & 0.0110 & 0.0080 \\ 0.0110 & 0.0133 & 0.0084 \\ 0.0080 & 0.0084 & 0.0080 \end{pmatrix}, \qquad (58)$$

and for the *JHK$_s$* bands:

$$C_\mu = \begin{pmatrix} 0.0279 & 0.0217 & 0.0213 \\ 0.0217 & 0.0238 & 0.0192 \\ 0.0213 & 0.0192 & 0.0283 \end{pmatrix}. \qquad (59)$$

ORCID iDs

Arturo Avelino ⓘ https://orcid.org/0000-0002-2938-7822
Andrew S. Friedman ⓘ https://orcid.org/0000-0003-1334-039X
Kaisey S. Mandel ⓘ https://orcid.org/0000-0001-9846-4417
David O. Jones ⓘ https://orcid.org/0000-0002-6230-0151
Robert P. Kirshner ⓘ https://orcid.org/0000-0002-1966-3942

References

Alam, S., Ata, M., Bailey, S., et al. 2017, MNRAS, 470, 2617
Albareti, F. D., Allende Prieto, C., Almeida, A., et al. 2017, ApJS, 233, 25
Astier, P., Guy, J., Pain, R., & Balland, C. 2011, A&A, 525, A7
Astier, P., Guy, J., Regnault, N., et al. 2006, A&A, 447, 31
Barone-Nugent, R. L., Lidman, C., Wyithe, J. S. B., et al. 2012, MNRAS, 425, 1007
Barone-Nugent, R. L., Lidman, C., Wyithe, J. S. B., et al. 2013, MNRAS, 432, 90
Beaulieu, J. P., Bennett, D. P., Batista, V., et al. 2010, in ASP Conf. Ser. 430, Pathways Toward Habitable Planets, ed. V. Coudé Du Foresto, D. M. Gelino, & I. Ribas (San Francisco, CA: ASP), 266
Betoule, M., Kessler, R., Guy, J., et al. 2014, A&A, 568, A22
Blondin, S., Mandel, K. S., & Kirshner, R. P. 2011, A&A, 526, A81
Blondin, S., & Tonry, J. L. 2007, ApJ, 666, 1024
Burns, C. R., Parent, E., Phillips, M. M., et al. 2018, ApJ, 869, 56
Burns, C. R., Stritzinger, M., Phillips, M. M., et al. 2011, AJ, 141, 19
Burns, C. R., Stritzinger, M., Phillips, M. M., et al. 2014, ApJ, 789, 32
Calcino, J., & Davis, T. 2017, JCAP, 1, 038

Campbell, H., D'Andrea, C. B., Nichol, R. C., et al. 2013, ApJ, 763, 88
Cardelli, J. A., Clayton, G. C., & Mathis, J. S. 1989, ApJ, 345, 245
Cardona, W., Kunz, M., & Pettorino, V. 2017, JCAP, 3, 056
Carrick, J., Turnbull, S. J., Lavaux, G., & Hudson, M. J. 2015, MNRAS, 450, 317
Cartier, R., Hamuy, M., Pignata, G., et al. 2014, ApJ, 789, 89
Childress, M., Aldering, G., Aragon, C., et al. 2011, ApJ, 733, 3
Childress, M., Aldering, G., Antilogus, P., et al. 2013, ApJ, 770, 107
Chotard, N., Gangler, E., Aldering, G., et al. 2011, A&A, 529, L4
Clampin, M. 2011, Proc. SPIE, 8146, 814605
Conley, A., Carlberg, R. G., Guy, J., et al. 2007, ApJL, 664, L13
Conley, A., Guy, J., Sullivan, M., et al. 2011, ApJS, 192, 1
Conley, A., Sullivan, M., Hsiao, E. Y., et al. 2008, ApJ, 681, 482
Contreras, C., Hamuy, M., Phillips, M. M., et al. 2010, AJ, 139, 519
Courtois, H. M., & Tully, R. B. 2012, ApJ, 749, 174
Dark Energy Survey Collaboration, Abbott, T., Abdalla, F. B., et al. 2016, MNRAS, 460, 1270
Dark Energy Survey Collaboration, Abbott, T. M. C., Alarcon, A., et al. 2019c, PhRvL, 122, 171301
Dark Energy Survey Collaboration, Abbott, T. M. C., Allam, S., et al. 2019d, ApJL, 872, L30
Dark Energy Survey Collaboration, Brout, D., Scolnic, D., et al. 2019a, ApJ, 874, 150
Dark Energy Survey Collaboration, Brout, D., Sako, M., et al. 2019e, ApJ, 874, 106
Dark Energy Survey Collaboration, D'Andrea, C. B., Smith, M., et al. 2018, arXiv:1811.09565
Dark Energy Survey Collaboration, Kessler, R., Brout, D., et al. 2019b, MNRAS, 485, 1171
Davis, T. M., Hui, L., Frieman, J. A., et al. 2011, ApJ, 741, 67
Davis, T. M., & Parkinson, D. 2016, in Characterizing Dark Energy Through Supernovae, ed. A. W. Alsabti & P. Murdin (Cham: Springer International Publishing), 1
Dhawan, S., Jha, S. W., & Leibundgut, B. 2018, A&A, 609, A72
Dhawan, S., Leibundgut, B., Spyromilio, J., & Maguire, K. 2015, MNRAS, 448, 1345
Efstathiou, G. 2014, MNRAS, 440, 1138
Folatelli, G., Phillips, M. M., Burns, C. R., et al. 2010, AJ, 139, 120
Foley, R. J., Scolnic, D., Rest, A., et al. 2018, MNRAS, 475, 193
Foley, R., Kirshner, R., Challis, P., et al. 2013, RAISIN: Tracers of Cosmic Expansion with SN Ia in the IR, NOAO Proposal ID 2013A-0373 (Tucson, AZ: NOAO)
Freedman, W. L., Madore, B. F., Gibson, B. K., et al. 2001, ApJ, 553, 47
Friedman, A. S. 2012, PhD thesis, Harvard Univ., https://search.proquest.com/docview/1027769281
Friedman, A. S., Wood-Vasey, W. M., Marion, G. H., et al. 2015, ApJS, 220, 9
Frieman, J. A., Turner, M. S., & Huterer, D. 2008, ARA&A, 46, 385
Gehrels, N. 2010, arXiv:1008.4936
Gelman, A., Carlin, J. B., Stern, H. S., et al. 2014, Bayesian Data Analysis (3rd ed.; Boca Raton, FL: CRC Press)
Goldhaber, G., Groom, D. E., Kim, A., et al. 2001, ApJ, 558, 359
Goobar, A. 2015, in Proc. Thirteenth Marcel Grossmann Meeting, On Recent Developments in Theoretical and Experimental General Relativity, Astrophysics and Relativistic Field Theories, ed. K. Rosquist (Singapore: World Scientific Pub.), 167
Goobar, A., & Leibundgut, B. 2011, ARNPS, 61, 251
Greenhouse, M. A. 2016, Proc. SPIE, 9904, 990406
Guy, J., Astier, P., Nobili, S., Regnault, N., & Pain, R. 2005, A&A, 443, 781
Guy, J., Astier, P., Baumont, S., et al. 2007, A&A, 466, 11
Guy, J., Sullivan, M., Conley, A., et al. 2010, A&A, 523, A7
Hamuy, M., Phillips, M. M., Suntzeff, N. B., et al. 1996, AJ, 112, 2438
Hicken, M., Challis, P., Jha, S., et al. 2009b, ApJ, 700, 331
Hicken, M., Challis, P., Kirshner, R. P., et al. 2012, ApJS, 200, 12
Hicken, M., Wood-Vasey, W. M., Blondin, S., et al. 2009a, ApJ, 700, 1097
Hounsell, R., Scolnic, D., Foley, R. J., et al. 2018, ApJ, 867, 23
Hsiao, E. Y., Conley, A., Howell, D. A., et al. 2007, ApJ, 663, 1187
Hsiao, E. Y., Phillips, M. M., Marion, G. H., et al. 2019, PASP, 131, 014002
Ivezic, Z., Kahn, S. M., Tyson, J. A., et al. 2019, ApJ, 873, 111
Jha, S., Kirshner, R. P., Challis, P., et al. 2006, AJ, 131, 527
Jha, S., Riess, A. G., & Kirshner, R. P. 2007, ApJ, 659, 122
Jones, D. O., Scolnic, D. M., Riess, A. G., et al. 2018, ApJ, 857, 51
Kattner, S., Leonard, D. C., Burns, C. R., et al. 2012, PASP, 124, 114
Kessler, R., Becker, A. C., Cinabro, D., et al. 2009a, ApJS, 185, 32
Kessler, R., Bernstein, J. P., Cinabro, D., et al. 2009b, PASP, 121, 1028

Kirshner, R. 2012, RAISIN: Tracers of Cosmic Expansion with SN IA in the IR, HST Proposal 13046 (Baltimore, MD: STScI)
Kirshner, R. 2014, Extracting distances from WFIRST/AFTA light curves and spectra, NASA Proposal 14-WPS14-14 (Washington, DC: NASA)
Kirshner, R. P. 2013, in IAU Symp. 281, Binary Paths to Type Ia Supernovae Explosions, ed. R. Di Stefano, M. Orio, & M. Moe (Cambridge: Cambridge Univ. Press), 1
Kirshner, R. P. & The RAISIN TEAM 2014, AAS Meeting, 223, 116.10
Komatsu, E., Smith, K. M., Dunkley, J., et al. 2011, ApJS, 192, 18
Krisciunas, K., Contreras, C., Burns, C. R., et al. 2017, AJ, 154, 211
Krisciunas, K., Garnavich, P. M., Stanishev, V., et al. 2007, AJ, 133, 58
Krisciunas, K., Hastings, N. C., Loomis, K., et al. 2000, ApJ, 539, 658
Krisciunas, K., Marion, G. H., Suntzeff, N. B., et al. 2009, AJ, 138, 1584
Krisciunas, K., Phillips, M. M., & Suntzeff, N. B. 2004a, ApJL, 602, L81
Krisciunas, K., Phillips, M. M., Suntzeff, N. B., et al. 2004b, AJ, 127, 1664
Krisciunas, K., Suntzeff, N. B., Candia, P., et al. 2003, AJ, 125, 166
Krisciunas, K., Suntzeff, N. B., Phillips, M. M., et al. 2004c, AJ, 128, 3034
Krisciunas, K., Suntzeff, N. B., Phillips, M. M., et al. 2005, AJ, 130, 350
Leloudas, G., Stritzinger, M. D., Sollerman, J., et al. 2009, A&A, 505, 265
Mandel, K. S., Foley, R. J., & Kirshner, R. P. 2014, ApJ, 797, 75
Mandel, K. S., Narayan, G., & Kirshner, R. P. 2011, ApJ, 731, 120
Mandel, K. S., Scolnic, D. M., Shariff, H., Foley, R. J., & Kirshner, R. P. 2017, ApJ, 842, 93
Mandel, K. S., Wood-Vasey, W. M., Friedman, A. S., & Kirshner, R. P. 2009, ApJ, 704, 629
Meikle, W. P. S. 2000, MNRAS, 314, 782
Mosher, J., Guy, J., Kessler, R., et al. 2014, ApJ, 793, 16
Mould, J. R., Huchra, J. P., Freedman, W. L., et al. 2000, ApJ, 529, 786
Narayan, G. S., Rest, A., & Tucker, B. E. 2013, PhD thesis, Harvard Univ.
Narayan, G., Rest, A., Tucker, B. E., et al. 2016, ApJS, 224, 3
O'Donnell, J. E. 1994, ApJ, 422, 158
Perlmutter, S., Aldering, G., Goldhaber, G., et al. 1999, ApJ, 517, 565
Perlmutter, S., Gabi, S., Goldhaber, G., et al. 1997, ApJ, 483, 565
Phillips, M. M. 1993, ApJL, 413, L105
Phillips, M. M. 2012, PASA, 29, 434
Phillips, M. M., Lira, P., Suntzeff, N. B., et al. 1999, AJ, 118, 1766
Phillips, M. M., Contreras, C., Hsiao, E. Y., et al. 2019, PASP, 131, 014001
Pierel, J. D. R., Rodney, S., Avelino, A., et al. 2018a, PASP, 130, 114504
Pierel, J. D. R., Rodney, S. A., Avelino, A., et al. 2018b, SNSEDextend: SuperNova Spectral Energy Distributions Extrapolation Toolkit, Astrophysics Source Code Library, ascl:1805.017
Pignata, G., Benetti, S., Mazzali, P. A., et al. 2008, MNRAS, 388, 971
Pimbblet, K. A., Penny, S. J., & Davies, R. L. 2014, MNRAS, 438, 3049
Planck Collaboration, Ade, P. A. R., Aghanim, N., et al. 2016a, A&A, 594, A8
Planck Collaboration, Adam, R., Ade, P. A. R., et al. 2016b, A&A, 594, A13
Planck Collaboration, Aghanim, N., Akrami, Y., et al. 2018, arXiv:1807.06209
Prieto, J. L., Rest, A., & Suntzeff, N. B. 2006, ApJ, 647, 501
Prieto, J. L., Garnavich, P. M., Phillips, M. M., et al. 2007, arXiv:0706.4088
Radburn-Smith, D. J., Lucey, J. R., & Hudson, M. J. 2004, MNRAS, 355, 1378
Rasmussen, C. E., & Williams, C. K. I. 2006, Gaussian Processes for Machine Learning (Cambridge, MA: MIT Press)
Rest, A., Scolnic, D., Foley, R. J., et al. 2014, ApJ, 795, 44
Riess, A. G., Casertano, S., Yuan, W., et al. 2018c, ApJ, 853, 126
Riess, A. G., Casertano, S., Yuan, W., et al. 2018b, ApJ, 855, 136
Riess, A. G., Filippenko, A. V., Challis, P., et al. 1998, AJ, 116, 1009
Riess, A. G., Macri, L. M., Hoffmann, S. L., et al. 2016, ApJ, 826, 56
Riess, A. G., Press, W. H., & Kirshner, R. P. 1996, ApJ, 473, 88
Riess, A. G., Rodney, S. A., Scolnic, D. M., et al. 2018a, ApJ, 861, 126
Schlafly, E. F., & Finkbeiner, D. P. 2011, ApJ, 737, 103
Schmidt, B. P., Suntzeff, N. B., Phillips, M. M., et al. 1998, ApJ, 507, 46
Schweizer, F., Burns, C. R., Madore, B. F., et al. 2008, AJ, 136, 1482
Scolnic, D., Jones, D., Rest, A. & Pan-STARRS Transients Team 2017, AAS Meeting, 229, 341.09
Scolnic, D., Casertano, S., Riess, A., et al. 2015, ApJ, 815, 117
Scolnic, D. M., Jones, D. O., Rest, A., et al. 2018, ApJ, 859, 101
Scolnic, D., Rest, A., Riess, A., et al. 2014a, ApJ, 795, 45
Scolnic, D. M., Riess, A. G., Foley, R. J., et al. 2014b, ApJ, 780, 37
Shariff, H., Dhawan, S., Jiao, X., et al. 2016, MNRAS, 463, 4311
Smith, R. M., Dekany, R. G., Bebek, C., et al. 2014, Proc. SPIE, 9147, 914779
Spergel, D., Gehrels, N., Baltay, C., et al. 2015, arXiv:1503.03757
Stanishev, V., Goobar, A., Amanullah, R., et al. 2018, A&A, 615, A45
Stanishev, V., Goobar, A., Benetti, S., et al. 2007, A&A, 469, 645
Stritzinger, M. D., Phillips, M. M., Boldt, L. N., et al. 2011, AJ, 142, 156
Stritzinger, M., Burns, C. R., Phillips, M. M., et al. 2010, AJ, 140, 2036
Taddia, F., Stritzinger, M. D., Phillips, M. M., et al. 2012, A&A, 545, L7

Takanashi, N., Doi, M., & Yasuda, N. 2008, MNRAS, 389, 1577
Tonry, J. L., Schmidt, B. P., Barris, B., et al. 2003, ApJ, 594, 1
Tripp, R. 1998, A&A, 331, 815
Tully, R. B., Courtois, H. M., Dolphin, A. E., et al. 2013, AJ, 146, 86
Tully, R. B., Courtois, H. M., & Sorce, J. G. 2016, AJ, 152, 50
Valentini, G., Di Carlo, E., Massi, F., et al. 2003, ApJ, 595, 779
Wallner, O., Ergenzinger, K., Tuttle, S., Vaillon, L., & Johann, U. 2017, Proc.
    SPIE, 10565, 105650K

Wang, L., Goldhaber, G., Aldering, G., & Perlmutter, S. 2003, ApJ, 590, 944
Wang, L., Strovink, M., Conley, A., et al. 2006, ApJ, 641, 50
Weinberg, D. H., Mortonson, M. J., Eisenstein, D. J., et al. 2013, PhR, 530, 87
Weyant, A., Wood-Vasey, W. M., Allen, L., et al. 2014, ApJ, 784, 105
Weyant, A., Wood-Vasey, W. M., Joyce, R., et al. 2018, AJ, 155, 201
Wood-Vasey, W. M., Friedman, A. S., Bloom, J. S., et al. 2008, ApJ, 689, 377
Wood-Vasey, W. M., Miknaitis, G., Stubbs, C. W., et al. 2007, ApJ, 666, 694
Zhan, H., & Tyson, J. A. 2018, RPPh, 81, 066901